Searches for continuous and transient gravitational waves from known neutron stars and their astrophysical implications

Matthew David Pitkin

Department of Physics and Astronomy
University of Glasgow

Presented as a thesis for the degree of Ph.D.
in the University of Glasgow, University Avenue,
Glasgow, G12 8QQ.

Professor Hubert Farnsworth: *It's a little experiment that might win me the Nobel Prize.*

Leela: *In which field?*

Professor Hubert Farnsworth: *I don't care - they all pay the same.*

Futurama

Acknowledgements

I was attracted to the field of gravitational wave research due to the promise that we would be entering exciting times with several large scale projects bringing in unprecedented amounts of new data. Given this the discovery of gravitational waves would be just round the corner, opening up gravitational wave astronomy for real. Little did I know that this has been exactly what's been said for around 30 years! Despite this I do actually believe that I've entered the field at a prime time and finding gravitational waves is just around, if not the first corner, then the next one. I've even got money on it! I'd therefore like to thank the people who have encouraged me into pursuing this, sometimes frustrating, but hopefully ultimately very rewarding, career path.

Three years ago I was made very welcome at the University of Glasgow after moving up from London. Much of that was down to the very friendly people in the two research groups I became a member of: the Institute for Gravitational Research (IGR) and the Astronomy & Astrophysics (A&A) group. When I started my PhD the gravitational wave data analysis group at Glasgow was rather small, with one faculty member and three students (including me) nestled in one small office. Being such a small group I can imagine it was a risk taking me on as a student, so I'm therefore very grateful to my supervisor Graham Woan and IGR leader Jim Hough for taking that risk and all their help since. I'm also indebted to my original officemates Réjean and Martin. Without Réjean's work to build on my PhD would have taken a very different path, and Martin was always helpful with Matlab and signal processing queries. I should also thank PPARC for funding me through my PhD.

Since then us data analysts have been marching forward attracting more and more

people. Although both Réjean and Martin have moved on (leaving me with the daunting task of filling their shoes and being the most *experienced* student!) the new guys to come in have been equally good. I'd therefore like to say a big thanks to John and Jen for being brilliant officemates and making ours the best office in the Kelvin building (keep up the good work with James).

With the official business done I'll put you out of your misery in finding out who else has made it into the acknowledgement section and who hasn't. Going back to when I started my PhD I was quickly drawn into the close knit group of A&A students. So thanks to: Kirsty - for many nights of vodka and diet Coke; Ross - for his moments of extreme outrage; Iain - for providing an unmitigated barrage of sarcasm and web links; Brendan - for full on gingerness; Brian, Gail, Eduard, Hugh etc - for football; Graeme and Norman - for all things computer based; and everyone else for being so nice, aaahh.

In the last year there have been many people who've taken on the task of stopping me finishing my PhD, so here I give them their dues. Bob has done a fine job deflecting anyone else's misdemeanours by providing a reputation no-one can match. Helen has valiantly dragged us to the pub at any and every sunny opportunity, with Richard and Neil only to happy to come along. A big seven out of ten goes to Rav, who by returning to Glasgow got me back in the pub watching football where I belong. Mandy also deserves thanks for providing a much needed distraction from the horrors of work.

My friends and family south of the border are also deserving a large amount of thanks. Thank you Mum and Dad, Rebecca - for giving me someone to look up to, Gemma and Andrew. Colin, Neil, Jim, Steve, Justin and all the others with whom I got through Sandringham School have been great friends over the years. James, Mike, Rich, Eve and all my other friends from UCL gave me a great time as an undergraduate and continue to be good friends. All of whom have provided great encouragement for, and more often a refuge from, my work.

Thanks should also be extended to a great many members of the LIGO Scientific Collaboration (LSC), for making collaboration meetings a sometimes enjoyable

experience, and for all the help and advice that's been extended to me.

As ever there are people who've had to be left out here, but a great big thanks to you all wherever you are.

Declaration

This thesis presents upper limit results on the strength of gravitational waves from known neutron stars using data from the LIGO and GEO 600 interferometric gravitational wave detectors as part of the LIGO Scientific Collaboration (LSC). This work was performed as part of the LSC, and as such much work has been done by a great many people in building and maintaining the detectors, obtaining and characterising the data, and developing software components that we have used. Below I provide a summary of the work performed by myself with reference to that of others.

The first chapter describes the basic theory behind gravitational radiation and summarises some of the properties of gravitational wave sources. A brief description is given of interferometric gravitational wave detectors, including their major noise sources. A summary of the previous searches performed by the LSC is given along with some of the main results.

Chapter 2 describes neutron stars and their potential as sources of continuous gravitational waves. A description of the search algorithm and Bayesian parameter estimation technique, as developed by Dupuis and Woan [1], is provided. New to this thesis are descriptions of techniques to deal with pulsar timing noise and pulsars in binary systems. These have been developed by myself and Graham Woan, with the software being validated and checked by myself. The binary software has made use of the pulsar timing software TEMPO [2]. Verification of the code has relied greatly on information provided to us by Michael Kramer of Jodrell Bank Observatory.

In Chapter 3 the results of searches for gravitational waves from 93 known pulsars using data from the LSC S3 and S4 science runs are presented. Many of the pulsar

timing parameters were supplied by Michael Kramer and Andrew Lyne of Jodrell Bank Observatory, and the Australia Telescope National Facility pulsar catalogue. I describe the selection of pulsars used in the analysis, noting errors on the pulsars parameters and for the first time discussing the possible effects of timing noise on our analysis for all pulsars. Results for 65 of these pulsars have never before been obtained. The S3 and S4 analyses have been performed by myself and include the new method of combining the two data sets for a single analysis, with all the results, in terms of upper limits on gravitational wave amplitude and pulsar ellipticity, presented here. I suggest a method of displaying some results on a moment of inertia-ellipticity plane, thus providing an exclusion region in this parameter space.

In Chapter 4 the emission of gravitational waves from quasi-normal modes ring-downs of neutron stars is discussed. Also discussed is the generation of such modes from neutron star glitches. I present a preliminary search for gravitational wave ring-down signals from the magnetar SGR 1806-20 during a giant flare on 27^{th} December 2004. For our search I describe and make use of matched filtering software developed by Jolien Creighton and others, but which had otherwise never been used for neutron star ring-down searches. I also describe a search method developed by myself and Graham Woan based on Bayesian evidence, by making use work of Bretthorst [3].

Chapter 5 describes the future of both these searches and prospects for the latest science run.

Abstract

We have used data from the third and fourth science runs of the laser interferometric gravitational wave detectors LIGO and GEO 600 to produce upper limits on the emission of gravitational waves from a selection of known neutron stars. Two different emission mechanisms are looked into; i) the emission of continuous gravitational waves from triaxial neutron stars; and ii) emission of quasi-normal mode ring-downs from glitching neutron stars.

We have produced upper limits on the gravitational wave amplitude and ellipticity for 93 known pulsars assuming continuous emission via triaxiality. This selection of pulsars includes the majority of currently known pulsars with frequencies $> 25\,\mathrm{Hz}$, with many within binary systems and globular clusters. New algorithms to take into account the motions within binary systems and possible effects of pulsar timing noise are presented. Also shown is the first analysis to combine the data sets from two distinct science runs as a method of lowering the upper limits. The results are starting to push into the range of plausible neutron star ellipticities, with the Crab pulsar closely approaching the limit that can be set through spin-down arguments. For the 32 of these pulsars in globular clusters the results provide upper limits independent of the cluster dynamics. The astrophysical significance of these results is discussed. Along with results from true pulsars we also present the extraction of simulated signals injected into the interferometers during the science runs. These provide validation checks of both the extraction software and the coherence of the detectors.

Two techniques are discussed in relation to searching for quasi-normal mode ring-down signals from excited neutron stars, for example during a glitch; one based on

matched filtering and the other based on Bayesian evidence. These are both applied to a search for such a signal from SGR 1806-20 during a GRB on 27$^{\text{th}}$ December 2004, using the LIGO H1 detector and GEO 600 data. This search provided upper limits on the energy released in gravitational waves via quasi-normal modes over the range of frequencies from 1-4 kHz. These are compared with results from a previous search using the bar detector AURIGA [4] and theoretical arguments. The limitations of the search and search techniques, and possible extensions to these, are discussed.

The future of these searches is discussed with regard to extensions to the analysis techniques and number of potential sources. Particular emphasis is placed on searches using data from the current LSC S5 science run.

Contents

List of Figures

List of Tables

Well, the thing about a black hole - its main distinguishing feature - is it's black. And the thing about space, your basic space colour is black. So how are you supposed to see them?

Holly - Red Dwarf

Chapter 1

Introduction

This chapter will provide a brief overview of the theory behind gravitational radiation. A selection of sources are discussed with emphasis on their potential to produce detectable gravitational waves. A brief overview of the detection of gravitational waves using interferometry is given. Finally, a summary of a selection of previous searches for several types of gravitational wave source is given.

1.1 The history and theory of gravitational radiation

Prior to 1915 all conventional gravitational theory was Newtonian and in the equations of this framework the force of gravity was thought of as any other force - the action of one body on another - with, for the case of gravity, that action being instantaneous. Masses attracted other masses because that was a property of mass. This theory provided no method for the production of gravitational waves which would only come about after a radical rethink of the theory of gravity[1]. With the publication of Einstein's General Theory of Relativity in 1915 [6] gravity became a property of space-

[1] although combining Newtonian gravity with special relativity, through the insertion of a delay, or retardation, between the source, $\rho(x,t)$, and its Newtonian gravitational potential field, $\phi(y, t-|x-y|/c)$, gives the basic properties from which gravitational waves can be derived, as in Schutz (1984) [5].

time itself (indeed the idea of space-time as a combined entity $\{t, x, y, z\}$ in which the frame of reference was paramount had only just been introduced), where mass/energy curved space-time and objects followed geodesics in this curved manifold. From the equations of General Relativity (GR), as the theory is universally known, the prediction of gravitational waves - ripples in space-time - was quickly derived by Einstein [7].

1.1.1 The basics of gravitational wave theory

This section will provide an overview of the derivation of gravitational waves from GR, but is not meant to be an in-depth description. A far fuller description can be found in Schutz (1985) [8], along with definitions of many of the terms and equations used herein.

GR describes the force of gravity in the new terms of geometry. This geometry is described by the geodesic equation, which is the GR equivalent of the regular equation of motion $F = ma$, and the Riemann curvature tensor (defined in [8]). The source of this curvature is the energy-momentum density and flux of space which is described by the *stress-energy* tensor $T^{\alpha\beta}$. From these an equivalent of the Newtonian gravitational potential field equation (or electromagnetic potential field), the general relativistic field equation, known as Einstein's field equation, is defined (in natural units so $G = c = 1$) as,

$$G^{\alpha\beta} \equiv R^{\alpha\beta} - \frac{1}{2} g^{\alpha\beta} R = 8\pi T^{\alpha\beta}, \tag{1.1}$$

where $R^{\alpha\beta}$ and R are the Ricci tensor and scalar describing the curvature of space (from the Riemann tensor), and $g^{\alpha\beta}$ is the space-time metric describing transformations relevant for the space-time. Deriving the formula for gravitational waves comes straight from Einstein's field equation in the weak field approximation. Under this approximation the metric $g_{\alpha\beta} = \eta_{\alpha\beta} + h_{\alpha\beta}$, where $\eta_{\alpha\beta}$ is the Minkowski metric for flat space ($\eta_{\alpha\beta\ (\alpha=\beta)} = \{-1, 1, 1, 1\}$ and $\eta_{\alpha\beta\ (\alpha\neq\beta)} = 0$) and $h_{\alpha\beta}$ is some small perturbation with $|h_{\alpha\beta}| \ll 1$. The *background Lorentz transforms*, again defined in [8], show that $h_{\alpha\beta}$ transforms as a tensor all by itself rather than just being part of $g_{\alpha\beta}$, so the under-

lying space-time is always flat with $h_{\alpha\beta}$ defined on top of it. This allows us to think of our curvature, and Riemann tensor, just in terms of $h_{\alpha\beta}$. For convenience the metric perturbation $h_{\alpha\beta}$ is redefined as the *trace reverse*

$$\bar{h}^{\alpha\beta} = h_{\alpha\beta} - \frac{1}{2}\eta^{\alpha\beta}h. \tag{1.2}$$

Under the weak field approximation equation 1.1 reduces to

$$\Box\bar{h}^{\alpha\beta} = -16\pi T^{\alpha\beta}, \tag{1.3}$$

which for the case of free space, where $T^{\alpha\beta} = 0$, becomes

$$\left(-\frac{\partial^2}{\partial t^2} + \nabla^2\right)\bar{h}^{\alpha\beta} = 0. \tag{1.4}$$

It can be seen that equation 1.4 is the three-dimensional wave equation, the solution of which for the simplest plane waves is

$$\bar{h}^{\alpha\beta} = A^{\alpha\beta}\exp\left(ik_\alpha x^\alpha\right), \tag{1.5}$$

showing that small perturbations in space-time will propagate as a wave. Through further proofs, as given in [8], it can be shown that this wave will propagate at the speed of light. Applying the *transverse-traceless* gauge conditions Schutz [8] shows that the wave will be transverse and that the tensor has the form

$$h^{\mathrm{TT}}_{\alpha\beta} = \begin{pmatrix} 0 & 0 & 0 & 0 \\ 0 & \bar{h}_{xx} & \bar{h}_{xy} & 0 \\ 0 & \bar{h}_{xy} & -\bar{h}_{xx} & 0 \\ 0 & 0 & 0 & 0 \end{pmatrix}, \tag{1.6}$$

i.e. if the wave is travelling in the z direction it will only have amplitude components in the x and y directions, and with only two independent amplitude values A^{TT}_{xx} and A^{TT}_{xy}. The fact that the tensor must be traceless, $A^{\alpha}{}_{\alpha} = 0$, implies that $\bar{h}^{\mathrm{TT}}_{\alpha\beta} = h^{\mathrm{TT}}_{\alpha\beta}$.

In a coordinate dependent system the effect of a gravitational wave will not be seen. However, we can see how these waves (metric perturbations) affect particles by looking at their effect on the proper distance $d\ell$ between two such particles. Applying the equation of geodesic deviation it can be shown, again in Schutz (1985) [8], that for two particles separated in the x-direction, with 4-velocity $\vec{U} = (1, 0, 0, 0)$ and separation vector $\vec{\xi} = (0, \epsilon, 0, 0)$, that

$$\frac{\partial^2}{\partial t^2}\xi^x = \frac{1}{2}\epsilon\frac{\partial^2}{\partial t^2}h_{xx}^{\mathrm{TT}}, \text{ and } \frac{\partial^2}{\partial t^2}\xi^y = \frac{1}{2}\epsilon\frac{\partial^2}{\partial t^2}h_{xy}^{\mathrm{TT}}. \tag{1.7}$$

Considering two particles initially having a separation vector $\vec{\xi} = (0, \epsilon\cos\theta, \epsilon\sin\theta, 0)$, we get acceleration in ξ of

$$\frac{\partial^2}{\partial t^2}\xi^x = \frac{1}{2}\epsilon\cos\theta\frac{\partial^2}{\partial t^2}h_{xx}^{\mathrm{TT}} + \frac{1}{2}\epsilon\sin\theta\frac{\partial^2}{\partial t^2}h_{xy}^{\mathrm{TT}}, \tag{1.8}$$

and

$$\frac{\partial^2}{\partial t^2}\xi^y = \frac{1}{2}\epsilon\cos\theta\frac{\partial^2}{\partial t^2}h_{xy}^{\mathrm{TT}} - \frac{1}{2}\epsilon\sin\theta\frac{\partial^2}{\partial t^2}h_{xx}^{\mathrm{TT}}. \tag{1.9}$$

Using the real part of the plane wave solution to the wave equation (with us stationary at $z = 0$), so $h_{\alpha\beta}^{\mathrm{TT}} = A_{\alpha\beta}\cos(\omega t)$, as shown by Hendry [9], gives solutions to equations 1.8 and 1.9 in x and y of

$$\xi^x = \epsilon\cos\theta + \frac{1}{2}\epsilon\cos\theta A_{xx}^{\mathrm{TT}}\cos\omega t + \frac{1}{2}\epsilon\sin\theta A_{xy}^{\mathrm{TT}}\cos\omega t, \tag{1.10}$$

and

$$\xi^y = \epsilon\cos\theta + \frac{1}{2}\epsilon\cos\theta A_{xy}^{\mathrm{TT}}\cos\omega t - \frac{1}{2}\epsilon\sin\theta A_{xx}^{\mathrm{TT}}\cos\omega t. \tag{1.11}$$

If we have a ring of particles at various angles between 0 and 2π radians these equations show how the passing of a plane gravitational wave effects them in terms of the proper distance between them and the centre of the ring (see fig 1.1). These equations show that because of the independence of h_{xx}^{TT} and h_{xy}^{TT} we have two distinct linear polarisations of the wave, one when $h_{xx}^{\mathrm{TT}} \neq 0$ and $h_{xy}^{\mathrm{TT}} = 0$ and the other when $h_{xx}^{\mathrm{TT}} = 0$

and $h_{xy}^{\mathrm{TT}} \neq 0$. These two states, called 'plus' (+) and 'cross' (×) are seen in figure 1.1 to be rotated by 45° to each other, as opposed to electromagnetic wave polarisation states with a rotation of 90°.

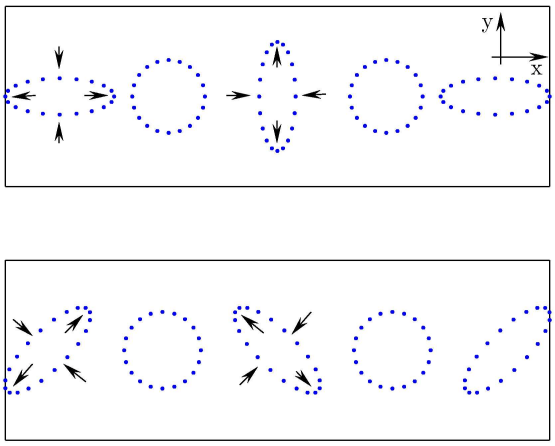

Figure 1.1: The effect of a plane gravitational wave on a ring of particles over one wavelength for the + polarisation (top) and the × polarisation (bottom).

1.1.2 Generation of gravitational waves

The equations above described how a gravitational wave propagates through space, but says nothing about their generation as the *stress-energy* tensor is set to zero. To study the generation of gravitational waves we will have return to equation 1.3 and follow the methodology shown in Schutz (1985) [8]. The solutions of this are simplified through two assumptions: i) the time dependent part of $T_{\alpha\beta}$ is sinusoidal with angular frequency Ω; and ii) the source is small compared to the wavelength of radiation emitted, $\epsilon \ll 2\pi/\Omega$. Under these assumptions the solution for $\bar{h}_{\alpha\beta}$, to lowest order, has the form

$$\bar{h}_{\alpha\beta} = 4J_{\alpha\beta}e^{i\Omega(r-t)}/r, \tag{1.12}$$

where r is the distance from the source. The $J_{\alpha\beta}$ term can be written in the form of the quadrupole moment of the mass distribution

$$I^{lm} \equiv \int T^{00} x^l x^m \mathrm{d}^3x \approx \int \rho x^l x^m \mathrm{d}^3x, \tag{1.13}$$

where $T_{00} \approx \rho$ is the mass density (under the assumption that the source motion is slow i.e. $v \ll c$), so

$$J_{\alpha\beta} e^{-i\Omega t} = \frac{1}{2} \frac{\mathrm{d}^2}{\mathrm{d}t^2} I_{\alpha\beta}. \tag{1.14}$$

From this we can write our solution as

$$\bar{h}_{jk} = -2\ddot{I}_{jk}/r = -2\Omega^2 I_{jk} e^{i\Omega r}/r. \tag{1.15}$$

It can be shown, as in Flanagan and Hughes (2005) [10], that the lower order moments of the mass distribution (zeroth and dipole) are ruled out as contributing to the gravitational wave emission through the conservation of mass/energy and angular momentum respectively. A simple approximation of the quadrupole moment for a source with total mass M and size R, shows that I_{jk} is of order MR^2. Equation 1.15 can be used to get a simple estimate of the gravitational wave amplitude (as shown in Schutz, 1999 [11]) by noting that for non-spherical motions the components of $\ddot{I}_{jk}$ will have magnitudes or order Mv^2, where v is the non-spherical component of the velocity inside the source. Given this an approximate amplitude will be

$$h \sim 2Mv^2/r \tag{1.16}$$

(or $h \sim 2GMv^2/c^4r$ converting back to SI units). It should be stated that spherically symmetric motions will not radiate.

Again we can make a gauge restriction and find a *transverse-traceless* gauge which gives the simplest form of the wave. In such a gauge the quadrupole moment becomes

the reduced quadrupole moment tensor,

$$I_{jk} \to I_{jk} - \frac{1}{3}\delta_{jk} I^{l}{}_{l}. \tag{1.17}$$

With axis aligned so that the wave is travelling in the z-direction we get components of our perturbation given by

$$\bar{h}^{\mathrm{TT}}_{zi} = 0, \tag{1.18}$$

$$\bar{h}^{\mathrm{TT}}_{xx} = -\bar{h}^{\mathrm{TT}}_{yy} = -\Omega^2 (I_{xx} - I_{yy}) e^{i\Omega r}/r, \tag{1.19}$$

$$\bar{h}^{\mathrm{TT}}_{xy} = -2\Omega^2 I_{xy} e^{i\Omega r}/r. \tag{1.20}$$

These show that the reduced quadrupole moment provides the main factor in the gravitational wave amplitude. This method is not the exact solution but is in general a good approximation for simple sources and for providing estimates of source strength.

We will consider the example of two stars in a binary system separated by R and of equal mass m (as shown in [10]). If we chose these to be lying in the $x-y$ plane, then in our coordinates $x = x_1 = R\cos\Omega t$, $y = x_2 = R\sin\Omega t$ and $z = x_3 = 0$. The reduced quadrupole moment for this system is

$$I_{jk} = \mu\left(x_j x_k - \frac{1}{3}\delta_{jk} r^2\right) \tag{1.21}$$

$$= \mu R^2 \begin{pmatrix} \cos^2\Omega t - \frac{1}{3} & \cos\Omega t \sin\Omega t & 0 \\ \cos\Omega t \sin\Omega t & \cos^2\Omega t - \frac{1}{3} & 0 \\ 0 & 0 & -\frac{1}{3} \end{pmatrix} \tag{1.22}$$

where $\mu = m_1 m_2/(m_1+m_2) = m/2$ is the reduced mass of the system, giving coefficients of the time varying parts of the second derivative, $\ddot{I}_{jk}$, as $-2\Omega^2\mu R^2$. This gives a typical magnitude for h of

$$h \approx \frac{4\mu\Omega^2 R^2}{r}. \tag{1.23}$$

In this example we can use Kepler's third law ($R^3\Omega^2 = GM$, where $M = 2m$ is the

total mass) to give (in SI units)

$$h = \frac{(GM)^{5/3}\Omega^{2/3}}{c^4 r}. \tag{1.24}$$

Values will be placed on this for realistic examples in §1.2. For two unequal masses $M(= m_1 + m_2)$ will be replaced by the *chirp mass* $\mathcal{M} = \mu^{3/5}M^{2/5}$. These gravitational waves will be have a completely circular polarisation perpendicular to the plane and completely linear polarisation along the plane.

The frequency of gravitational waves can often, as with the above example, be related to motions of the source, but in many cases it is also related to the natural frequency of a self-gravitating body

$$f = \sqrt{G\bar{\rho}/4\pi} \approx (1/2\pi)\sqrt{GM/R^3}, \tag{1.25}$$

where $\bar{\rho}$ is the mean mass-energy density [11]. Some examples of this will be given in §1.2.

The energy carried away by gravitational waves (the source's luminosity) is given by

$$\frac{\mathrm{d}E}{\mathrm{d}t} = L = -\frac{G}{5c^5}\langle \dddot{I}_{jk}\dddot{I}^{jk}\rangle. \tag{1.26}$$

This can be useful for estimating the timescale over which objects will emit gravitational waves.

1.2 Sources of gravitational waves

The above equations can be used to derive the approximate strength of gravitational waves for simplified sources. From these we can estimate what kind of systems will yield detectable levels of radiation. Some sources and their classification are discussed below, with more thorough reviews to be found in Thorne (1987) [12] and Schutz (1999) [11].

1.2.1 Man-made sources

We could consider the possibility making some sort of gravitational wave generator on human scales and then estimating the level of radiation. Following the example in [11] we will construct something analogous to the binary star system described above, consisting of two 10^3 kg masses held 10 m apart by a light rigid beam rotating about its centre at a frequency of 10 Hz. As all the motion is non-spherical we will approximate h using equation 1.16, with velocity $v \sim 300\,\mathrm{ms}^{-1}$. The distance to the source r must be at least one wavelength away in order to detect the gravitational waves rather than the nearby Newtonian field. For our generator the emission will be at twice the rotation frequency $f = 20$ Hz as the mass distribution is symmetric about the rotation axis, and the corresponding wavelength will be $\lambda = 1.5{\times}10^7$ m. So given these values we get an estimate of the gravitational wave amplitude $h \sim 1{\times}10^{-43}$, which is ~ 20 orders of magnitude below the level we can expect to be able to detect. This shows that human scale objects are not good sources, so we need to look elsewhere for possible sources. In the universe, however, there are many environments with extreme energetics where the mass-energy densities are at levels which begin to look more plausible as detectable gravitational wave generators. These will now be discussed.

1.2.2 Continuous wave sources

A continuous (or periodic) wave source is one that emits a quasi-sinusoidal signal over a long period. This feature will allow any detection strategy to build up signal-to-noise over a long period of observation. The fact that the signal is persistent means that the source must not be strongly damped (via gravitational wave or electromagnetic emission, particle acceleration or other mechanisms), or must have some source of power. The most obvious choice of sources with these properties are those with intrinsic frequencies due to their own orbital or rotational motion.

Neutron stars

Neutron stars are discussed in more detail in Chapter 2, but here we will described the basics of their continuous wave emission mechanism. Neutron stars (seen as pulsars or inferred in High and Low Mass X-ray Binaries - LMXBs) are known to spin with precise frequencies and small spin-down rates, i.e. they are damped slowly, therefore fulfilling both the criteria above for a continuous wave source. Due to their extremely high gravitational field neutron stars are thought to be close to spherical, but to generate gravitational waves there must be some form of asymmetry about the rotational axis. The two main forms of rotational asymmetry will be if the star is triaxial (oblate or prolate) or precessing (rotation of the spin axis). If we consider the case of a triaxial star with a bump or mountain (of mass m) giving our non-sphericity, then we can estimate the gravitational wave amplitude via equation 1.16 as in [11]. Given a radius R and rotational frequency ν (emission will be at 2ν as rotation is about the centre of mass) we get $h \sim 16\pi^2 GmR^2\nu^2/c^4 r$. It can be seen that for this case the quadrupole moment is $mR^2 = \varepsilon I_{zz}$, where $\varepsilon = (I_{xx} - I_{yy})/I_{zz}$ is the star's equatorial ellipticity, and I_{zz} is the principal moment of inertia about the rotation axis. We can write this using some canonical neutron star values giving

$$h \approx 4.2\times10^{-26}\left(\frac{I_{zz}}{10^{38}\mathrm{kg\,m^2}}\right)\left(\frac{\varepsilon}{10^{-6}}\right)\left(\frac{\nu}{100\,\mathrm{Hz}}\right)^2\left(\frac{1\,\mathrm{kpc}}{r}\right), \tag{1.27}$$

where the value of ε is on the upper end of plausible values for conventional neutron star equations of state. This shows that in general this mechanism produces quite weak gravitational waves, although the abundance of neutron stars and the fact that signal-to-noise can be built up over time means they are a good potential source within our galaxy. It can be seen in figure 1.2 that for one year of observations with the LIGO detectors at design sensitivity we are reaching into this range, and for Advanced LIGO (AdvLIGO) we should be in a range with many potential sources.

Free precession of a neutron star requires some mechanism to sustain it and is generally strongly damped. With only one pulsar (PSR B1828-11) known to exhibit

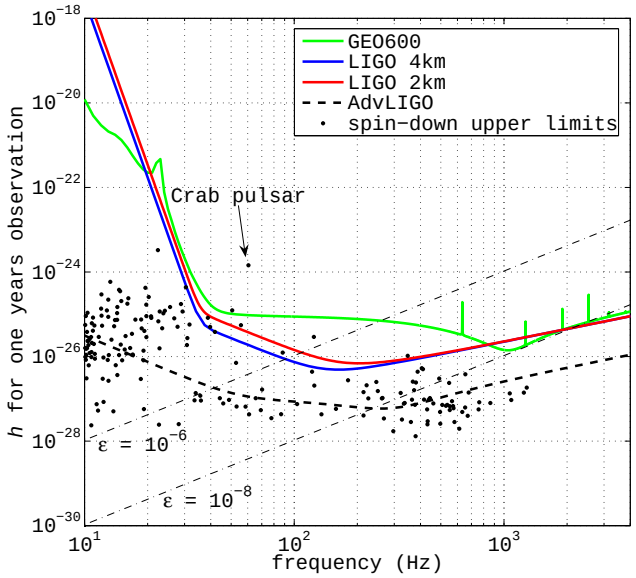

Figure 1.2: The sensitivity of the GEO 600 (tuned to 1000 Hz), LIGO and Advanced LIGO detectors for one year of observations. The Advanced LIGO design sensitivity is the current best estimate and subject to small changes. Included are lines representing the expected gravitational wave amplitude from a pulsar with an equatorial ellipticity ε of 10^{-6} and 10^{-8} at a distance of 1 kpc, with $I_{zz} = 10^{38}\,\mathrm{kg\,m^2}$. The spin-down upper limits (equation 2.3) for all known pulsars with $\nu > 5\,\mathrm{Hz}$ are also plotted.

free precession, and a few more decreasingly likely candidates [13], the population of sources is also likely to be small. It therefore provides a far less likely source of gravitational waves, with the calculations of Jones and Andersson (2002) [14] giving amplitudes of

$$h_0 \sim 10^{-27} \left(\frac{\Omega_w}{0.1}\right) \left(\frac{1\,\mathrm{kpc}}{r}\right) \left(\frac{f_s}{500\,\mathrm{Hz}}\right)^2, \tag{1.28}$$

where Ω_w is the wobble angle, and f_s is the signal frequency, which is well below the level of sensitivity of LIGO, but may be a source for AdvLIGO.

Hot, newly formed neutron stars, or stars heated up during accretion from a companion, could provide continuous gravitational waves due to emission from hydrodynamic waves on the surface or within the star. Such a type of wave is the r-mode [15], which is driven by the rotation of the star and is analogous to Rossby (or planetary) waves on the Earth driven by the Coriolis force. For newly formed stars this could provide continuous wave emission for maybe up to a year after formation, until the star has cooled and spun-down sufficiently [11]. For accreting stars, i.e. in LMXBs, the

accretion can spin-up the star's rotation such that gravitational wave emission could provide a natural frequency limit at which gravitational wave energy loss balances that spinning-up the star. As such the gravitational wave emission would be directly related to the systems X-ray luminosity.

Binary systems

The other main source of continuous waves will be binary or multiple systems. All orbiting systems will emit gravitational waves to some extent (as in our man-made generator example), but the scale of the system will be important in whether the waves are detectable. Evidence for the existence of gravitational waves was in fact inferred by the study of a neutron star binary system discovered by Hulse and Talyor (1975) [16, 17] in which the orbit was losing energy exactly as expected if carried away by gravitational radiation. As seen above gravitational waves will be emitted at twice the frequency of the orbital motion, with the amplitude proportional to the frequency squared and the masses involved. Through the emission of gravitational radiation binaries will eventually inspiral, increasing in frequency and therefore amplitude until coalescence. As an example of this we can find the gravitational wave amplitudes and coalescence times for a variety of systems. We will start with the nearest stellar system to our own, the α and β-Centauri system. This system lies at a distance of 4.35 ly with two stars of roughly $1\,\mathrm{M}_\odot$ having an orbital period of 80 years ($f = 4{\times}10^{-10}\,\mathrm{Hz}$) and a separation of 23 AU. Using equation 1.24 we can calculate the amplitude of gravitational waves seen at Earth as $h \sim 6{\times}10^{-23}$, which would be large enough for detection were it at much higher frequencies, but is well out of the frequency range of any planned detector (see figure 1.3). The *chirp time* (or time to coalescence) of the binary can also be estimated by making use of its luminosity and current kinetic energy ($= -1/2$ potential energy $= Gm_1m_2/2R = G\mu M/2R$) via $t_{\mathrm{chirp}} = 1/4(E_{\mathrm{binary}}/L_{\mathrm{binary}}) \sim 10^{23}$ years (from a luminosity of $L_{\mathrm{binary}} \sim 10^6\,\mathrm{W}$). This shows that for main sequence binary systems the gravitational wave emission will take many orders of magnitude longer than the Hubble time to cause noticeable orbital decay.

To get to amplitude levels and frequencies necessary for observations the binary systems must be much more compact, therefore with much faster periods, and/or have much more massive components, like supermassive black holes. For many systems made up of stellar remnants i.e. white-dwarfs, neutron stars or stellar mass black holes, orbital periods on the order of hours are seen. Such systems will also have chirp times within the age of the universe, leading to the possibility of observing the final inspiral (discussed below). There are predicted to be many galactic double white-dwarf binary systems $\sim 10^8$ (see Nelemans *et al.*, 2001 [18]), a proportion of which with orbital periods of a few hours (some of which have been observed, Saffer *et al.*, 1998 [19]). These provide a large population of sources around $f \sim 10^{-4}\,\mathrm{Hz}$, with gravitational wave amplitudes (assuming two $0.5\,\mathrm{M}_\odot$ white-dwarfs and a distance of 100 light years) of $h \sim 10^{-21}$. Again as these are continuous sources, the signal-to-noise can be built up over time. Due to the large amount of sources there could be much source confusion with a noise floor made up of overlapping binary systems (see figure 1.3). This presents a potential challenge for LISA[2] data analysis in this frequency range.

As well as double white-dwarf systems, there are currently five *known* galactic double neutron star systems (see Burgay *et al.*, 2003 [20]), although the total population of these will be far smaller than for white-dwarfs. These all have period of a few hours leading to an estimate for the amplitude at a similar level to that for the white dwarfs. The population of galactic black hole binaries will also be quite small and again produce gravitational waves of a similar order of magnitude.

Black hole binaries consisting of supermassive black holes, for example those found at the centre of most galaxies, start to become of interest on cosmological distance scales. Such systems of black holes with $M \gtrsim 10^6\,\mathrm{M}_\odot$ are likely to be visible to LISA throughout the entire universe with amplitudes as shown in figure 1.3.

[2]LISA is a future spaced-based interferometric gravitational wave detector designed to view the low frequency band from $\sim 10^{-4} - 10^{-1}\,\mathrm{Hz}$, and will be discussed briefly later.

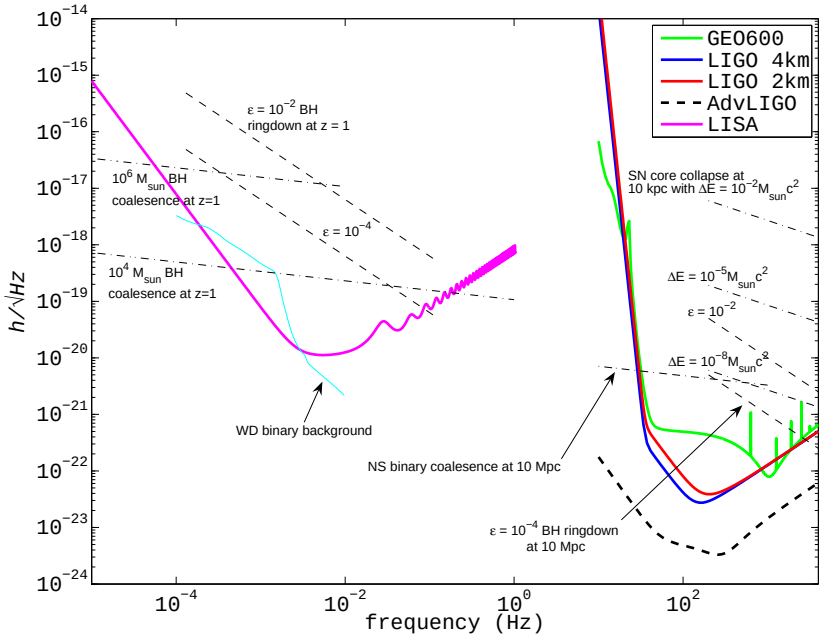

Figure 1.3: The noise spectrum of the current ground based interferometers (GEO 600 and the LIGO detectors), the proposed Advanced LIGO upgrade and the planned space-based detector LISA. Also shown are curves representing approximate theoretical predictions of source amplitudes for a variety of transient and continuous sources.

1.2.3 Burst sources

These sources will be those that emit a short duration transient burst of gravitational radiation. The transient nature of the source means that signal-to-noise cannot be built up over time and the event cannot be re-observed, so the event must be very strong to have confidence in a detection and gain useful source information. Possible mechanisms to produce such bursts are thought to occur in core-collapse supernova, the final inspiral and coalescence of compact binaries, ringing of black holes/neutron stars and cosmic string cusps. There may be other unknown burst sources, but we shall briefly discuss only the conventional ones.

Binary inspirals

As we have just discussed binary systems it seems natural to extend that to the point at which the binary system has lost so much energy through gravitational wave emission that it is close to coalescence. During this stage the gravitational wave amplitude will

be large and, for binaries consisting of neutron star and stellar mass black holes, the frequency of the signal will sweep across the range of current ground based detectors; up to $f_{\max} \approx 1\,\mathrm{kHz}$ for neutron stars and $f_{\max} \approx 10/(M_1/M_\odot)\,\mathrm{kHz}$ for black holes with the larger mass M_1 [12]. This means that for stellar mass black holes $f_{\max}$ will be at high frequencies and for supermassive black holes $f_{\max}$ will be at low frequencies. Two neutron stars with a period of one second will be approximately one month from merging, with (at a distance of 10 Mpc) the gravitational wave amplitude being $\sim$ a few $\times 10^{-24}$. By the time such a system gets to 100 Hz it will be only a few seconds from coalescence with amplitudes of $\sim 10^{-22}$, which is within the detectable range of current instruments. These events can be well modelled using the quadrupole approximation for the majority of the inspiral, but the final coalescence is far less well understood. The rate of double neutron star binary systems about to coalesce within the effective seeing distance of the LIGO interferometers ($\sim$ 20 Mpc) and AdvLIGO ($\sim$ 350 Mpc) has been estimated from the galactic population by Kalogera *et al.* (2005a and 2005b) [21, 22] to be $R_{\mathrm{LIGO}} \sim 0.35\,\mathrm{yr}^{-1}$ and $R_{\mathrm{AdvLIGO}} \sim 190\,\mathrm{yr}^{-1}$ respectively. Recently it has been suggested by Lee and Brown (2005) [23] that neutron star-black hole binaries could provide an even more promising source for LIGO with an detection rate increased by a factor of ~ 20 over double neutron star mergers. From Fox *et al.* (2005) [24] there now appears to be strong observational evidence that such mergers occur, with recent observations of the X-ray afterglow of short γ-ray bursts (GRBs) indicating mergers to be the source.

The inspiral will leave a remnant, most likely a black hole, which will be vibrating with a characteristic frequency $f_c \approx 1.3{\times}10^4(\mathrm{M}_\odot/M)\,\mathrm{Hz}$ (from equation 1.25 using the Schwarzschild radius $r_s = 2GM/c^2$). These vibrations will ring-down with a quality factor $Q = 2(1-\hat{a})^{(-9/20)}$, where $\hat{a}$ is related to the spin and must be greater than unity meaning $Q > 2$ (see Creighton, 1999 [25]). For a black hole formed from two $1.4\,\mathrm{M}_\odot$ neutron stars (assuming the majority of the mass is not lost) $f_c \approx 5.5\,\mathrm{kHz}$ with

a decay time $\tau \gtrsim 10\,\mathrm{hrs}$. The gravitational wave amplitude (taken from [12]) will be

$$h \approx 1.0\times10^{-20}\left(\frac{\epsilon}{0.01}\right)^{\frac{1}{2}}\left(\frac{10^3\,\mathrm{Hz}}{f_c}\right)\left(\frac{10\,\mathrm{Mpc}}{r}\right), \tag{1.29}$$

where $\epsilon = \Delta E/Mc^2$, is the efficiency of conversion of energy. For our example assuming an efficiency of $\epsilon = 0.01$ and a distance of 10 Mpc this gives $h \approx 2\times10^{-21}$, which should be detectable with current detectors. For larger (but still stellar range) mass mergers the frequencies should be well into the current detector range with high signal-to-noise, and as the waveform is very well defined should make a good target for detection. For the supermassive black hole mergers the frequencies will be in the milliHertz range, covered by future space based detectors e.g LISA, with gravitational wave amplitudes so large that they will be observable throughout the universe.

The central supermassive black holes in galaxies will occasionally scatter or 'eat' a normal stellar mass object. These extreme mass ratio inspirals (EMRIs) could be an interesting low frequency gravitational wave source with the waveform providing a precise map of the space-time around the black hole. For a single black hole the rate would typically be far less than one per year, but with approximately 100 large galaxies within 10 Mpc the event rate for these could be reasonable.

Supernova core-collapse

The formation of neutron stars and stellar mass black holes is through the core-collapse of massive stars in Type II supernovae. The strength and frequency of any gravitational wave emission from such events is dependent on the degree of non-sphericity and speed of collapse. The modelling of such collapses to a neutron star is very difficult and therefore the gravitational wave amplitude and waveform is very uncertain. If the collapse remains axisymmetric then it could include bounces of the core and then damped pulsations of the proto-neutron star with characteristic frequencies of $\approx 2\,\mathrm{kHz}$. Other possibilities are that collapse could lead to a bar-mode deformation of the neutron star, leading to it rotating end-over-end, or the deformation could be so unstable as to break up the newly formed star. The large uncertainties in the various models lead

to the possibility of gravitational waves carrying away energies over a large range from $\Delta E_{\rm gw} \lesssim 10^{-10} - 10^{-2}\,{\rm M}_\odot c^2$ with frequencies from $f_c \sim 200 - 10\,000\,{\rm Hz}$ [12]. Using these ranges, and adopting equation (37) of Thorne (1987) [12] the various amplitudes of gravitational wave from core-collapse are shown in figure 1.3. Rates of Type II supernovae in our galaxy are around 1-3 per century, which extrapolating out the range of the large Virgo cluster of galaxies ($\sim 10\,{\rm Mpc}$) gives a rate of a few per year. Beyond this the rate increases roughly as the distance cubed assuming an isotropic distribution of galaxies.

Due to the simplicity of a black hole compared to a neutron star their collapse is better understood. The collapse will lead to damped vibrations of the newly formed black hole in the same way as for the mergers discussed above. For the creation of a $10\,{\rm M}_\odot$ black hole we get a characteristic frequency $f_c \approx 1\,{\rm kHz}$, which for efficiencies of $\epsilon \sim 0.01$ should give detectable gravitational waves out to around 10 Mpc (see figure 1.3). Black holes formation rates rates are thought to be at about a third of that for neutron stars, giving about one event per year to 10 Mpc. The formation of black holes in supernovae is thought to be the source of long duration GRBs under the so-called *collapsar* model (MacFadyen and Woosley, 1999 [26]).

Neutron star ring-downs

It has been discussed already that newly formed black holes and neutron stars could ring-down, but what of older neutron stars? Neutron stars are seen to glitch (discussed in more detail in Chapter 4) which it has been suggested (for example by Andersson and Kokkotas, 1998 [27]) could provide a mechanism to excite vibrational modes of the star. The main modes will be the fundamental fluid f-mode, the first pressure p-mode and the first gravitational wave w-mode. The f-modes will have frequencies of around 2 kHz, the natural frequency of a neutron star, with the other modes being at frequencies $\gtrsim 10\,{\rm kHz}$. These modes will ring down much quicker than black holes, with decay times of around 50-100 milliseconds. The gravitational wave emission from such modes depends on the amount of energy deposited in them during the glitch (or

supernova). For neutron star glitches, the amount of energy available is fairly small $\lesssim 10^{-10}\,\mathrm{M}_\odot c^2$, so these modes could only conceivably be observed within our galaxy (see equation 4.4). In supernovae the amount of energy deposited could be much higher $\lesssim 10^{-4}\,\mathrm{M}_\odot c^2$ and therefore provide a source into the Mpc range.

1.2.4 Stochastic sources

Stochastic sources are those that contribute to the general underlying background of gravitational waves. This could be due to the superposition of waves from all the types of sources discussed above, or could be primordial in nature. One of the most prominent sources at low frequency will be the large number of local binary stars. It can be seen in figure 1.3 how the galactic population of binary white dwarf systems dominates the noise floor for LISA over a certain frequency range.

One of the most exciting prospects of gravitational wave detection is the possibility of seeing gravitational waves from a tiny fraction of a second after the big bang. Whereas the photons forming the cosmic microwave background (CMB) only let us see back to their last scattering at about 300 000 years after the big bang, gravitational waves would have last scattered less than 10^{-24} seconds after the big bang [11]. Scenarios such as inflation would have lead to the amplification of initial perturbations in the gravitational field, leaving a random background of gravitational radiation today. Other alternatives to inflation would also leave their own gravitational wave signatures.

The stochastic background is generally characterised by its energy density rather than the gravitational wave amplitude. In this way we can set a limit on the energy density of the gravitational wave field in units of the critical energy density required to close the universe, ρ_{crit}, as

$$\Omega_{\mathrm{gw}}(f) = \frac{\mathrm{d}\rho_{\mathrm{gw}}/\rho_{\mathrm{crit}}}{\mathrm{d}\ln f}. \tag{1.30}$$

For inflationary scenarios this should be flat across the frequency spectrum [11], whereas other models can give altogether different spectra. The current best cosmological model

for the universe (the dark energy and cold dark matter or ΛCDM model), from a combination of CMB, Type Ia supernova, galaxy distribution and big-bang nucleosynthesis results, gives a value of the overall energy density of the universe to be $\Omega = 1$, with $\Omega_{\rm matter} \approx 0.3$ and $\Omega_\Lambda \approx 0.7$, meaning that $\Omega_{\rm gw} \ll 1$. Nucleosynthesis models place conservative bounds on the total energy density in gravitational waves integrated over frequency of $\int {\rm d}\ln f \Omega_{\rm gw}(f) < 1.1 \times 10^{-5}$ (see Abbott *et al.*, 2005b [28]). Current ground-based detectors should soon be able to start pushing the nucleosynthesis limits of $\sim 10^{-5}$ around the 100 Hz range, with AdvLIGO able to reach well below this to levels around $\sim 10^{-9}$ [11]. The space-based detector LISA could reach levels of $\Omega_{\rm gw} \sim 10^{-8}$ in the milliHertz range, but as stated its sensitivity might be limited by the binary background.

The stochastic background would be seen as a random noise in the detectors competing with their own instrumental noise. If the gravitational wave background is greater than the instrumental noise, or the instrumental noise level is known independently, then it could be detected using a single detector, but otherwise requires the cross-correlation of the output of two or more close by detectors. Detectors will only have a limited frequency over which they can constrain a gravitational wave background level, so will not be able to give definitive results without more broadband studies using different types of detectors.

Other more speculative sources of a stochastic background could be cosmic strings, phase transitions during the big bang and the death of Population III stars.

1.3 Gravitational wave detection

It was not until the 1960s that people seriously started to consider the detection of gravitational waves as plausible, and if not for the pioneering work of Joseph Weber [29] the field may have never got off the ground. The original detectors of Weber were large cylinders of aluminium called bar, or resonant mass, detectors. Here we will discuss interferometric detectors, which work based on the principle of how gravitational waves interact with free masses.

1.3.1 Interferometric detectors

The use of interferometers as gravitational wave detectors started in earnest in the 1970s with several groups turning away from the bar design. These interferometers were either a basic Michelson design (see figure 1.4) or containing Fabry-Perot cavities. The main advantage of the interferometers was their far wider bandwidth compared with a bar, which has a narrow bandwidth about its resonant frequency.

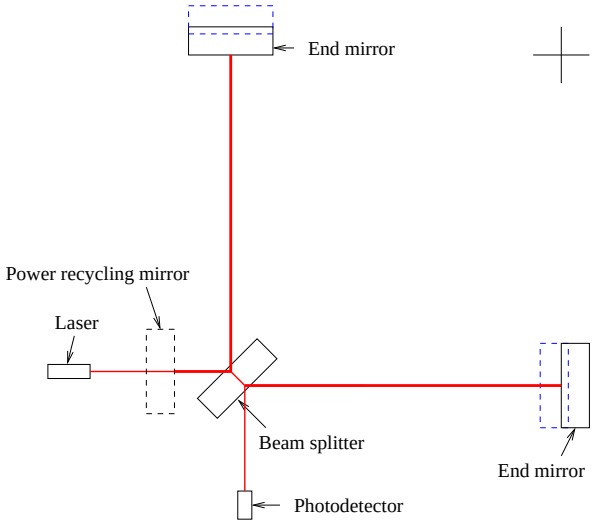

Figure 1.4: A schematic of a simple Michelson interferometer with power recycling.

Interaction of gravitational waves with detectors

The principle of detecting gravitational waves is based on how they interact with freely falling objects. It was shown in equations 1.10 and 1.11 and figure 1.1 how particles will react to a passing wave, so we will consider two free masses (our interferometer's mirrors) placed perpendicular to the direction of propagation of the wave aligned in its $x-y$ plane. If the interferometer beam splitter is placed at a distance L_0 from each mirror, then from equations 1.10 and 1.11 a gravitational wave will produce a time varying displacement δL of the mirrors, for each polarisation, of

$$\frac{\delta L^x(t)}{L_0} = \frac{1}{2}(h_+ + h_\times), \tag{1.31}$$

and

$$\frac{\delta L^y(t)}{L_0} = \frac{1}{2}(h_\times - h_+). \tag{1.32}$$

It is the ability of an interferometer to measure such changes in its arm length via the interference pattern produced that makes them useful for measuring gravitational waves. The amplitudes given above are for an optimally oriented detector, and if the plane is not perpendicular to that of the wave then the amplitude will be reduced by a certain factor (called the beam or antenna pattern). It can be seen that for longer arm lengths a smaller gravitational wave strain will be measurable for the same displacement, this means that to detect the sort of source strains discussed above interferometric gravitational wave detectors will need be large (on the km scale). Even so they will be having to sense displacements of order 10^{-18} m, roughly equivalent to sensing a displacement of order the diameter of a Gold atom between the Earth and the moon.

Kilometre scale detectors are still much smaller than the wavelength of the gravitational wave frequencies they are sensitive to $L_0 \ll \lambda \sim 10^3$ km for $f \sim 100$ Hz. This means that in the time that it takes light to travel down the arms of the interferometer only a small fraction of the displacement will have taken place. To get round this the light needs to be kept in the arms for about the half period of the wave. This can be achieved by use of a Fabry-Perot cavity or signal recycling mirror, which can increase the effective path length of the light by ~ 100 [11].

Sources of noise

The displacements to be measured are small, so there will be many sources of noise that threaten to dominate any gravitational wave signal. The dominant source of noise for an interferometer changes with frequency, and each will be briefly discussed here (see figure 1.5 for the noise sources in GEO 600).

At low frequencies (< few Hz) the underlying noise limit for any ground-based detector will be gravity gradient noise. This will come from changes in the local gravitational field, from environmental and possibly man-made sources. The spectrum

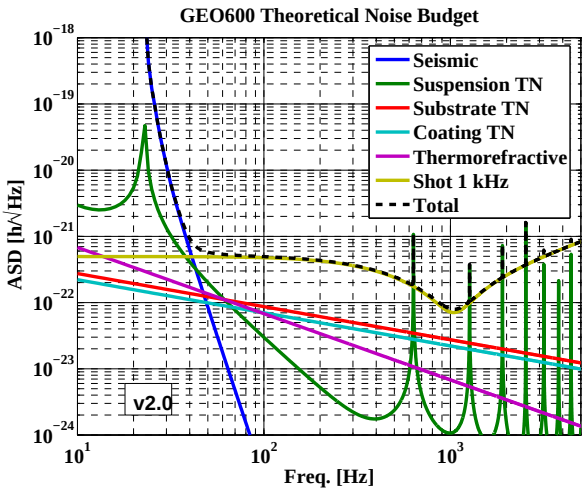

Figure 1.5: The theoretical models of the noise sources for GEO 600 across the sensitive band of the interferometer (taken from `http://www.aei.mpg.de/~jrsmith/geocurves.html`).

for this source of noise is inversely proportional to frequency to a high power and is well below other sources of noise for current detectors [11]. It could however form a noise wall at low frequencies for future ground-based detectors. For these low frequencies the only way to get around gravity gradient noise is to go into space (e.g. LISA `http://lisa.jpl.nasa.gov`).

The main low frequency ($\lesssim$ 30 Hz) noise source above gravity gradient noise is seismic noise. To isolate the mirrors from vibrations they are suspended as pendulums. This provides good isolation for frequencies above the resonant frequency of the pendulum. Even more effective isolation can be achieved by stacking several levels of pendulums.

In the mid-range of frequencies ($\sim$100 Hz-1 kHz) thermal noise of the masses, mirror coatings and suspensions will dominate. These components are chosen to have natural frequencies of vibration outside the main operating frequency range of the detectors, with the suspensions at a few Hz and masses at several kHz. By choosing materials for these elements with a high quality factor Q, like silica, most of the vibrational energy will be kept to a small frequency range about the natural frequency. The use of high Q materials means that the interferometers can be operated at room temperature, but cooling the detectors is being studied as a possible way of reducing thermal noise in the future.

At high frequencies ($\gtrsim 1\,\mathrm{kHz}$) quantum shot noise is the dominant noise source. The fact that the laser light is made up of quantised photons gives rise to random fluctuations in the number of photons N at the output. This is a Poisson process so the number of photons will vary as $\sqrt{N}$, therefore the fractional error on the fluctuations in the number of photons detected will be reduced by increasing the laser power i.e. increasing N. To get the shot noise down to the low levels needed requires laser powers far higher than any commercially produced lasers reach, so a technique called power recycling must be used. If the interferometer output is kept on a dark fringe, so no power is lost at the output, then the only way for power to escape is through the input, so by placing a mirror in front of the laser this light can be sent back into the cavity (see figure 1.4). As the mirror optics are high quality little power is lost in transmission and the power in the cavity is built up. This means that a 10 W laser is able to give powers of up to several kW in the cavity. The higher power can however lead to radiation pressure noise and thermal heating of the mirror and as such a trade off needs to be made.

All these noise sources combine to mean that current interferometers are most sensitive in the regions of $\sim 10 - 1000\,\mathrm{Hz}$, although all sides of the noise curve can be pushed outwards by applying novel techniques.

Current detectors

This thesis will focus on results from the GEO 600 and LIGO detectors. GEO 600 is a joint British/German 600 m long folded arm Michelson interferometer based near Hannover, with power and signal recycling[3] [30]. The Laser Interferometric Gravitational Wave Observatory (LIGO) project [31] is a US-based set of three Fabry-Perot cavity interferometers: two collocated in Hanford, WA with 4 km and 2 km arm lengths (called H1 and H2 respectively); and one in Livingston, LA (L1), with a 4 km arm length. These detectors make up those used by the LIGO Scientific Collaboration (LSC). All

[3]This is a way of holding light in the cavities for longer at certain frequencies to enhance the sensitivity in a tunable narrow band, and is achieved by introducing another movable mirror at the output to put light back into the cavity.

were under construction and commissioning until they performed their first science run in autumn 2002 (see Abbott *et al.*, 2004c [32]), since when there have been three more science run periods between which commissioning has taken place. The relative design sensitivities of these can be seen in figure 1.2. Due to its smaller size GEO 600 has been a test bed for more advanced technologies than LIGO, like monolithic double suspensions and signal recycling, which will be used in future upgrades to the LIGO instruments i.e. Advanced LIGO.

These detectors are not the only interferometers currently operating. The first large scale interferometer to successfully make measurements was in fact the Japanese 300 m-arm-length TAMA 300 detector. This has since performed several data taking runs. The other main interferometer is the French/Italian 3 km VIRGO detector near Pisa. VIRGO has been designed with a very elaborate suspension system to minimise low frequency noise, giving it an advantage over LIGO and GEO 600 below ~ 50 Hz. VIRGO is still under its commissioning, but should soon join the network of detectors.

Along with the interferometers there are several groups with bar detectors. These include AURIGA, ALLEGRO, EXPLORER and NAUTILUS which have been very active for many years.

Future detectors

For ground-based interferometers plans are very advanced for the upgrade and construction of the next generation. These include the planned upgrade to the current LIGO detectors, by porting some technologies over from GEO 600. These should help lower the noise floor by an order of magnitude (see figure 1.2) and expand the volume of space covered by about a factor of ~ 1000. The Japanese have plans for a new detector possibly using cryogenic technologies to reduce thermal noise. Any upgrades to GEO 600 could see it being focused on the high frequency region using advanced optical techniques to get below the standard quantum noise limits in this region.

One of the most exciting future detectors is the space-based detector, the Laser Interferometer Space Antenna (LISA). This joint ESA/NASA venture aims to put an

interferometer consisting of three spacecraft forming an equilateral triangle of side 5 million km into space. This would be free from gravity gradient noise and have a sensitivity over the frequency range of $\sim 0.1 - 100\,\mathrm{mHz}$. The range of sources in this frequency band should guarantee gravitational wave detection.

1.4 Current searches

As stated above the LSC interferometers have performed several periods of data taking under science mode, these have been: S1 from 23$^{\mathrm{rd}}$ August - 9$^{\mathrm{th}}$ September 2002 with both GEO 600 and the LIGO instruments; S2 from 14$^{\mathrm{th}}$ February - 14$^{\mathrm{th}}$ April 2003 with just the LIGO instruments; S3 from 31$^{\mathrm{st}}$ October 2003 - 9$^{\mathrm{th}}$ January 2004 with LIGO and including GEO 600 for two separate periods; and S4 from 22$^{\mathrm{nd}}$ February - 23$^{\mathrm{rd}}$ March 2005 with both GEO 600 and LIGO. Using data from these runs a variety of searches for a large section of the above sources has been carried out. Here we will briefly summarise some of these results.

In Abbott *et al.* (2004a and 2005a) [33, 34] searches for continuous gravitational waves from known pulsars were performed using data from S1 and S2 setting upper limits on h of $\sim 10^{-24}$ and ellipticities of $\sim 10^{-5}$ for several pulsars (results from the S3 and S4 runs are presented in this thesis). Abbott *et al.* (2005c) [35] shows an all-sky search for continuous gravitational waves from unknown neutron stars or other sources in the 200-400 Hz range using S2 data, with a best upper limit on h of $\sim 4.4 \times 10^{-23}$. Other such all-sky coherent, semi-coherent and incoherent searches are being used on S2 and more recent data, including a targeted search for gravitational waves from the LMXB Sco X1, but these results are as of yet unpublished.

Searches for untriggered burst sources have been performed on LIGO data from S1 and S2 in Abbott *et al.* (2004d and 2005d) [36, 37], giving a best upper limit on the event rate for bursts of between 100-1000 Hz of less than 0.26 per day in the strain amplitude range $h_{\mathrm{rss}} \sim 10^{-20} - 10^{-19}\,\mathrm{Hz}^{-1/2}$[4]. A coincidence burst search between LIGO

[4] $h_{\mathrm{rss}} \equiv \sqrt{\int |h|^2 \mathrm{d}t}$ is the root-sum-squared amplitude spectral density for bursts

and the TAMA 300 detectors during the period of S2 (Abbott *et al.*, 2005e [38]) has given an upper limit of 0.12 events per day above a strain of $h_{\rm rss} \sim 1-3\times10^{-19}\,{\rm Hz}^{-1/2}$ in the frequency range of 700-2000 Hz. In Abbott *et al.* (2005f) [39] a search has targeted a GRB and set an upper limit on the radiation for the specific event GRB030329 using LIGO data. For an event shorter than 150 ms and around 250 Hz this gave a strain amplitude upper limit of $h_{\rm rss} \simeq 6\times10^{-21}\,{\rm Hz}^{-1/2}$. Again burst searches for gravitational waves from more recent runs, including coincidences with GEO 600, have yet to be published.

The search for inspiral events has included binary neutron stars inspiral (Abbott *et al.*, 2004b and 2005g [40, 41]), binary black holes (Abbott *et al.*, 2005h [42]) and primordial black holes in the Galactic halo (MACHOs) (Abbott *et al.*, 2005i [43]). The binary neutron star search had a maximum range of ~ 1.5 Mpc with an event rate upper limit of 47 per year per Milky Way equivalent galaxy (MWEG) for neutron stars in the mass range $1-3\,{\rm M}_\odot$. The binary black hole search found no events out to distances of 1 Mpc for black hole masses between $3-20\,{\rm M}_\odot$, giving an upper limit rate of 38 per year per MWEG. These results are all at 90% confidence and have been set using S2 data with more up to date results to be published.

Finally in Abbott *et al.* (2004e and 2005b) [44, 28] upper limits on the stochastic background have been set using LIGO data from S1 and S3. This has given the increasingly astrophysically interesting upper limit of $\Omega_{\rm gw} < 8.4\times10^{-4}$ in the frequency band 69-156 Hz.

All these upper limits are from LSC detectors. There are also interesting upper limits on burst, continuous wave and stochastic sources from the various bar detector groups. Stochastic upper limits in much lower frequency ranges are also being set via spacecraft doppler tracking and pulsar timing. Summarising all would require a large review paper and is out of the scope presented here. In the future all the various detectors should form a large network, the pooling of data from which will be used to gain the most information about sources and provide the best results.

I hate to go all technical on you, but... all hands on deck, swirly thing alert!

Cat - Red Dwarf

Chapter 2

Gravitational waves from known pulsars

In this chapter we will discuss pulsars as a source of continuous gravitational waves. A search technique and parameter estimation tool for such sources is described. The inclusion of timing noise corrections and binary pulsar time delays into this search is then discussed, along with code validation proceedures.

2.1 Pulsars and gravitational radiation

One class of astrophysical object thought to be a strong candidate for the emission of detectable continuous gravitational waves is neutron stars. These are the ultra-dense evolutionary end states for high mass stars ($\sim 8 - 25\,M_{\odot}$) produced during core-collapse in a Type II supernova, or accretion induced collapse of a white dwarf in a Type I supernova. They were theorised (in the first instance by Baade and Zwicky, 1934 [45]) for several decades before evidence for their existence was confirmed by the discovery of pulsars in 1967 by Hewish and Bell [46]. They discovered periodic coherent radio pulses from outside the solar system. These were consistent with a beamed source of radiation from a rapidly rotating highly magnetic object. The very fast periods seen for the promptly discovered Crab and Vela pulsars ruled out, as sources, already known objects such a white dwarfs as they would have radii greater than the surface of the light

cylinder[1]. This left the far denser and smaller neutron stars as the prime candidate. The pulsed emission was due to an offset between the spin axis and magnetic axis, from which electromagnetic radiation was being beamed, occurring when the magnetic axis crossed our line of sight; in a way analogous to a lighthouse. Since their initial discovery, at the time of writing, 1533 pulsars have been discovered (as given by the Australia Telescope National Facility - ATNF - online pulsar catalogue [47]). The majority have been discovered through radio surveys of the sky, although emission from some objects can be seen across a wide range of energies, even into the γ-ray spectrum. Surveys are ongoing, but estimates of the number of pulsars in the galaxy can be made by inference from the current population, taking into account biasing from selection effects, and the supernova rate. Estimates give values of $\sim 200\,000$ active pulsars within our galaxy (see Lorimer, 2001 [48]).

Pulsars are found in a wide range of environments. As might be expected from their birth in supernovae some are found associated with supernova remnants (SNR). These are typically young pulsars whose birth velocity has not yet caused a large displacement from the remnant, their emissions are still enough to excite the SNR to emit, and the SNR has not dissipated into the interstellar medium (ISM). Other pulsars are found in binary systems as companions to a whole range of bodies ranging from planets, through main sequence stars, to white dwarfs and other neutron stars. The so called millisecond pulsars (pulsars with rotation periods of < 10 milliseconds) are often found within binary systems, and their rotation speed is often attributed to their being spun-up by accretion of material from a stellar companion. Many pulsars are seen within globular clusters, which is not surprising due to the high concentration of old stars. Pulsars are also seen without any association. From here on we shall classify any pulsar not in a binary system as isolated.

The range of spin periods covered by pulsars is quite wide going from ~ 12 seconds to ~ 1.5 milliseconds. The distribution of periods is not uniform with distinct populations of fast millisecond and young pulsars, and slower pulsars.

[1]The surface which would be rotating at the speed of light.

Pulsars are generally seen to spin-down as they lose rotational energy via various emission mechanisms. The generally accepted energy loss is via magnetic dipole radiation. The energy loss mechanism most important for us would be via gravitational radiation. The phase evolution of a pulsar can generally be well described by the Taylor expansion,

$$\phi(t) = \phi_0 + 2\pi \left\{ \nu_0(t - t_0) + \frac{1}{2}\dot{\nu_0}(t - t_0)^2 + \frac{1}{6}\ddot{\nu_0}(t - t_0)^3 + \ldots \right\}, \tag{2.1}$$

where ϕ_0 is the initial phase, ν_0 and its time derivatives are the pulsar frequency and spin-down coefficients at an epoch t_0, and t is the time in a reference frame comoving with the pulsar. For the vast majority of pulsars the value of $\dot{\nu}$ is very small and $\ddot{\nu}$ is unmeasurable or swamped by timing noise (see §2.3). To date there are only five pulsars with well enough sampled observations to have a measurable $\ddot{\nu}$, which allows a quantity called the braking index, $n = \frac{\nu\ddot{\nu}}{\dot{\nu}^2}$, to be defined. For spin down caused by pure magnetic dipole radiation then $n = 3$, and for pure gravitational radiation $n = 5$ (see Palomba, 2000 [49]). For the few pulsars with a measurable value of the breaking index, four (PSR J0534+2200 - the Crab pulsar, PSR J1513-5908, PSR J0835-4510 - the Vela pulsar, and PSR J0540-6919) show $n < 3$ [49] and one (PSR J0537-6910) shows $n \sim 6.9$ [50]. For the four pulsars with $n < 3$ Palomba [49] tries to explain them with a combination of magnetic breaking and gravitational radiation.

Neutron stars are typically thought, from theoretical arguments, to have a mass of around $1.4\,\mathrm{M}_\odot$ and radii of $\sim 10\,\mathrm{km}$. Using these canonical values of mass and radius and assuming a uniform density sphere, the moment of inertia of a neutron star is often quoted as $I = \frac{2}{5}MR^2 = 10^{38}\mathrm{kg\,m^2}$. Their structure is thought to consist of a thin crust of highly distorted heavy nuclei (mostly iron) and a degenerate electron gas, above a mantle of fluid neutrons with some protons and electrons, surrounding a core of neutrons or unbound quarks (this is discussed in more detail in Benhar, 2005 [51]). Densities range from $\sim 10^{10}\,\mathrm{kg/m^3}$ near the surface to $\sim 10^{18}\,\mathrm{kg/m^3}$ in the core. The true nature of the neutron star interior is unknown, with much speculation surrounding the possibility of it consisting of strange quark matter and other exotic

theories. Questions about the equation-of-state could possibly be answered through observations of gravitational waves from neutron stars.

2.1.1 Gravitational wave emission mechanisms

Spinning stars with perfect symmetry about their rotation axis will not emit gravitational waves, so if we expect to detect any continuous gravitational wave signal then some mechanism must be in place to cause an asymmetry to arise. In this section the most important gravitational wave emission mechanism we will discuss is the emission of continuous waves from a triaxial neutron star (in Chapter 4 the emission of transient quasi-normal modes will be discussed).

Emission from a triaxial neutron star

There are several ways in which a neutron star could be deformed from asymmetry. During formation and crystallisation the neutron star crust may be deformed from axisymmetry due to centrifugal forces. This deformation could then be supported by the solid crust [52]. Another possibility is that a strong magnetic field could distort the star. Gravitational waves produced by such mechanisms would be produced at twice the rotation frequency of the star. They would have a characteristic strain amplitude given by

$$h_0 = \frac{16\pi^2 G}{c^4}\frac{\varepsilon I_{zz}\nu^2}{r}, \tag{2.2}$$

where ν is the star's spin frequency, I_{zz} is the principal moment of inertia, ε is the star's ellipticity, and r is the distance to the star (see Jaranowski *et al.*, 1998 [53]). In this chapter and the next we shall only consider gravitational waves emitted via this mechanism.

Emission from a precessing neutron star

Precession of a star about its rotation axis is another source of asymmetry. Gravitational waves generated by precession would have a frequency at the star's rotation frequency, with sidebands ofset by the precession frequency from this for small wobble

angles (Zimmermann and Szedentis, 1979 [54]). In Jones and Andersson (2002) [14] they conclude that gravitational wave amplitudes from such sources are likely to be orders of magnitude below the level of detectability for LIGO, but may be detectable with AdvLIGO.

Other mechanisms

Another source of asymmetry in a star may arise if it is in a binary system and accreting matter from its companion, as in Low Mass X-ray Binaries (LMXBs). Such systems could emit gravitational waves via r-modes as discussed in Andersson *et al.* (1999) [55] or could perhaps have large ellipticities induced by an accretion-confined magnetic field as in Melatos and Payne (2005) [56].

2.1.2 Gravitational wave searches

Known pulsars provide an enticing target for gravitational wave searches. With known positions and frequencies the parameter space to search over can be much smaller than for unknown searches. The fact that the waves are continuous means that, assuming a coherent search, you can build up signal-to-noise with longer observations (scaling as $\sqrt{T}$, where T is observation time). The main drawback in a search for gravitational waves for the majority of known pulsars is that the level of emission can be inferred to be much lower than current detector sensitivities. It is possible using existing radio measurement to set an upper limit on gravitational wave emission amplitudes from energy conservation arguments, assuming there is no unknown mechanism powering the star in some way. If one assumes that all the kinetic energy lost as the pulsar spins-down is dissipated via gravitational radiation ($\mathrm{d}E_{\mathrm{gw}}/\mathrm{d}t = 4\pi^2 I_{zz}\nu|\dot{\nu}|$) then an upper limit on h_0 can be set as

$$h_0^{\mathrm{spin-down}} = \left(\frac{5}{2}\frac{GI_{zz}\dot{\nu}}{c^3 r^2 \nu}\right)^{1/2}, \tag{2.3}$$

this will be discussed in more detail in §3.5. Even so, searches do provide upper limits on emission which can be valuable in constraining certain equations of state, and we may just find something!

The ability to search for gravitational waves from known pulsars before the advent of the large scale interferometric detectors was rather limited. Bar detectors are only sensitive in a narrow band of frequencies around their resonant frequencies and so cannot be used to target objects outside that band. A specific attempt to search for gravitational waves from the Crab pulsar at a frequency of $\sim 60.2\,\mathrm{Hz}$[2], was made with a specially designed aluminium quadrupole antenna (see Hirakawa *et al.*, 1978 and Suzuki, 1995 [57, 58]). A search for gravitational waves from the then fastest millisecond pulsar, PSR J1939+2134, was conducted by Hough *et al* (1983) [59] using a split bar detector, producing an upper limit of $h_0 < 10^{-20}$.

Using the inherently broadband interferometers a larger sample of objects is accessible. The first search for gravitational waves from a pulsar using an interferometer was with the prototype 40 m interferometer at Caltech by Hereld (1983) [60]. Again the search was for gravitational waves from PSR J1939+2134, and produced upper limits of $h_0 < 3.1\times10^{-17}$ and $h_0 < 1.5\times10^{-17}$ for the first and second harmonics of the pulsar's rotation frequency. For the LIGO instruments all pulsars with rotation frequencies $> 25\,\mathrm{Hz}$ (gravitational wave frequency $> 50\,\mathrm{Hz}$) are accessible. Below this frequency the seismic noise floor rises sharply giving far less stationary data and sensitivities well below sensible levels. This generally leaves only the population of millisecond and young pulsars accessible, consisting of 150 pulsars at the time of writing (from the ATNF catalogue [47]). The low frequency sensitivity of the VIRGO detector may in the future allow the probing of a larger sample of pulsars at lower frequencies.

Current searches

The search for gravitational waves from known pulsars has developed rapidly since the start of data taking runs with the LIGO and GEO 600 interferometers in 2002.

[2]twice its rotation frequency at the time of their search, although the frequency now searched is closer to $\sim 59.6\,\mathrm{Hz}$.

Data from the first science run (S1) was used to perform a search for gravitational waves from PSR J1939+2134, assuming a triaxial star emitting at twice the rotation frequency [33]. For this search two techniques were used: one a frequency domain, frequentist search, and the other a time domain, Bayesian search.

The frequency domain method and others

The frequency domain search makes use of Fourier transforms of the data to search for a signal in the correct frequency bin using a detection statistic ($\mathcal{F}$-statistic [53]). This statistic is based on a maximum-likelihood analysis, making use of the output of matched-filters (more on matched filtering is given in §4.2.1) for a series of templates over the pulsar signal parameters. An upper limit using this statistic can be set using Monte-Carlo injections and establishing a threshold which gives a certain false alarm rate and false dismissal rate.

There are efforts to search for gravitational waves from neutron stars by a variety of other methods in the LSC using LIGO and GEO 600 data from the last four science runs. The use of the Hough transform method can be seen in Abbott *et al.* (2005c) [35], the StackSlide method is described in Mendell (2005) [61], and the PowerFlux method is described in Dergachev (2005) [62]. These generally make use of short Fourier transformed stretches of data to form something analogous to a time-frequency spectrogram. Techniques are used to modulate this in a way consistent with the expected gravitational wave form. The spectrogram is then searched for evidence of a signal using a variety of pattern recognition procedures.

These methods do not rely on precise knowledge of the signal phase evolution like the time domain method. This lends them to uses in all-sky searches over large frequency and spin-down ranges rather than being used to target specific objects. They can also be used in targeted searches for objects with badly constrained parameters, for example the search for gravitational waves from the LMXB systems. These strategies can also be used in hierarchical searches as described in Brady and Creighton (2000) [63], whereby wide area searches provide possible signal candidates for a more tightly

focused follow up search. Coincidences between candidates in different detectors can also be applied.

For the analysis of the second science run (S2) of the LIGO interferometers the first attempt to search for a broad range of pulsars was made. Twenty eight pulsars with either very well defined and stable parameters or with new timing taken over the period of S2 were searched for [34]. All these pulsars were isolated. For this search a slightly modified version of the time domain method of S1 was used. It is this search method which will be discussed in more detail below and which has been used to obtain the results herein.

Another method making use of the time domain technique and Markov Chain Monte Carlo (MCMC) statistical methods is also being explored for possible "fuzzy" targeted searches where some signal parameters are badly constrained (see Veitch *et al.*, 2005 [64]). An MCMC approach provides a way of intelligently exploring large parameter spaces without having to exhaustively cover the entire range. An example of an object for which such a search is being applied is a potential pulsar remnant of SN1987A (a supernova which occurred in the LMC in 1987), as speculatively observed by Middleditch *et al.* (2000) [65], where the pulsar frequency and spin-down are uncertain within a small range. Problems with this technique are that it does not naturally lend itself to producing an upper limit (rather than a detection), although further study is going into this area.

2.2 Time domain search method

The time domain method described here is described more fully in Dupuis (2004) and Dupuis and Woan (2005) [66, 1]. The extensions to this included here are the additions of timing noise corrections and binary system effects into the model. We receive data from the gravitational wave sensitive channels of the LIGO and GEO 600 interferometers. For LIGO data this is received in an uncalibrated form (raw voltages from the instrument output) with frequency domain calibration information supplied separately (calibration will be discussed in more detail in Chapter 3). For GEO 600 time series data

is supplied in a calibrated form, making post-processing calibration unnecessary. All data is received at a sampling rate of 16 384 Hz. This sampling rate means a frequency range of 8192 Hz is available for searches. In known pulsar searches the frequency is known very precisely, so the vast majority of this frequency space is redundant. A way to down-sample this large bandwidth of data is useful to increase the speed of any search. Knowledge of the pulsar parameters allows us to perform a heterodyne on the data and down-sample it to $\frac{1}{60}$ Hz (one sample per minute), as described later.

The expected signal from a pulsar is given by

$$h(t) = \frac{1}{2}F_+(t;\psi)h_0(1+\cos^2\iota)\cos 2\phi(t) + F_\times(t;\psi)h_0\cos\iota\sin 2\phi(t), \tag{2.4}$$

where $\phi(t)$ is that given in equation 2.1, F_+ and $F_\times$ are the detector beam patterns for the plus and cross polarisations of the gravitational waves, ψ is the wave polarisation angle, and ι is the angle between the rotation axis of the pulsar and the line-of-sight. For a gravitational wave signal impinging on the Earth the signal arrival time at the detector, t, given in equation 2.1 will be modulated by Doppler, time delay and relativistic effects caused by the motions of the Earth and other bodies in the solar system. Therefore,

$$t_b = t + \delta t = t + \frac{\mathbf{r}\cdot\hat{\mathbf{n}}}{c} + \Delta_{E_\odot} + \Delta_{S_\odot}, \tag{2.5}$$

where $\mathbf{r}$ is the position of the detector with respect to the solar system barycentre (SSB), $\hat{\mathbf{n}}$ is the unit vector pointing to the pulsar, $\Delta_{E_\odot}$ is the special relativistic Einstein delay, and $\Delta_{S_\odot}$ is the general relativistic Shapiro delay. This corrects the signal to the SSB time t_b. This reference frame is assumed to be at rest with respect to the pulsar, with its proper motion generally being negligible. For pulsar's in binary systems there will be additional time delays as discussed in §2.4.

We assume that our gravitational wave detector data is given by

$$s(t) = h(t) + n(t), \tag{2.6}$$

where $h(t)$ is the gravitational wave signal and $n(t)$ is the noise. In searching for a

particular pulsar we can perform a complex heterodyne of the data by multiplying it by $e^{-i2\phi(t_b)}$, where $\phi(t_b)$ is the phase evolution of that pulsar given by equation 2.1, and t_b from equation 2.5. The pulsar signal (equation 2.4) can be rewritten using trigonometric identities as

$$h(t) = A_1(t)e^{i2\phi(t_b)} + A_2(t)e^{-i2\phi(t_b)}, \tag{2.7}$$

where

$$A_1(t) = \frac{1}{4}F_+(t;\psi)h_0(1+\cos^2\iota)e^{i2\phi_0} - \frac{i}{2}F_\times(t;\psi)h_0\cos\iota e^{i2\phi_0}, \tag{2.8}$$

and

$$A_2(t) = \frac{1}{4}F_+(t;\psi)h_0(1+\cos^2\iota)e^{-i2\phi_0} + \frac{i}{2}F_\times(t;\psi)h_0\cos\iota e^{-i2\phi_0}, \tag{2.9}$$

and ϕ_0 is the initial phase of the gravitational wave signal from the pulsar. Performing the heterodyne on the signal transforms

$$s(t) \to s(t)e^{-i2\phi_0} = s_{\rm het}(t) = (h(t)+n(t))e^{-i2\phi_0} = A_1(t) + A_2(t)e^{-i4\phi(t_b)} + n(t)e^{-i2\phi(t_b)} \tag{2.10}$$

which removes the phase evolution from the A_1 term and increases the oscillation of the A_2 term to twice the gravitational wave frequency. $A_1(t)$ will now only oscillate at the diurnal rate of the detector antenna pattern. The slow rate of change of the antenna pattern means that the data can be significantly down-sampled by averaging from 16 384 Hz to $\frac{1}{60}$ Hz. We call each minute sample B_k where k is the sample number. Before this averaging takes place it is prudent to low-pass filter the data to prevent aliasing from other bands contaminating the pulsar signal band. The filters used are three consecutive third order Butterworth infinite impulse response (IIR) filters, with a cut-off frequency of $\frac{1}{2}$ Hz. This should also effectively suppress the fast oscillating $A_2(t)$ term. After filtering, the data can then be averaged to give

$$B_k = \frac{1}{M}\sum_{i=1}^{M} s'_{\rm het}(t_i), \tag{2.11}$$

where $s'_{\rm het}$ is the filtered heterodyned data and $M = 16\,384\,\mathrm{Hz} \times 60\,\mathrm{s} = 983\,040$. The averaging will also act as another level of low pass filtering. In this approach the pulsar phase and therefore solar system barycentring time delays need to be calculated for every sample of data at 16 384 Hz. This can be computationally expensive, but does mean that the filter cut-off frequencies can be tight and the data averaged to a low rate. If the pulsar parameters were not well known, so that the signal could drift across the heterodyned band, then the filter cut-offs and re-sampling rate might need to be increased. This can be done on purpose to try to reduce the computation time. For example an initial heterodyne using a phase calculated with just the pulsar frequency and without the barycentring can be carried out. The data can then be re-sampled to, say, 4 Hz and re-heterodyned with the frequency derivatives and barycentre timing corrections included. When performing such an analysis for a few pulsars the former strategies' computational time is not too constraining, but for many pulsars it can become quite inefficient.

2.2.1 Bayesian analysis

Once the data has been heterodyned we are left with the complex value

$$B_k = \frac{1}{4}F_+(t_k;\psi)h_0(1+\cos^2\iota)e^{i2\phi_0} - \frac{i}{2}F_\times(t_k;\psi)h_0\cos\iota e^{i2\phi_0} + n(t_k)', \tag{2.12}$$

where $n(t_k)'$ is the heterodyned averaged noise for the $k^{\rm th}$ sample. We want to somehow search for the signal buried in this noise. This signal is defined by the four unknown parameters of h_0, ψ, ι and ϕ_0.

To search for the signal we use a Bayesian parameter estimation method. Two slightly different approaches to this are considered in Dupuis (2004) [66], one in which the noise variance is estimated from the data and one in which the noise variance is considered to be unknown. Here we will concentrate on the latter method. Bayesian statistics make use of the basic rules of probability theory, namely the product rule

and the sum rule. Application of these leads to Bayes' theorem,

$$p(x|y,I) = \frac{p(y|x,I) \times p(x|I)}{p(y|I)}, \tag{2.13}$$

where $p(x|y,I)$ is called the posterior probability distribution function (pdf) of x given y, $p(y|x,I)$ is the likelihood function of y given x, $p(x|I)$ is the prior probability distribution of x.

In our search we start off with the Gaussian likelihood function as representing the likelihood of each complex B_k,

$$p(B_k|\mathbf{a},\sigma_k) = \frac{1}{(\sigma_k\sqrt{2\pi})^2} \exp\left(-\frac{|B_k - y_k|^2}{2\sigma_k^2}\right), \tag{2.14}$$

where $\mathbf{a} = \{h_0, \psi, \iota, \phi_0\}$, $y_k = B_k - n(t_k)'$ is our model, and σ_k is the standard deviation of the noise in B_k. It is shown in Bretthorst (1988) [3] that such a likelihood function is the least informative. This is not to say that it is a bad likelihood function to use, but just means that it is expressing the least prior information on what the distribution looks like. If we assume that the noise in each B_k is independent then our complete likelihood for the whole set of data can be given by the product of all the Gaussians,

$$p(\{B_k\}|\mathbf{a},\{\sigma_k\}) = \left(\prod_{k=1}^{n} \frac{1}{(\sigma_k\sqrt{2\pi})^2}\right) \exp\left(-\sum_{k=1}^{n} \frac{|B_k - y_k|^2}{2\sigma_k^2}\right), \tag{2.15}$$

where n is the number of B_ks. In the search of Abbott *et al.* (2004a) [33] this likelihood was used with the standard deviation of each B_k calculated before the down-sampling took place. In a strict sense the Gaussian likelihood should only be used when the noise level is known in advance, whereas in [33] it was estimated from the data. This can lead to non-negligible uncertainties in σ when the number of data points used to estimate it is low. In subsequent searches [34, 66] the above likelihood was adapted for the case where the noise variance was unknown. This is achieved by taking the variance as an unknown nuisance parameter and marginalising over it for segments of data when the noise level can be assumed to be stationary. If we split the n B_ks into

M segments of length m_j with the same noise level then

$$n = \sum_{j=1}^{M} m_j. \tag{2.16}$$

The likelihood for each segment j can be rewritten as

$$\begin{aligned} p(\{B_k\}_j|\mathbf{a}) &\propto \int_0^\infty p(\{B_k\}_j, \sigma_j|\mathbf{a})\mathrm{d}\sigma_\mathrm{j} \\ &\propto \int_0^\infty p(\sigma_j|\mathbf{a}) p(\{B_k\}_j|\mathbf{a}, \sigma_j)\mathrm{d}\sigma_\mathrm{j}, \end{aligned} \tag{2.17}$$

where $p(\sigma_j|\mathbf{a})$ is the prior on the noise floor and the likelihood is the Gaussian likelihood given in equation 2.15. As σ_j is a scale parameter the least informative prior on it is the Jeffreys' prior (uniform in log space)

$$\begin{aligned} p(\sigma_j|\mathbf{a}) &\propto \tfrac{1}{\sigma_j} \quad (\sigma_j \geq 0), \\ &= 0 \quad (\sigma_j < 0). \end{aligned} \tag{2.18}$$

Combining the prior in equation 2.18 with equation 2.17 gives a likelihood integral

$$p(\{B_k\}_j|\mathbf{a}) \propto \int_0^\infty \frac{1}{\sigma_j^{2m_j+1}} \exp\left(-\frac{1}{2\sigma_j^2}\sum_{k=1}^{m_j}|B_k - y_k|^2\right)\mathrm{d}\sigma_\mathrm{j}. \tag{2.19}$$

This integral can be solved analytically following the procedure given in [66]. Making the substitutions

$$\begin{aligned} u^2 &= \frac{\sum |B_k - y_k|^2}{2\sigma_j^2}, \\ \mathrm{du} &= -\frac{\sqrt{\sum |B_k - y_k|^2}}{\sqrt{2}\sigma_j^2}\mathrm{d}\sigma_\mathrm{j}, \end{aligned} \tag{2.20}$$

and rearranging as

$$\begin{aligned} \frac{1}{\sigma_j} &= \frac{\sqrt{2}u}{\sqrt{\sum |B_k - y_k|^2}}, \\ \frac{\mathrm{d}\sigma_\mathrm{j}}{\sigma_j^2} &= \frac{1}{\sqrt{2\sum |B_k - y_k|^2}}\mathrm{du}, \end{aligned} \tag{2.21}$$

gives an integral of the form

$$p(\{B_k\}_j|\mathbf{a}) \propto 2^{m_j}\left(\sum |B_k - y_k|^2\right)^{-m_j} \int e^{-u^2} u^{2m_j-1}\mathrm{du}, \tag{2.22}$$

the solution to which is

$$\begin{aligned} p(\{B_k\}_j|\mathbf{a}) &\propto 2^{m_j-1}\left(\sum |B_k - y_k|^2\right)^{-m_j} m! \\ p(\{B_k\}_j|\mathbf{a}) &\propto \left(\sum |B_k - y_k|^2\right)^{-m_j}. \end{aligned} \tag{2.23}$$

This approximates a Student's t-distribution with $2m_j - 1$ degrees of freedom. As the number of degrees of freedom increase this will tend towards a Gaussian distribution. To get a joint likelihood for the whole data set of n points we can use the product rule to combine the likelihoods of each segment j giving

$$p(\{B_k\}|\mathbf{a}) \propto \prod_j^M p(\{B_k\}_j|\mathbf{a}). \tag{2.24}$$

Once we have this likelihood we can use Bayes' theorem to start estimating the posterior probability distributions of the various signal parameters. For this we need to set priors for each of our signal parameters. For the four parameters we use a uniform prior over their ranges: ϕ_0 over $[0, 2\pi]$, ψ over $[-\pi/4, \pi/4]$, ι in terms of $\cos\iota$ over $[-1, 1]$ and h_0 over $[0, \infty]$. These are the least informative priors for ϕ_0, ψ and $\cos\iota$, but that for h_0 is just a compromise solution. With h_0 being a scale factor the Jeffreys' prior would provide the least informative prior, but as this is improper (non-normalisable) one would not be able to use it to set an upper limit. Such a prior would also have the effect of overwhelming the likelihood of the data, meaning we would not be updating

our knowledge from the experiment. One could also say that the spin-down upper limits provide a prior on h_0, but with this, for most pulsars, being at a much lower level than our noise floor means that we learn nothing from the experiment. The compromise solution of a uniform prior allows us to normalise our posterior probability and means that our solution just represents the sensitivity of the detector. It is in reality just a more conservative value than that which could be obtained with more realistic priors.

Using these priors and our likelihood function we can produce a 4-dimensional posterior pdf

$$p(h_0, \phi_0, \psi, \cos\iota|\{B_k\}) \propto p(\{B_k\}|h_0, \phi_0, \psi, \cos\iota)p(h_0)p(\phi_0)p(\psi)p(\cos\iota). \quad (2.25)$$

This contains all the probability information, but can be hard to interpret. For the case of setting upper limits on h_0 the angle parameters can be considered as nuisance parameters and be computationally marginalised over

$$p(h_0|\{B_k\}) \propto \int_{\phi_0=0}^{\phi_0=2\pi} \int_{\psi=-\pi/4}^{\psi=\pi/4} \int_{\cos\iota=-1}^{\cos\iota=1} p(h_0, \phi_0, \psi, \cos\iota|\{B_k\})\mathrm{d}\phi_0\mathrm{d}\psi\mathrm{d}\cos\iota. \quad (2.26)$$

If a signal is detected then the same sort of marginalisation can be used to extract pdfs of the other parameters (as will be seen for signal injections in Chapter 3). Using the pdf for h_0 an upper limit on the signal amplitude can be set by marginalising from zero up to the degree of belief required. We generally give a 95% degree of belief upper limit, where $h_0^{95\%}$ is calculated from

$$0.95 = \int_{h_0=0}^{h_0^{95\%}} p(h_0|\{B_k\})\mathrm{dh}_0. \quad (2.27)$$

Such an upper limit can always be set even if there is signal present.

This analysis can easily be extended into a multi-detector analysis by combining the data sets from several detectors. As long as the data sets are independent the product rule can just be used to combine the likelihoods for each detector. The detectors also need to be coherent as any phase offsets between them can completely ruin the result,

with the possibility of nullifying a real signal if they are π out of phase (the validity of the detectors phase coherence is discussed more in Chapter 3 with relation to signal injections). If there are n detectors of equal sensitivity and the data sets are of equal length this can be considered equivalent of having one detector with n times the data length, with an increase in signal-to-noise (S/N) of $\sqrt{n}$. In practice using the network of detectors in the LSC, there can be quite large differences in sensitivity and live time, meaning that the most sensitive detector will dominate any multi-detector analysis. As the detectors become more comparable this becomes a useful technique in increasing S/N and has already been used in [34].

2.3 The problem of timing noise

Pulsars are generally very stable over periods of several days, but there are phenomena which can show up deviations in this timing stability. With the very high accuracy of pulsar timing any random timing irregularities will start to become evident. One such phenomenon is that of timing noise. This phenomenon has been known about since the early days of pulsar observations and represents a random walk in phase, frequency or frequency derivative of the pulsar about the regular spin-down model given in equation 2.1 [67]. The strength of this effect has been quantitatively defined, in Cordes and Helfand (1980) [67] as the activity parameter A, as referenced to that of the Crab pulsar, and in Arzoumanian *et al* (1994) [68] as the stability parameter Δ_8. A is based on the logarithm of the ratio of the rms residual phase of the pulsar, after removal of the timing model, to that of the Crab pulsar over an approximately 3 year period. Δ_8 provides a more absolute measure not being based on the stochastic nature of the Crab pulsar's timing noise and being defined for a fixed time (10^8 s) as

$$\Delta_8 = \log\left(\frac{1}{6\nu}|\ddot{\nu}| \times (10^8\,\mathrm{s})^3\right). \tag{2.28}$$

This quantity has the oddity that it is the logarithm of a value with the dimensions of seconds, as it is supposed to represent the pulsar clock error. A more appropriate value

for us to use is the phase residual which would be obtained by removing ν from the equation, or the fractional phase residual by using $(10^8\mathrm{s})^2$. Even so we will continue to use the Δ_8 parameter for comparison to the literature, but when used shall quote the actual phase residual. There is a definite correlation between these parameters and the pulsar's spin-down rate, therefore possibly the pulsar's age. Young pulsars, like the Crab pulsar, generally show the most timing noise activity. The categorisation of the type of timing noise (i.e. phase, frequency or frequency derivative) in Cordes and Helfand (1980) [67] allowed them to ascribe different processes for each. The majority of pulsars studied showed frequency-type noise, possibly a result of random fluctuations in the stars moment of inertia. The actual mechanism behind the process is still unknown, with Cordes and Greenstein (1981) [69] positing and then ruling out several mechanisms inconsistent with observations.

Any timing noise intrinsically linked to the rotation of the pulsar, as opposed to motions of the electromagnetic emission source or fluctuation in the magnetosphere, could be important in the search from gravitational waves from the object. The implications of timing noise with respect to a gravitational wave search is discussed in Jones (2004) [70]. The three categories of timing nose would each have a different effect on any search. If, as is thought most likely, all parts of the neutron star are strongly coupled on short timescales then there should be no difference between the electromagnetic phase and gravitational wave phase (as expected if timing noise is frequency-type noise). If the timing noise were purely a magnetospheric fluctuation then phase wandering caused by timing noise would not be seen in the gravitational wave emission. The third possibility, whereby the electromagnetic emission source wanders, would result from a weak exchange of angular momentum between the parts of the star responsible for electromagnetic and gravitational wave emission. This would be seen as a factor, representing the ratio of moments of inertia of the two parts of the star $\alpha = I_{\mathrm{em}}/I_{\mathrm{gw}}$, between the electromagnetic and gravitational wave timing noise phase [70]. In principle this factor could be included as another search parameter, but in general we will take this factor to be 1 as in the case of frequency noise. As we need

very precise knowledge of the phase evolution of a pulsar for our analysis anything that could lead to a drift in phase from the simple Taylor expansion model needs to be addressed. The majority of pulsars though, show timing noise at levels which would not affect our analysis.

As previously stated the level of timing noise is proportional to the pulsar spin-down rate/age. Of the pulsars analysed in Chapter 3 the Crab pulsar is the youngest. The problem of timing noise will be discussed more with respect to how it is countered for this pulsar. The method was used in Abbott *et al.* (2005a) [34], but has not previously been described in detail. A more detailed look into the effects of timing noise for other pulsars will be discussed later.

2.3.1 Timing noise in the Crab pulsar

A pulsar was discovered in the Crab nebula (M1) in 1968 and since then it has been one of the most intensively studied pulsars. It has been observed across the whole range of the electromagnetic spectrum since the initial radio and optical observations. Its parameters are given in table 2.1 as taken from the ATNF catalogue [47]. The

Table 2.1: The parameters of the Crab pulsar given in the ATNF catalogue.

PSR J0534+2200	
Right ascension α	$05^{\mathrm{h}}34^{\mathrm{m}}31^{\mathrm{s}}.973$
Declination δ	$22°00'52''.06$
proper motion in α	-13 mas/yr
proper motion in δ	7 mas/yr
Position epoch	MJD 40675
ν	30.2254370 Hz
$\dot{\nu}$	-3.86228×10^{-10} Hz/s
$\ddot{\nu}$	1.2426×10^{-20} Hz/s^2
Frequency epoch	MJD 40000
Distance	2.0 kpc

Crab pulsar (J0534+2200) is the youngest known pulsar, with an actual age of 951 years (the formation of the Crab nebula is associated with a supernova observed in AD 1054). A spin-down age can also be calculated at $-\nu/2\dot{\nu} = P/2\dot{P} = 1250$ years. The

Crab pulsar is also one of the few in which a value of $\ddot{\nu}$ can be accurately measured, allowing a value of the braking index, $n \sim 2.5$, to be calculated. Analyses of long-term timing observation of the Crab pulsar are given in Lyne *et al.* (1993) [71] and Wong *et al.* (2001) [72]. These analyses show some of the timing features which make the Crab pulsar such an interesting object: the timing noise and glitches.

Since 1982 there has been a regular monitoring program of the Crab pulsar at Jodrell Bank Observatory, and timing ephemerides from this are publicly available online [73]. The ephemeris gives the pulsar frequency and frequency derivative and associated errors, and the associated epoch. The epochs, generally given on the 15^{th} of each month, represent the time of the peak of the first pulse after midnight on that day. They therefore represent zero of modulus phase of the electromagnetic pulse. Notes are given in the event of a timing irregularity or glitch being observed. Using the online ephemeris it is possible to show the timing noise of the pulsar (figure 2.1) by fitting the frequency (up to second order) to the simple Taylor expansion of equation 2.1. The section of data used was chosen to be free of glitches as these cause a step change in the frequency and frequency derivative, which generally fall back to pre-glitch values, but can induce a permanent change. The parameters of the fit are given in table 2.2.

Figure 2.1 compares well the that given in Lyne *et al.* (1993) [71], although some

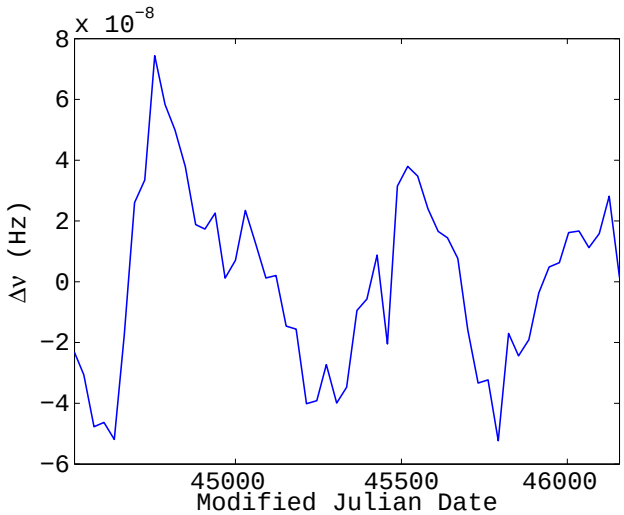

Figure 2.1: The timing noise in the frequency of the Crab pulsar after removing a quadratic fit to the frequency as given in the Jodrell Bank ephemeris. Fit parameters are given in table 2.2.

Table 2.2: Parameters of fit for Crab pulsar frequency.

PSR J0534+2200	
ν	$30.05922413656965\,\mathrm{Hz}$
$\dot{\nu}$	$-3.809951556460455\times10^{-10}\,\mathrm{Hz/s}$
$\ddot{\nu}$	$1.207087526259945\times10^{-20}\,\mathrm{Hz/s^2}$
Frequency epoch	MJD 45015

difference can be expected due to the different lengths of data and epochs used in the fitting. It can be seen that on scales of several months there is quite a large variation in the timing residual (including a possible 20 month quasi-sinusoidal periodicity shown in Lyne *et al.*, 1988 [74]). It is shown in [71] that on smaller time scales the variation is far smoother. The question that needs asking is whether a single model fit for the Crab pulsar is going to be good enough to track the phase without significant phase wandering, or whether the timing noise will mean that such a simple model would be too inaccurate to track the phase. In Jones (2004) [70] a decoherence timescale, $T_{\mathrm{decoherence}}$, is constructed as the time over which the timing noise will cause the phase to deviate by 1 radian from the second order Taylor expansion of phase. This makes use of the "activity parameter" and is calculated for the Crab pulsar to be ~ 2.6 years. Using the activity parameter as a measure of $T_{\mathrm{decoherence}}$ can be imprecise as it is not a fixed quantity and will vary with the model fit epoch and time-span. The activity parameter will also not account for any permanent changes to spin-down caused by glitches. $T_{\mathrm{decoherence}}$ should therefore not be taken as a hard and fast value to adhere to. Another estimate of the effects of timing noise can also be made using the Δ_8 parameter, although for the Crab pulsar its value as derived from equation 2.28 is not altogether useful. This is because for the Crab pulsar, unlike most other pulsars, timing noise is not the dominant component in $\ddot{\nu}$, but is more a feature of even higher order terms (although for the Crab pulsar even an intrinsic non-timing noise dominated value of $\dddot{\nu}$ can be measured to an accuracy of 10% [75]). In Arzoumanian *et al.* (1994) [68]

they fit a linear relation between Δ_8 and $\log \dot{P}$ as

$$\Delta_8 = 6.6 + 0.6 \log \dot{P}, \tag{2.29}$$

where $\dot{P} = -\dot{\nu}/\nu^2$ is the period derivative, which we can use for the Crab pulsar instead. This gives $\Delta_8 \approx -0.8$ which relates to a timing noise cumulative time offset of $\sim 0.15\,\mathrm{s}$ or a phase offset of $\sim 4.4\,\mathrm{cycles}$ over a period of approximately three years. A larger value than $T_{\mathrm{decoherence}}$ suggests.

It is reasonable that if a third order model for the Crab pulsar phase was fit over a period of a few months, then it should fairly accurately represent the phase in that set of data. It is when the stretch of data you need to cover extends for longer than this that such a fit breaks down. However the Crab pulsar ephemeris provides timing every month, which should be sufficient to update the model. By using the phase, frequency and frequency derivative for each entry in the ephemeris as boundary conditions to a set of simultaneous equations the full phase evolution between each month can be calculated, giving a fifth order equation,

$$\begin{aligned}\phi_{5^{\mathrm{th}}}(t_b) &= \phi_0 + 2\pi\left\{\nu_0(t_b - t_0) + \frac{1}{2}\dot{\nu}_0(t_b - t_0)^2\right. \\ &\left. + \frac{1}{6}\ddot{\nu}_0(t_b - t_0)^3 + \frac{1}{24}\dddot{\nu}_0(t_b - t_0)^4 + \frac{1}{120}\ddddot{\nu}_0(t_b - t_0)^5\right\}.\end{aligned} \tag{2.30}$$

For most of the time this method might well be unnecessarily complicated and a simple linear interpolation between months would be sufficient.

In terms of how this affects the analysis in §2.2 it can be made equivalent to performing an extra heterodyne step as described in Pitkin and Woan (2004) [76]. In the initial heterodyne a third order fit to the the phase is used, with values of ν and $\dot{\nu}$ taken from the ephemeris at the closest time *before* the time of the data to be analysed, and $\ddot{\nu}$ taken from the ATNF pulsar catalogue [47]. Then, assuming for the moment that any gravitational wave signal would also show timing noise, we apply a second heterodyne

using the phase difference between equations 2.1 and 2.30

$$B'_k = B_k e^{-i2[\phi_{5\text{th}}(t_b)-\phi(t_b)]}. \tag{2.31}$$

This step can be performed on the B_ks after the filtering and down sampling as the rate of change of this phase difference will be very slow.

The effect of this extra heterodyne can be seen using the example of the S2 analysis. This science run of the LIGO interferometers lasted approximately two months and overlapped three entries in the Crab pulsar ephemeris. The S2 run started on 14$^{\text{th}}$ Feb 2003, so values of the frequency and spin-down used in the initial heterodyning were chosen to be those given in the first ephemeris entry prior to the run (15th Jan 2003). The second derivative was set to be that taken from the ATNF catalogue. The values shown in table 2.3 were multiplied by two to give the gravitational wave frequency. Once the B_ks were produced the ephemeris values were used to calculate the phase

Table 2.3: The parameters used in the initial heterodyne stage of the Crab pulsar analysis for S2.

PSR J0534+2200	
ν	29.8102713888 Hz
$\dot{\nu}$	-3.736982×10^{-10} Hz/s
$\ddot{\nu}$	1.2426×10^{-20} Hz/s^2
Frequency epoch	GPS 726624013

given in equation 2.30. The difference between the initial heterodyne phase and the 5$^{\text{th}}$ order phase is shown in figure 2.2. This phase difference is used in the extra heterodyne to remove the variation. It can be seen in figure 2.2 how a linear fit between ephemeris values would be acceptable for these times, with only small deviations in phase from the fifth order fit. The black crosses in figure 2.2 provide the first step in checking the code used for the extra heterodyne stage. The red points represent the phase difference used in our extra heterodyne step (equation 2.31) to heterodyne each S2 data point as calculated using our code, whereas the black crosses just show the phase difference between the initial heterodyne and the individual Crab pulsar ephemeris data points. The fact that these overlap provides a check that the heterodyne code is

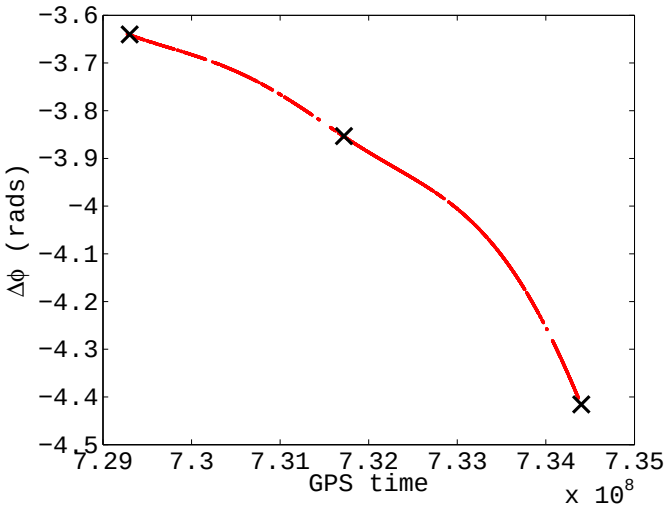

Figure 2.2: The red points show the phase difference between that used in the initial heterodyne and that interpolated from a fifth order fit to the ephemeris. The black crosses show just the phase difference between the initial heterodyne and the individual ephemeris values.

producing the correct phase difference. A second step in checking the code is to make sure it introduces no spurious phase or amplitude changes to the B_ks. We can check the ratio of the magnitudes of the B_ks before and after the timing noise heterodyne, $|B_{k\ \mathrm{before}}|/|B_{k\ \mathrm{after}}|$. This ratio is equal to 1, bar tiny numerical noise, showing that there are no unexpected amplitude changes introduced. We can also check that we can recover the phase correction, $\Delta\phi(t) = 2[\phi_{5^{\mathrm{th}}}(t_b) - \phi(t_b)]$, using the B_ks before ($a = B_k$) and after ($b = B_k e^{-i\Delta\phi}$) the timing noise heterodyne is applied and the relation

$$\frac{a \cdot b^*}{a \cdot a^*} = \frac{B_k \cdot B_k^* e^{i\Delta\phi}}{B_k \cdot B_k^*} = e^{i\Delta\phi}. \tag{2.32}$$

Using the identity $e^{i\Delta\phi} = \cos\Delta\phi + i\sin\Delta\phi$ the original phase correction can be extracted. This extracted phase is shown in figure 2.3 and can be seen to be identical to that calculated and shown in figure 2.2.

If we simulate a signal from the Crab pulsar over the period of S2 with the following parameters, $h_0 = 0.5$, $\phi_0 = 0.0$, $\psi = 0.0$ and $\iota = \pi$, we can see how including a timing noise heterodyne step affects the parameter estimation. Figure 2.4 shows the extracted values of h_0 and ϕ_0 for the signal with and without the timing noise removed. It can be seen that there is very little difference between the amplitudes for the two cases,

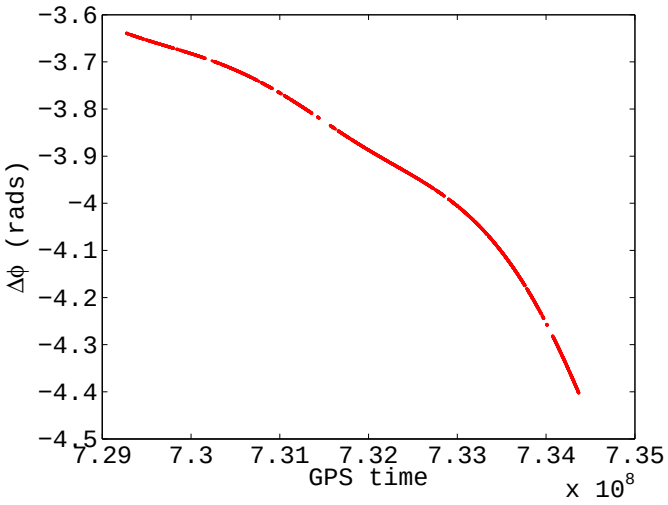

Figure 2.3: The timing noise phase correction as extracted from the B_ks before and after heterodyning.

due to the slope of the phase difference $\Delta\phi$ not being too steep over the period of S2. However, the extracted value of the phase is affected quite heavily, mainly due to

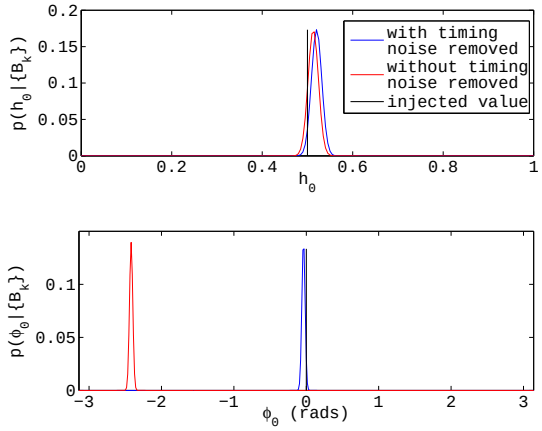

Figure 2.4: The extracted pdfs for h_0 and ϕ_0 for a simulated signal from the Crab pulsar over the period of S2 with and without timing noise removed.

the the phase offset between the start of S2 and the epoch of the initial heterodyne parameters seen in figure 2.2.

We can simulate a Crab pulsar signal and analyse it with and without the timing noise heterodyne step over greater periods than just S2 to show its importance. The same process as above has been carried out over the period of the S3 run, using the same initial heterodyne parameters and pulsar injection parameters. The extracted

pdfs can be seen in figure 2.5 and show that without the timing noise correction the signal is completely missed. The fact that the signal is not seen at all if the timing noise

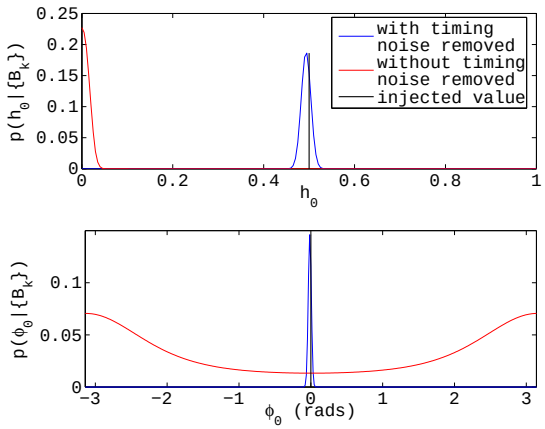

Figure 2.5: The extracted pdfs for h_0 and ϕ_0 for a simulated signal from the Crab pulsar over the period of S3 with and without timing noise removed.

heterodyne is not used might seem at odds with the 2.6 year decoherence time stated above, as S3 was only about 8 months after S2. It is not seen however, because the initial heterodyne values used were chosen to be those from the Crab ephemeris closest to the start of S2 and not those from a more general fit to the data over an extended period, as was used to calculate $T_{\mathrm{decoherence}}$. If we perform a fit to the Crab pulsar ephemeris over the whole of 2003, when the S2 and S3 took place, we can again check what difference removing or not removing the timing noise has for S3 (see figure 2.6).

Now it can be seen that for an extended fit for the Crab parameters whether or not

Table 2.4: The parameters of the Crab for a fit to second order in frequency over the period of 2003 using monthly ephemeris data.

PSR J0534+2200	
ν	29.81027139567395 Hz
$\dot{\nu}$	$-3.736984315709851 \times 10^{-10}$ Hz/s
$\ddot{\nu}$	$1.070857000427481 \times 10^{-20}$ Hz/s^2
Frequency epoch	GPS 726624013.0597030

the timing noise is removed makes little difference over S3, although a slight phase offset is present. One might then ask if it is then necessary to perform the extra timing noise heterodyne if fits to the pulsar parameters over periods of say a year are

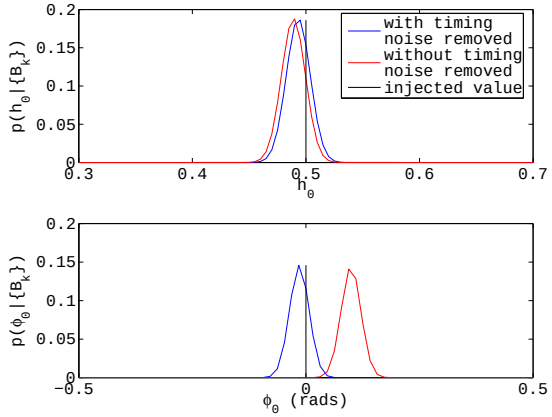

Figure 2.6: The extracted pdfs for h_0 and ϕ_0 for a simulated signal from the Crab pulsar over the period of S3 with and without timing noise removed for initial heterodyne values obtained from a fit to the ephemeris over 2003 (see table 2.4).

good enough to provide the initial heterodyne parameters. This is when the value of $T_{\mathrm{decoherence}}$ does come into play. For times scales less than this a single heterodyne with properly fit parameters might be sufficient, although for long observation times, as are required for continuous wave sources to build up S/N, it is best to track the phase as accurately as possible. This also allows the maximum information to be extracted if a detection occurs, as the electromagnetic and gravitational wave phases can be compared accurately. Glitches in the pulsar could also throw out the accuracy of any general fit, that a continuous updating of parameters, as is done with the timing noise heterodyne stage, would not be sensitive to.

2.3.2 Timing noise in other pulsars

For the majority of pulsars timing noise is most prominent in the second derivative of frequency, but for millisecond pulsars this value is often so small as to be unmeasurable. For these pulsars an estimate of the effect of timing noise in terms of the Δ_8 parameter can be made. This value can be used to estimate the cumulative phase contribution of timing noise. As values of $\ddot{\nu}$ are so often unavailable values of Δ_8 can be estimated via equation 2.29. In Chapter 3 this test will be used to examine the validity of the timing solutions for the selection of pulsar in our analysis.

2.4 Pulsars in binary systems

Of the 1533 pulsars in the ATNF catalogue some 112 are in binary systems. The first of which, PSR J1915+1606, was discovered by Hulse and Taylor in 1974 [16]. Of these 112 pulsars 88 of them have spin frequencies greater than 25 Hz (out of a total 150 isolated and binary pulsars). The majority of millisecond pulsars are in binary systems. This disproportionally large number of fast spinning pulsars in binary systems is unsurprising, as their rotation speed can be attributed to the very fact that they have a companion. In such systems accretion of material from a companion onto the pulsar results in it being spun-up as angular momentum is conserved. This process is seen in LMXBs, where material accreting onto the neutron star is intensely heated and emits X-rays. The Eddington limit suggests that there must be a limit on the rate of accretion where it matches the rate at which the star can lose energy. Assuming the energy is lost through magnetic dipole radiation a limit on the pulsar period from accretion spin-up can be given by

$$P = 1.9 B_9^{6/7} \text{milliseconds}, \tag{2.33}$$

where B_9 is the magnetic field strength on the stars surface in units of 10^9 gauss [75]. It its shown in figure 10.1 of Lyne and Graham-Smith (1998) [75] that the majority of millisecond pulsars fall below this limit. Of course this is assuming accretion energy is only lost via dipole radiation and discounting the possibility of energy loss via gravitational wave emission. A limit on the spin period of recycled[3] millisecond pulsars supposing gravitational wave emission plays a role in energy loss is given in Andersson (1999) [55]. The mechanism for producing this limit will only be in play during the accreting stage when the neutron star is hot. It is believed that all millisecond pulsars are recycled and belonged to binary systems for which, in the case of now isolated pulsars, a subsequent disruption, i.e. a supernova explosion or merger, caused the loss/expulsion of the companion star. Millisecond pulsars have a magnetic field several

[3] pulsars spun-up by accretion.

orders of magnitude lower than the slower population meaning that their spin-down rate (due to magnetic dipole radiation) is significantly lower and they will continue to spin at high speeds over a long period.

2.4.1 Pulsar timing

A brief discussion on how pulsar timing information is obtained is relevant here. The majority of pulsars have been discovered and are monitored using radio telescopes. Searches, discussed in more detail in Lyne and Graham-Smith (1998) [75], in general use Fourier transform methods to look for periodic signals in the radio telescope output. Radio astronomers also take into account, and fit, the effect of interstellar dispersion across the radio frequency band which they observe, whereby electrons in the interstellar medium slow down electromagnetic waves as a function of frequency. This dispersion measure will depend on the density of the ISM through which the radio waves have had to travel. Once a pulsar signal is detected timing measurements can be made. Over short periods of time the time series radio data can be folded at the pulsar frequency to build up the S/N of the actual pulse. Once a stable pulse is obtained[4] the time of arrival (TOA) can be measured at the peak of the pulse. These pulse times can then be used to extract more precise information about the pulsar parameters, including its position and frequency parameters.

The most prevalent tool used by pulsar astronomers for fitting timing measurements is the TEMPO software [2]. This requires precise solar system ephemerides, containing the positions and velocities of the major solar system bodies, to convert TOAs at a detector to the rest frame of the pulsar. It computes the pulsar phase at each TOA, $\phi(T_i)$, over the range of pulsar parameters (α, δ, ν, $\dot{\nu}$, etc), and uses a χ^2 goodness of fit statistic to determine the best model via minimisation. A starting point for the fit is obtained through a rough knowledge of the position and frequency from the initial discovery, but it can still be quite complex as there can be many other parameters that could be contributing. Below it is seen how a pulsar in a binary system requires

[4]individual pulses can vary in shape, but the summation of many gives a generally stable pulse shape.

a complex model with many more parameters than an isolated object.

2.4.2 Binary pulsar timing

The fact that the majority of pulsars within our gravitational wave frequency band are in binary systems means that in any search for known pulsars, if we want to maximise the number of potential sources, then we need to look into how this will effect the search described above. This has not been used or described before in previous pulsar gravitational wave searches. Equation 2.5 shows the timing corrections needed to take account of Doppler and relativistic delays to a signal and transform it to the SSB. As is generally the case any additional Doppler delays from the pulsar's actual motion relative to the SSB are negligible and the SSB frame can be considered as the rest frame of the pulsar. For a pulsar in a binary system this will not be the case and its motion within the system will need to be taken into account. To achieve this a transform from binary system barycentre to the pulsar proper time is needed.

The basic transformation and binary models below are summarised in Taylor and Weisberg (1989) [17] and used in the pulsar timing program Tempo [2]. The transformation from SSB time t_b (in TT) to pulsar proper time T follows the form of equation 2.5 and is

$$t_b - t_0 = T + \Delta_{\rm R} + \Delta_{\rm E} + \Delta_{\rm S} + \Delta_{\rm A}, \tag{2.34}$$

where $\Delta_{\rm R}$ is the Roemer time delay giving the propagation time across the binary orbit; $\Delta_{\rm E}$ is the Einstein delay and gives gravitational redshift and time dilation corrections; $\Delta_{\rm S}$ is the Shapiro delay and gives general relativistic correction; and $\Delta_{\rm A}$ is the aberration delay caused by the pulsars rotation. When radio astronomers search for pulsars in binary systems they need to have a model of that system to calculate the transformation to proper time. For the majority of systems the orbits can be described as Keplerian (just governed by Newtonian gravity and following Kepler's laws). Such Keplerian orbits are defined by five parameters, T_0 - the time of periastron (closest approach in the binary orbit); ω - the longitude of periastron; P_b - the orbital period; e - the orbital eccentricity (where $e = \sqrt{(1 - b^2/a^2)}$ and a and b are the semi-major and

semi-minor axis of the orbital ellipse respectively); and $x \equiv (a \sin i)/c$ is the projected semi-major axis, with i being the orbital inclination. We will look at the three main models used by radio pulsar astronomers to describe binary systems.

Blandford-Teukolsky model

The first model put forward for use in describing pulsars in binary systems was that of Blandford and Teukolsky [77] (BT), which provided a model that made no assumptions about the correct relativistic theory of gravity. This model assumes a Keplerian orbit with slow precession, into which additional relativistic effects have been added. Other phenomena can be taken into account through time derivatives of the four main orbital elements excluding T_0. As shown in [17] equation 2.34 becomes

$$\begin{aligned} t_b - t_0 = T + \{x \sin\omega(\cos E - e) + [x \cos\omega(1-e^2)^{1/2} + \gamma] \sin E\} \\ \times\Big\{1 - \frac{2\pi}{P_b}[x\cos\omega(1-e^2)^{1/2}\cos E - x\sin\omega\sin E] \\ \times(1 - e\cos E)^{-1}\Big\}, \end{aligned} \tag{2.35}$$

where γ incorporates gravitational redshift and time dilation effects, and E is the eccentric anomaly as defined via Kepler's equation,

$$E - e\sin E = \frac{2\pi}{P_b}(t_b - T_0). \tag{2.36}$$

The eccentric anomaly can be well approximated by power series in e as in Dhurandhar and Vecchio (2001) [78], but in practice it is often easier to solve iteratively. Any additional relativistic effect can be fit via the inclusion of $\dot{\omega}$, $\dot{P}_b$, $\dot{x}$ and $\dot{e}$, so for example $\omega = \omega_0 + \dot{\omega}(t_b - T_0)$. The BT model has been used to fit data for 47 of the binary pulsars with $\nu > 25\,\mathrm{Hz}$, so is the most common model used. One of these systems is modelled using the Tempo model BT2P which accommodates three orbits, the first of which can be relativistic, but the second and third are Keplerian. The system is a multiple system, described in Wolszczan *et al.* (2000) [79], in which three, or possibly four, planets orbit the pulsar. Although additional orbits complicate the above equations it

has been suggested to us by Michael Kramer [80] that the ordinary BT model is good enough to describe the system for our purposes.

Low eccentricity model

The second most common model used in fitting radio observations of binaries is the low eccentricity model (called ELL1 in TEMPO) developed in Lange *et al.* (2001) [81]. It is used as a fit for pulsars in very low eccentricity orbits where e is almost zero and is the model for 34 of the pulsars with $\nu > 25\,\mathrm{Hz}$. With an almost circular orbit it is very hard to fit a value of T_0 and ω, so these parameters, along with e, are replaced with the time of the ascending node of the orbit ($T_{\mathrm{asc}} \equiv T_0 - \omega P_b/2\pi$) and the first and second Laplace-Lagrange parameters $\eta \equiv e\sin\omega$ and $\kappa \equiv e\cos\omega$. The time delays for this model, defined in [81] and the TEMPO code, are

$$\Delta_{\mathrm{R}} + \Delta_{\mathrm{E}} = \quad \Delta_{\mathrm{RE}} = \quad x\left(\sin\Phi + \frac{\kappa}{2}\sin 2\Phi - \frac{\eta}{2}\cos 2\Phi\right), \tag{2.37}$$

$$\Delta_{\mathrm{RE}}{}' = \quad x\cos\Phi, \tag{2.38}$$

$$\Delta_{\mathrm{RE}}{}'' = \quad -x\sin\Phi, \tag{2.39}$$

$$\Delta_{\mathrm{S}} = \quad -2r\ln(1 - s\sin\Phi), \tag{2.40}$$

$$\Delta_{\mathrm{A}} = \quad A_0\sin\Phi + B_0\cos\Phi, \tag{2.41}$$

where the phase of the orbit is $\Phi = \frac{2\pi}{P_b}(t_b - T_{\mathrm{asc}})$, $r = Gm_2/c^3$ is the Shapiro range parameter for a companion mass m_2, $s = \sin i$ is the Shapiro shape parameter, and A_0 and B_0 are abberation coefficients. Time derivatives for the parameters are taken into account with the reference epoch now being T_{asc}. The time delay thus becomes

$$t_b - t_0 = T + \Delta_{\mathrm{RE}}\left(1 - \frac{2\pi}{P_b}\Delta_{\mathrm{RE}}{}' + \frac{4\pi^2}{P_b^2}\Delta_{\mathrm{RE}}{}'^2 + \frac{2\pi^2}{P_b^2}\Delta_{\mathrm{RE}}\Delta_{\mathrm{RE}}{}''\right) + \Delta_{\mathrm{S}} + \Delta_{\mathrm{A}}. \tag{2.42}$$

The inclusion of the Sharpiro shape and range parameters means that, under strong-field gravity conditions, this model can provide more information about the nature of the system than the BT model. These parameters are nearly degenerate and can show

up as a small correction to the observed ellipticity. For the majority of systems the effect of the $\Delta_{\rm S}$ term is negligible. The abberation delay coefficients will also be small and are also degenerate with other values, so the $\Delta_{\rm A}$ term will contribute very little. In TEMPO the abberation coefficients are not included in the model fitting procedure although they can be set to a fixed value if desired.

Damour-Deruelle model

The third most common model is the Damour-Deruelle (DD) model [82]. This model uses a method for solving the relativistic two-body problem to post-Newtonian order and is valid under very general assumptions about the nature of gravity in strong field regimes. It is useful for highly relativistic systems where the most information needs to be extracted from the timing solution. There are six pulsars with $\nu > 25\,\mathrm{Hz}$ in the ATNF catalogue using this model. This model is again summarised in [17] with the various time delays given by

$$\begin{aligned}
\Delta_{\rm R} &= x \sin\omega[\cos E - e(1+\delta_r)] \\
&\quad + x[1 - e^2(1+\delta_\theta)^2]^{1/2} \cos\omega \sin E, && (2.43)\\
\Delta_{\rm E} &= \gamma \sin E, && (2.44)\\
\Delta_{\rm S} &= -2r \log\{1 - e\cos E - s[\sin\omega(\cos E - e) \\
&\quad + (1-e^2)^{1/2} \cos E \sin E]\}, && (2.45)\\
\Delta_{\rm A} &= A_0\{\sin[\omega + A_e(E)] + e\sin\omega\} \\
&\quad + B_0\{\cos[\omega + A_e(E)] + e\cos\omega\}, && (2.46)
\end{aligned}$$

where the eccentric anomaly is now defined via Kepler's equation as

$$E - e\sin E = 2\pi\left[\left(\frac{T-T_0}{P_b}\right) - \frac{\dot{P}_b}{2}\left(\frac{T-T_0}{P_b}\right)^2\right], \qquad (2.47)$$

and the true anomaly $A_e(E)$ is given by

$$A_e(E) = 2\arctan\left[\left(\frac{1+e}{1-e}\right)^{1/2}\tan\frac{E}{2}\right]. \tag{2.48}$$

The time derivative of ω now comes into the equation via $\omega = \omega_0 + kA_e(E)$, where $k = \dot{\omega}P_b/2\pi$, but the other time derivatives and γ are essentially the same as for the BT model. The abberation coefficients and parameters δ_r and δ_θ are again small and nearly degenerate with other parameters, making the $\Delta_{\rm A}$ term negligible.

2.4.3 Comparison with TEMPO

The above three models are all implemented in the pulsar timing software package TEMPO. In our search for gravitational waves from binary systems we also require these additional time corrections to correctly calculate the phase of the pulsar for heterodyning. Code to calculate the binary time delays for each model have been adapted from their TEMPO counterparts and are available under CVS in the LALapps repository [83]. Some consistency tests have been performed between the two codes, which are described below.

PSR J1012+5307

A convincing check of the LALapps code is to use it to demodulate a signal from a radio pulsar. To do this Michael Kramer supplied us with a set of TOAs for PSR J1012+5307 obtained with the Effelsberg 100 m radio telescope in Bonn, Germany. This pulsar has the second most circular orbit known and hence requires the ELL1 model. The data spanned just over 5 years[5] of on and off observations of the pulsar, and was supplied in the form of TOAs in MJD[6] with timing errors in μs and the observing frequency. We were also supplied with the TEMPO fit to the pulsar parameters (see table 2.5).

There were several correction that needed to be made to the supplied TOAs to convert them from the time system measured at the radio telescope to GPS. The

[5] from 2nd January 2000 to 12th February 2005
[6] Modified Julian Date = Julian Date - 2400000.5

Table 2.5: The parameters of PSR J1012+5307. Values are quoted with 1σ errors in brackets.

PSR J1012+5307	
α	$10^{\rm h}12^{\rm m}33^{\rm s}.43368(1)$
δ	$53°07'02''.5880(2)$
PMRA	$2.38(3)$ mas/yr
PMDEC	$-25.35(5)$ mas/yr
ν	$190.267837621884(9)$ Hz
$\dot{\nu}$	$-6.2022(2)\times10^{-16}$ Hz/s
$\ddot{\nu}$	$2.0(3)\times10^{-27}$ Hz/s^2
Frequency epoch	MJD 50700
Dispersion measure	$9.0233(7)$ cm^{-3} pc
Observing Frequency	1408.6 MHz
Binary model	ELL1
x	$0.581817(1)$ s
P_b	$0.6046727136(2)$ days
$T_{\rm asc}$	MJD 50700.0816289(4)
η	$7(4)\times10^{-7}$
κ	$-1(40)\times10^{-8}$

first correction to the raw TOAs was to correct for the difference between the stable Hydrogen maser time source at the telescope and coordinate Universal Time of the National Institute of Science and Technology UTC(NIST) reference, supplied by Michael Kramer. This correction was typically of order a few μs. The next correction that could have been made was the conversion from UTC(NIST) to UTC although this has been less than ±100 ns since 6$^{\rm th}$ July, 1994[7] so in practice was left out. The conversion between time in UTC times (given in MJD) to GPS times then follows as $t_{\rm GPS} = (t_{\rm UTC(MJD)} - 44244\,{\rm days}) \times 86400\,{\rm s} + {\rm leapseconds}$, where the 44244 days is the MJD of the GPS time epoch (1$^{\rm st}$ January, 1980) and the leap seconds represent the difference between UTC and GPS required as UTC is adjusted to match the Earth's rotation. For the times span of our given TOAs the number of leap seconds was always 13.

The next step was to correct the times for interstellar dispersion. The dispersion

[7] http://tf.nist.gov/timefreq/pubs/bulletin/nistutc2000.htm

time delay is given by

$$\Delta t_{\rm disp} = 4.148808 \times 10^3\,{\rm MHz}^2\,{\rm pc}^{-1}\,{\rm cm}^3\,{\rm s} \times {\rm DM}/f^2\,{\rm s}, \tag{2.49}$$

where DM is the dispersion measure in $\mathrm{cm}^{-3}\,\mathrm{pc}$ and f is the radio observation frequency in MHz (see table 2.5 for values). This correction is subtracted from the TOAs to give observations at infinite frequency with no dispersion.

The next stage compared the publicly available LIGO Algorithm Library (LAL) [84] barycentring codes to Tempo. As the pulsar parameters were calculated using Tempo we can check whether our barycentring codes can use these values to match the pulsar's phase. One of the major differences between our binary time domain code and the Tempo code is the time system used. All epochs in Tempo are defined in Barycentric Dynamical Time (TDB) whereas the general reference time for gravitational wave data analysis in the LSC is GPS time. Epochs can be converted to Barycentric Dynamical Time (TDB), which is a generally used timescale for ephemerides referenced to the solar solar barycentre. This timescale is related to Terrestrial Time (TT - formerly Terrestrial Dynamical Time TDT), which represents a time consistent with relativity for an observer on the Earth's surface, by a small factor, TDB = TT + δt, no greater than a couple of milliseconds and given by

$$\delta t = 0.001\,658\,{\rm s} \times \sin\Phi + 0.000\,014\,{\rm s} \times \sin 2\Phi, \tag{2.50}$$

where $\Phi = 357.53^\circ + 0.985\,600\,28^\circ({\rm MJD} - 51\,544.5)$ is the mean anomaly, or phase, of the Earth's orbit at the given Modified Julian Date. TT is related to International Atomic Time (TAI) via TT = TAI + 32.184 seconds[8] The conversion from TT to GPS time, therefore meant subtracting 51.184 s, where 32.184 s comes from the difference between TT and TAI and the remaining 19 s are the number of leap seconds between TAI and GPS. The code to calculate the SSB time delay takes in the pulsar's position,

[8]There are many definitions of time used in astronomy and very careful attention of which one is being used and how to convert between them is essential when high precision timings are being made. A good guide to these is given at [85].

the telescope position and a solar system ephemeris[9] and was used for each pulsar TOA to correct to the time at the SSB. This code was written by Curt Culter and has been independently tested against TEMPO [33, 66] showing no more than 4 μs difference between the two. Once corrected to the SSB the TOAs then needed to be corrected to the pulsar proper time by calculating the time delays in the binary system using the binary system parameters (see table 2.5). The binary and solar system time delays for a selection of TOAs covering part of the binary orbit are shown in figure 2.7. Once the corrections to the TOA had been applied the phase could be checked. All

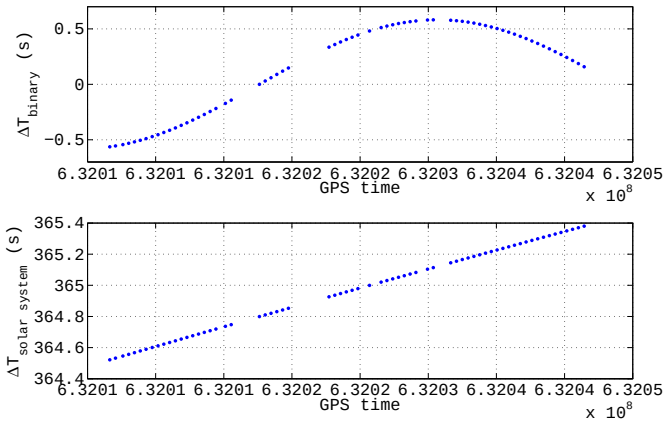

Figure 2.7: The binary and solar system time delays calculated for PSR J1012+5307 over a part of an orbit.

TOAs should be in phase as they each represent the peak of a pulse. If the TOAs were incorrectly converted by the barycentring codes then this would show up by them being out of phase. The phase at each TOA was calculated using the supplied frequency and frequency derivatives in equation 2.1, with $\phi_0 = 0$ and the frequency epoch as t_0. Figure 2.8 shows how the TOAs barycentred using our code stay in phase well over the observation time. There is a slight slope of ~ 0.04 rads/yr in the phase. A yearly periodicity is also present possibly showing up the slight difference in the LAL solar system barycentring code and TEMPO, although these effects are at a very low level. There are several points that are quite out of phase which correspond to times when the level of noise on the TOA measurements was high.

[9] the ephemerides used are those published by the Jet Propulsion Laboratory [86].

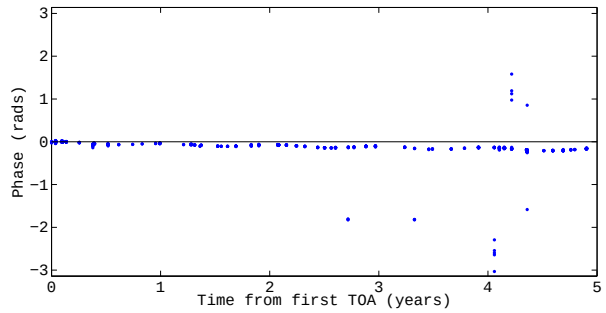

Figure 2.8: The modulus of the pulsar phase at each TOA over a 5 year period.

The parameters for PSR J1012+5307 were generated using the ELL1 model, so the above test really only checked the code describing that model. We can also check the two other models by converting $T_{\rm asc}$ to T_0 and the Laplace-Lagrange parameters κ and η to $e = \sqrt{(\kappa^2 + \eta^2)}$ and ω. As this pulsar has such a low eccentricity then T_0 can be set equal to $T_{\rm asc}$ and ω set to zero. Doing this we can again produce the phase plots for the BT and DD models (figure 2.9). The phase is again well described for these

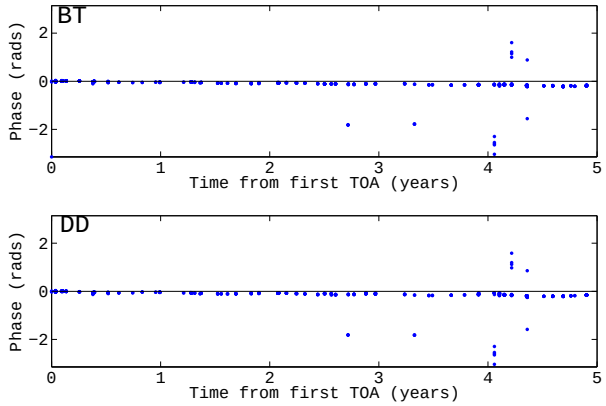

Figure 2.9: The modulus of the pulsar phase at each TOA over a 5 year period for the BT and DD models.

two models, with the slope and periodicity still present. This suggests that the slope and periodicities are not caused by the binary timing correction code (as each model is independent), but may be a results of slight errors in the other timing corrections, the solar system barycentring code or the parameters used.

Direct check against TEMPO

As was done for the solar system barycentring code, the binary timing code can be tested directly against TEMPO. TEMPO can be set into the so called predictive mode, whereby it uses a set of pulsar parameters to predict the pulsar phase over a period of time. This predicted phase can be then be compared with that calculated using our binary timing code. This was done for each model with a set of 500 randomly generated binary pulsar systems over a period of 100 days. The detector location was set to be at the SSB, so the solar system time delay errors would not be included. Histograms of the time residuals between the codes are shown in figure 2.10 for each model. These show that the time difference between the two codes is generally less

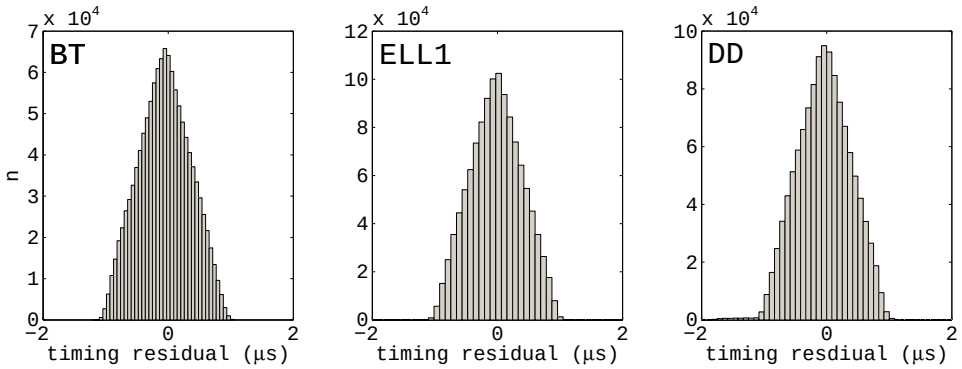

Figure 2.10: Timing residuals between the pulsar phase as predicted by TEMPO and that computed with our binary code for 500 random pulsars for each binary model.

than $\pm 1\,\mu$s, meaning there is a very good agreement between the codes and sufficient accuracy to ensure any signal and template remain in phase.

Blackadder: ...the fact that this secret has eluded the most intelligent people since the dawn of time doesn't dampen your spirits?

Percy: Oh, no. I like a challenge

Blackadder

Chapter 3

Results of the search for continuous gravitational waves from known pulsars

In this chapter we give results of the search for continuous gravitational waves from a selection of known pulsars using LIGO and GEO 600 data. We also show the extraction of several hardware signal injections and their interpretation. We discuss the selection of the pulsars used in the search, with regard to the validity of the pulsar parameters and possible timing noise effects. Briefly discussed is the possiblity of marginalising over calibration and distance errors in any results. Results for these pulsars are then given in terms of upper limits on the gravitational wave amplitude and ellipticity, and the astrophysical implications discussed. The code used to produce these results can be found at [83] under CVS with tag `S3KnownPulsarSearch_220605`.

3.1 The science runs

This chapter will focus on the results of the known pulsar search in data from the third and fourth LIGO and GEO 600 science runs (S3 and S4). These runs were carried out

from 31st October, 2003 to 9th January, 2004 and 22nd February to 23rd March, 2005 respectively. The search technique described in the previous chapter has been applied to this data to produce upper limits on the gravitational wave amplitude and equatorial ellipticity for a selection of known radio pulsars. The work is a natural extension of the work of Réjean Dupuis [66] and published in Abbott *et al.* (2004a and 2005a) [33, 34].

3.1.1 Detector calibration

Most scientific instruments need calibrating in some way to obtain accurate information about their measurements, and gravitational wave detectors are no different. They need to be calibrated to obtain their true response in terms of gravitational wave strain and phase over their frequency range, where strain, $s(t) = (L_x(t) - L_y(t))/L_0$, is the differential arm length of the interferometer over the arm length. Below we describe the calibration procedure for data from the LIGO interferometers. GEO 600 data is supplied in a pre-calibrated format, with the calibration procedure described in Hewitson *et al.* (2003) [87][1]. The raw output of the detector is the error signal $e(t)$, which needs to be converted into strain. To do this $e(t)$ is multiplied by a response function $R(f)$ so, in the frequency domain,

$$\tilde{s}(f) = R(f)\tilde{e}(f), \tag{3.1}$$

where $\tilde{s}(f)$ and $\tilde{e}(f)$ are the Fourier transforms of $s(t)$ and $e(t)$. The derivation of this response function, via the control loop which keeps the mirror motions small and the interferometer in lock, is given in the LIGO Calibration Documentation [88]. The variations in this function with time are tracked using calibration lines with known amplitudes injected into the control loop at certain frequencies. The response function as a function of frequency and time is then given by

$$R(f,t) = \frac{1 + \alpha(t)\beta(t)H_0(f)}{\alpha(t)C_0(f)}, \tag{3.2}$$

[1] such a procedure is now being performed for LIGO data.

where the $C_0(f)$ and $H_0(f)$ are the sensing function and open loop gain respectively at a reference time t_0, and the $\alpha(t)$ and $\beta(t)$ coefficients track the changes in these using the calibration lines. The functions H_0 and C_0 are complex and have a phase response as well as amplitude: $H_0 = |H_0|e^{i\theta_H}$, $C_0 = |C_0|e^{i\theta_C}$.

In terms of our analysis the B_ks discussed in Chapter 2 will initially be uncalibrated. They are calibrated to give a strain via.

$$\begin{aligned} \Re\{B_{k\ \text{calibrated}}\} &= \Re\{B_k\}\Re\{R(f,t)\} - \Im\{B_k\}\Im\{R(f,t)\}, \\ \Im\{B_{k\ \text{calibrated}}\} &= \Re\{B_k\}\Im\{R(f,t)\} + \Im\{B_k\}\Re\{R(f,t)\}. \end{aligned} \tag{3.3}$$

3.2 Hardware injections

For analysis validation purposes simulated gravitational wave signals for a variety of sources (bursts, pulsars, inspirals and stochastic) have been injected into the LIGO interferometers during the science runs from S2 onwards. In S2 two pulsar signals were injected [34]. This was increased to 10 initial signals for S3 and S4 covering a wider range of signal parameters. Extracting and understanding these injections has been quite an arduous task, but has been invaluable in validating the analysis.

The hardware injection signals are produced using software (under LALapps [83]), which is partially independent of the extraction code. Similarities between the code include the use of the same barycentring routines and the same detector antenna response function routines. The injection code defines the signal amplitude and orientation as the two parameters $A_+ = \frac{1}{2}h_0(1+\cos\iota)$ and $A_\times = h_0\cos\iota$ which are independent, rather than h_0 and $\cos\iota$ which are partially degenerate. The signals were added into the LIGO detectors via the excitation signal of the test mass in one arm.

3.2.1 S3 injections

An initial analysis of the S3 pulsar injections is given in [66]. The data have since been re-analysed with more recent versions of the calibration functions, the results of which

are presented here. For S3 initially 10 pulsars signals were injected, with a further one added at the end of the run to be in coincidence with a single injection into GEO 600. The majority of injection parameters were decided upon randomly, although pulsar frequencies needed to avoid major instrumental or calibration lines, and amplitudes were dependent on the frequency. The injections were split into two groups of five, where values of h_0 were calculated to give 2 each with S/Ns of approximately 3, 9, 27, 81 and 243. The parameter values are shown in table 3.1. The 10 initial signals were

Table 3.1: The parameter values for the S3 pulsar hardware injections. All angular parameters are given in radians.

PULSAR	α	δ	$\nu_{\rm gw}$ (Hz)	$\dot{\nu}_{\rm gw}$ (Hz/s)	h_0	ϕ_0	ι	ψ
0	1.25	-0.98	265.5	-4.15×10^{-12}	9.38×10^{-25}	2.66	0.65	0.77
1	0.65	-0.51	849.1	-3.00×10^{-10}	8.49×10^{-24}	1.28	1.09	0.36
2	3.76	0.06	575.2	-1.37×10^{-13}	1.56×10^{-23}	4.03	2.76	-0.22
3	3.11	-0.58	108.9	-1.46×10^{-17}	6.16×10^{-23}	5.53	1.65	0.44
4	4.89	-0.21	1430.2	-2.54×10^{-8}	1.01×10^{-21}	4.83	1.29	-0.65
5	5.28	-1.46	52.8	-4.03×10^{-18}	1.83×10^{-23}	2.23	1.09	-0.36
6	6.26	-1.14	148.7	-6.73×10^{-9}	5.24×10^{-24}	0.97	1.73	0.47
7	3.90	-0.36	1221.0	-1.12×10^{-9}	2.81×10^{-23}	5.24	0.71	0.51
8	6.13	-0.58	194.3	-8.65×10^{-9}	6.02×10^{-23}	5.89	1.50	0.17
9	3.47	1.32	763.8	-1.45×10^{-17}	1.61×10^{-22}	1.01	2.23	-0.01
GEO	0.78	-0.62	1125.6	-2.87×10^{-11}	7.5×10^{-22}	1.99	0.84	0.37

injected into the LIGO detectors for approximately the first half of the run, then all were turned off for a couple of weeks, to ensure data was present that was not artificially contaminated, and then turned back on with the two loudest signals removed. The simultaneous injection with GEO 600 was switched on near the end of the run.

These signals were extracted from the detector data using the analysis techniques described in Chapter 2. The two most important parameters for checking that the calibration of the instruments was correct were the amplitude and initial phase, so in the Bayesian fitting procedure the ι and ψ parameters were held fixed at their known values. This was done because the correlations between h_0 and $\cos\iota$ and ϕ_0 and ψ, respectively could lead to the marginalised posterior probability distributions for each parameter being distorted or spread out [66]. Figure 3.1 shows the posteriors for the initial 10 injected signal.

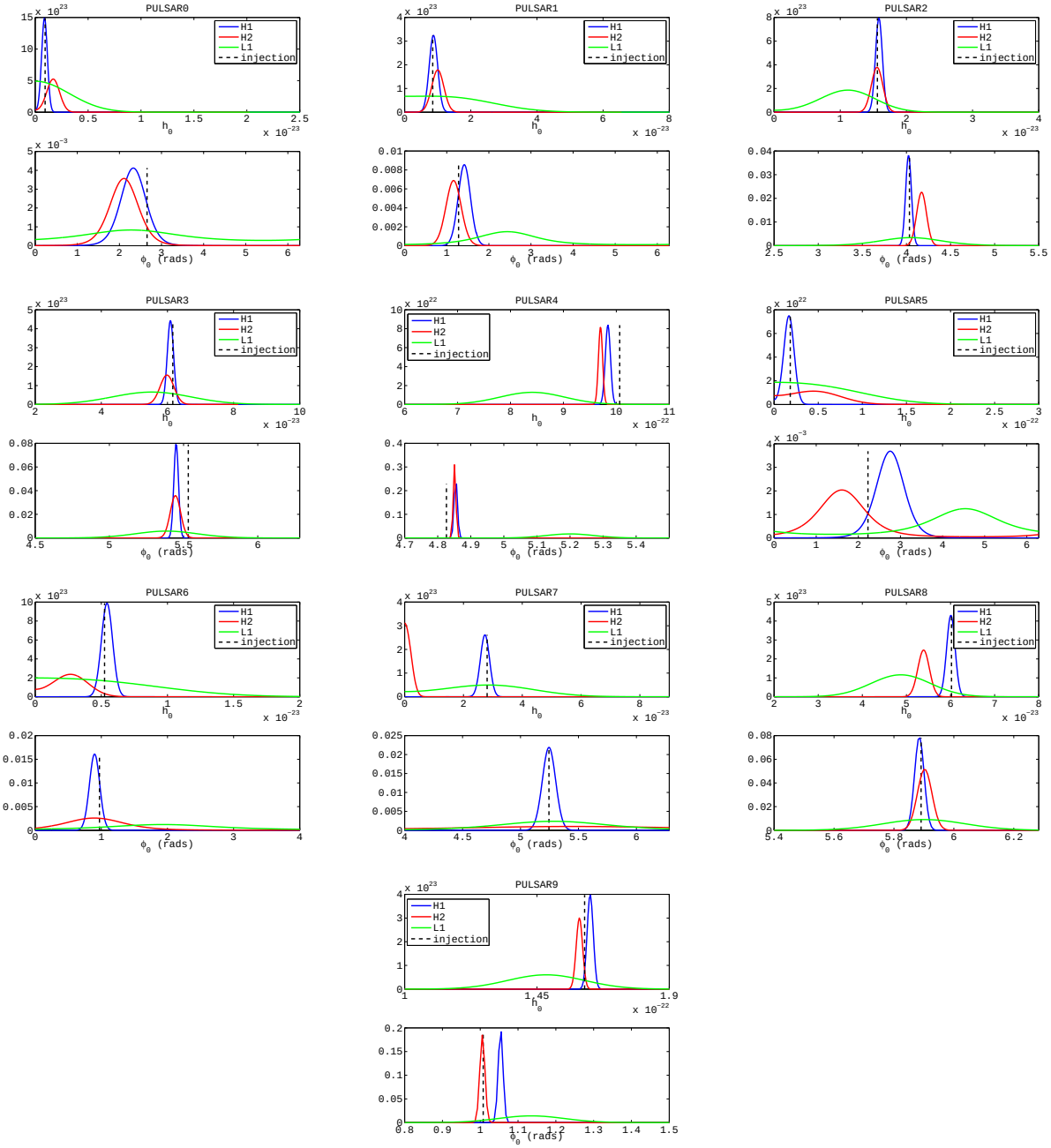

Figure 3.1: The pdfs of h_0 and ϕ_0 for 10 injections into the LIGO detectors during S3.

The pdfs in figure 3.1 are not quite the true posteriors that were extracted, but have been corrected for some calibration differences and injection errors. The h_0 pdfs have been multiplied by a factor related to the difference in the detector actuation function amplitudes between those used to calculate the injection amplitudes and those used to calculate the final calibration response function. The ratio of these actuation amplitudes is shown in figure 3.2. For the H1 and H2 interferometers the amplitudes are

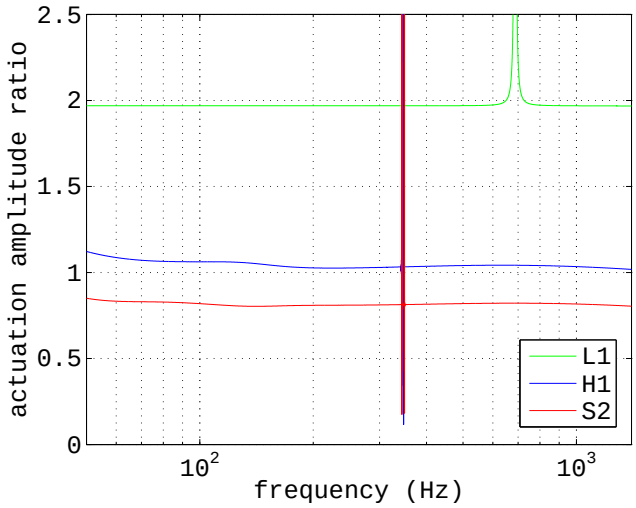

Figure 3.2: The ratio of the actuation function amplitudes for the LIGO interferometers between that measured for the S3 calibration and that measured prior to S3 during the E10 engineering run.

similar with ratios of approximately 1.0 and 0.8 respectively. For the L1 interferometer there is almost a factor of two difference. In reality these factors might not quite reflect the true error between the injection amplitudes and those extracted, as the extracted values actually use the full response function to calibrate the amplitude, but they do provide an estimate. The variations from the true injected amplitude, after the above corrections, could also be due to systematic uncertainties in the calibration (a method of marginalising over these is discussed in §3.4.1), as it can be seen for the stronger injections that the peak value of h_0 for H1 is systematically higher than H2. For L1 there seem to be large uncertainties which cause the pdfs to wander about the true value. The two other main anomalies are in the amplitudes of Pulsar7 and Pulsar0 in H2. Pulsar7 appears to be missing from H2, which has been tracked down to the fact that its amplitude was accidentally set at 1/60 of the supposed injection value.

PULSAR0 appears slightly larger in H1 than H2 (at odds with the general systematic showing the opposite), which is due to it being injected with an amplitude ~ 1.6 larger than expected.

The phases have also been corrected due to an error included during their injection. For the injections the true values of ϕ_0 need to be corrected for the actuation phase $\phi_{\rm act}$. This additional phase was added with the wrong sign leading to the extracted phase being $\sim 2\phi_{\rm act}$ away from the true value of ϕ_0. Again there was slight difference between the actuation phase used for the injection and that used for the calibration it was extracted with, so the true correction required the subtraction of both actuation phases (although they were very similar).

After the introduction of these corrections it can be seen that the phases agree with each other to within a few degrees. This provides some evidence that there is phase coherence between the detectors and that a joint analysis, combining the data from the detectors, would be possible. Unfortunately, as the corrections to the phase and amplitudes were included after the fitting procedure, the joint analysis could not be used on the injections as in [34].

The GEO 600 injection has been analysed in [66]. It was injected into the instrument in a different way to the LIGO injections as described in Weiland *et al.* (2004) [89]. As described in [66] the phase and amplitude of this signal in GEO 600 were significantly off their true values due to pickup between the injection hardware and the interferometer gravitational wave channel.

3.2.2 S4 injections

For S4 the 10 initial injections used in S3 were again used to create artificial signals in the LIGO interferometers. Their amplitudes were adjusted to give approximately the same S/N as for S3, but taking into account the better sensitivity during this run. For all but PULSAR9 the h_0 values were reduced by a half, with PULSAR9 being so strong that its amplitude was reduced by a factor of 20. The phases for all the injections are also shifted by π radians with respect to those given in table 3.1. These

signals were injected for the second half of the run from 8$^{\text{th}}$ March 2005 onwards. The updated h_0 values are shown in table 3.2. There were also an additional two signals, simulated to be from pulsars in binary systems, injected for the last day of the run. The binary pulsar injections allowed the testing of the binary timing code described in Chapter 2 as the injection code and extraction code were written independently. The binary injection signal (PULSAR10 and 11) parameters were taken from PULSAR3 and 8 respectively, with the frequencies changed and amplitudes increased to make sure they were visible over the short injection time. The frequency, amplitude and binary system parameters are shown in table 3.3. The binary system parameters were chosen to have one in a relatively eccentric orbit and one in a circular orbit with fairly short periods, so that they would have completed or nearly completed at least one full orbit during the injection. The T_0 values are given in the pulsar rest frame[2].

Table 3.2: The parameter values for the S4 pulsar hardware injections.

PULSAR	0	1	2	3	4
h_0	4.69×10^{-25}	4.25×10^{-24}	7.81×10^{-24}	3.08×10^{-23}	5.03×10^{-22}
PULSAR	5	6	7	8	9
h_0	9.17×10^{-24}	2.62×10^{-24}	1.40×10^{-23}	3.01×10^{-23}	8.06×10^{-24}

Table 3.3: The parameter values for the S4 binary pulsar hardware injections.

PULSAR	ν_{gw} (Hz)	h_0	T_0 (MJD in GPS)	P_b (days)
10	250.6	1.23×10^{-22}	51749.71156482407	1.35405939
11	188.0	4.93×10^{-22}	52812.92041175901	0.31963390
	e	ω_0 (degs)	$a \sin i$ (secs)	
10	0.0	0.0	1.65284	
11	0.180567	322.571	2.7564	

These signals were again extracted using the analysis techniques from Chapter 2. For the binary system injections the BT model was used, although as no relativistic parameters were included any of the models could have been used. Figure 3.3 shows

[2]This is a difference between the code used to create the signals which took in values of T_0 in the SSB frame and then corrected to the pulsar rest frame, and the code used to extract them which follows the TEMPO convention of defining all epochs in the pulsar rest frame.

the extracted pdfs of h_0 and ϕ_0 for the 10 isolated pulsar injections, where again ι and ψ were held fixed at their known values. Unlike the S3 injection pdfs in figure 3.1 there

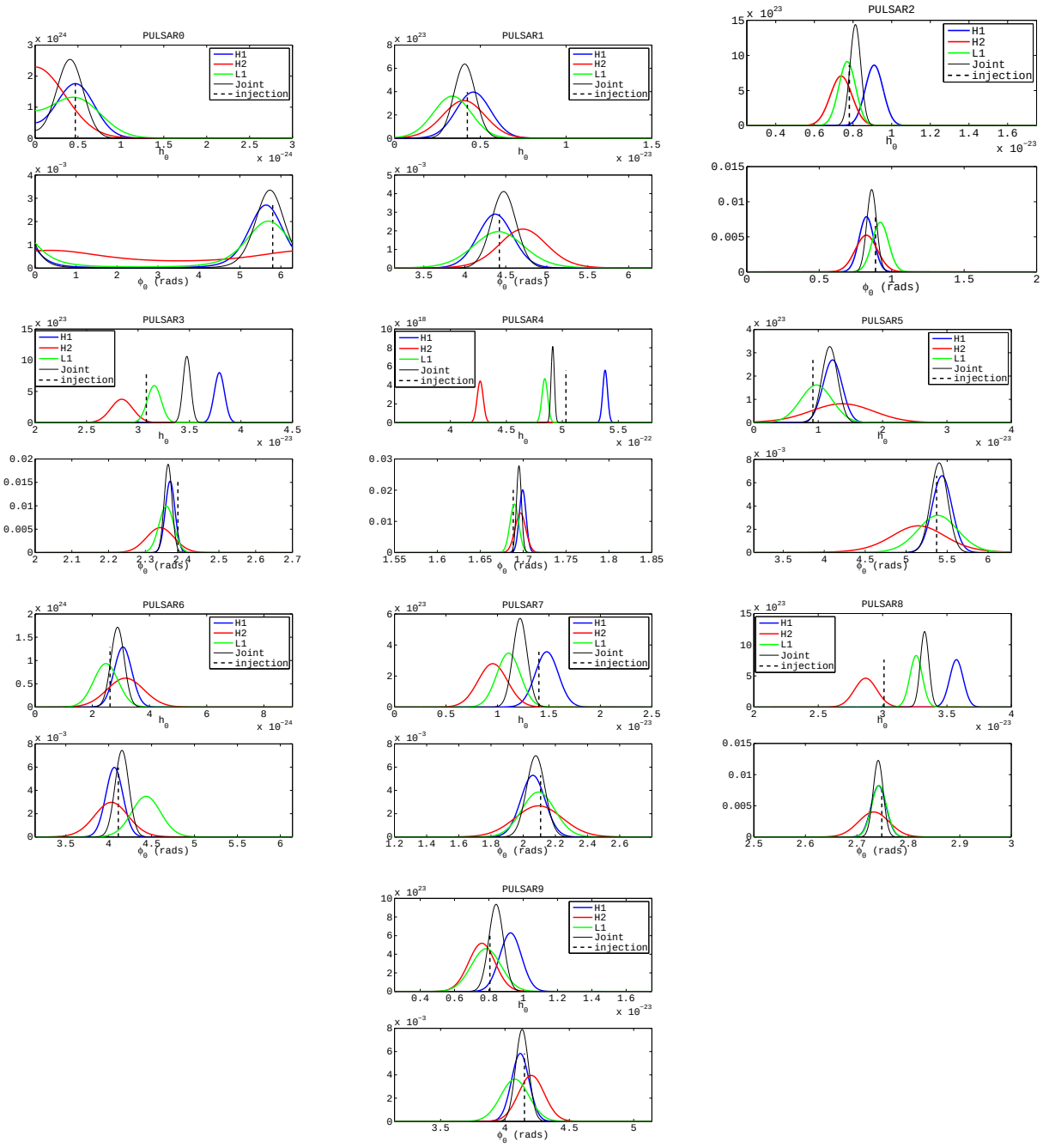

Figure 3.3: The pdfs of h_0 and ϕ_0 for 10 isolated pulsar injections into the LIGO detectors during S4.

have been no amplitude corrections applied to the S4 pdfs, because the calibrations used to calculate the injections and extract the injections are very similar. Due to the phase consistency between the detectors the joint likelihood, using all three detectors, have also been calculated. In general the values of h_0 are well matched with the

injection values. Again there are possible systematics which could affect the position of the pdfs. For S4 the actuation functions used to calculate the injection amplitudes and those used to calculate the final response function are much more similar than those for S3, with a ratio close to unity. The actuation phases are also very closely matched.

Figure 3.4 shows the pdfs for the two binary system pulsar injections. These show

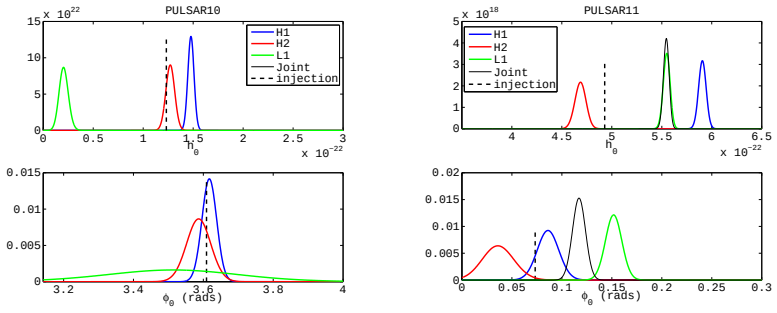

Figure 3.4: The pdfs of h_0 and ϕ_0 for the 2 binary pulsar injections into the LIGO detectors during S4.

similar matches to their injected values as the isolated pulsars. This is a good confirmation that the binary timing code can track the phase well and has no sign errors (assuming the independent injection code also does not contain the same sign errors). Here the main apparent error is the amplitude of PULSAR10 in L1, which appears a factor of ~ 4 lower than it should. At present the source of this error is unknown, although as the amplitude for PULSAR10 was derived from that of PULSAR3 multiplied by four, it could just be that this multiplication was left out.

3.3 Pulsar selection

The first criterion for selecting known pulsars to be included in this search was their frequency, the limiting factor being the low frequency noise floor of the detector. Below about 50 Hz the noise floor of the LIGO detectors increases rapidly making searches below this frequency a poor prospect. This is shown as a law of diminishing returns by equation 2.2 where the pulsar amplitude goes as ν^2, but the noise floor rises dramatically at low frequencies, so in general pulsar gravitational wave amplitudes will be

smaller in a frequency range that has a far worse detector sensitivity. The choice of a 50 Hz gravitational wave frequency cut-off (pulsar spin frequency of 25 Hz) is still somewhat arbitrary, but it also in some ways represents the split between the population of fast (millisecond/recycled and young) pulsars and slow pulsars.

The first stage of the selection process involved using the ATNF online pulsar catalogue [47] (described in Manchester *et al.*, 2005 [90]) which provides a list of pulsars and their parameters. As stated in Chapter 2 this catalogue shows that there are currently 150 pulsars with spin frequencies > 25 Hz. The accuracy of these parameters varies for each pulsar, and is dependent on several factors such as when it was discovered, how often it is monitored or even whether the catalogue has been recently updated with current best fits. The accuracy of the parameters is important in our search to make sure parameter errors do not lead to unacceptable phase errors in the heterodyne. Also important is the epoch of the parameters as more recent measurement will better reflect to current state of the pulsar. Such considerations are not a problem for the Crab pulsar as it is monitored on a very regular basis, so parameters are continuously updated [73]. Working closely with Andrew Lyne and Michael Kramer from Jodrell Bank Observatory we were supplied with up-to-date parameter information on as many pulsars as possible. They provided us with parameters for 75 pulsars for which recent timing data from around the period of the S3 run was available. For many of the other pulsars recent timing was either not present or unobtainable. For all pulsars the parameters were estimated using the whole set of data available. For pulsars where their timing straddled S3, the frequency (and occasionally frequency derivative) parameters were then re-estimated over that period with the other parameters held fixed at their previously calculated values. When Tempo fits a parameter it will calculate the associated uncertainty on that parameter (ostensibly a 1σ error, although in reality it is more commonly assumed to be $\sim \frac{1}{2}\sigma$), but no uncertainty will be produced if the parameter is fixed. This meant that if the pulsar parameters were re-fitted over S3 any uncertainty associated with the fixed parameters would be folded into the estimate of the freely varying frequency parameters (including effects of timing noise for example).

Since we are not terribly concerned with how good the fits are, but only whether the best parameters allow us to model the phase accurately (i.e. can they be used to unwind what TEMPO did to produce them) the parameter values should be exactly what we need for S3.

The final number of pulsars used for the S3 and S4 analyses is 93. The extra pulsars had their parameters taken from the most recent values on the ATNF catalogue, except PSR J0537-6910 for which parameters were taken from Marshall *et al.* (2004) [50] and the Crab pulsar where parameters were taken from the monthly ephemeris [73]. This still left 57 pulsars out of the analysis for which a judgement was made that the parameters were not defined accurately enough for our needs. This judgement call was easy for many of the newly discovered pulsars (for example the 21 newly discovered milliseconds pulsars in the Terzan 5 globular cluster in Ransom *et al.*, 2005 [91]) where simply not enough observations have been collected to give good parameter estimates.

3.3.1 Parameter checking

For pulsars where the radio parameter estimation was not performed over the epoch of S3, as timing was unavailable, it is worth checking whether the parameter errors could be enough to cause serious uncertainties in the heterodyne phase. For all pulsars this is an important consideration for the S4 run as no new timing has yet been obtained for this period. For all pulsars there are positional errors, which could affect the solar system barycentring time delay, and there are frequency and frequency derivative errors, all of which can affect the phase accuracy. For pulsars in binary systems there are errors associated with all the binary orbital parameters, which can again affect the phase through barycentring time delay errors. These errors are not necessarily uncorrelated though, for example the error on frequency could affect the accuracy of the first frequency derivative, and the binary time of periastron and longitude of periastron are highly correlated.

It is useful to see what effect these errors have on the phase over the course of S3 and S4, by propagating them over the period of the runs. We can just add/subtract

errors from the best fit values of all the parameters and work out the combination which gives a maximum phase deviation from that found using the best fit values. Due to the correlations between certain parameters this will give a conservative limit on the maximum phase error. TEMPO can be used to produce a covariance matrix for each of these parameters, which would take into account the correlations, but unfortunately this was not done for the parameters produced for S3.

When applying this we chose a criterion that any phase error $> 30°$ is unacceptable. This criterion was somewhat arbitrary, but was thought to be a reasonable compromise as it is small enough not cause a too much decoherence of a possible signal and large enough to avoid excluding too many pulsars. Applying this to S3 it is seen that 13 pulsars lie above this limit[3]. Eight of these are in binary systems: PSRs J0024-7204H, J0407+1607, J0437-4715, J1420-5625, J1518+0205B, J1709+2313, J1740-5340 and J1918-0642, and five are isolated: PSRs J0030+0451, J0537-6910, J1721-2457, J1730-2304 and J1910-5959B. For five of the binary systems it is the T_0 and ω_0 parameters which contribute most to the phase error. However, it also the case that these pulsars are in very low eccentricity (highly circular) orbits, thus meaning the errors on the T_0 and ω_0 parameters are intrinsically hard to measure and will most likely be far smaller than the quoted value. For these pulsars we can recalculate the phase error with the errors on T_0 and ω_0 set to zero and we find that for four of them (PSRs J0024-7204H, J0407+1607, J1420-5625, J1709+2313) the error now falls below our limit of $30°$. For the other pulsars it is the error on the frequency and/or position parameters, or in a couple of the binary cases the period error, which contribute most to the phase error.

Applying this to S4, using the above phase error limit, we actually have one pulsar (PSR J1910-5959B) fall back below the limit leaving 12 pulsars above it. This is due to the frequency parameter errors contributing most to the phase error for this pulsar and therefore with the shorter timespan of S4 not so much phase error could accumulate. If new parameter estimations over the period of S4 are made then these will be used

[3]for tables of errors see `http://www.astro.gla.ac.uk/~matthew/analyses/ParamErrors.htm`.

in the future.

This is not to say that for the pulsars where the phase error is possibly large it will be, as these are the worst case values. Therefore, results for these pulsars will still be given, but will retain a caveat that they could be unreliable due to possible phase errors. This could mean that for pulsars where the maximum phase error $\Delta\phi_{\rm max}$ is $< 90^\circ$ the upper limits may need scaling by $\sim 1/\cos\Delta\phi_{\rm max}$, and if $\Delta\phi_{\rm max}$ is $\geq 90^\circ$ the results will have to be discarded. With our limit of 30° this would lead to a scaling in amplitude of $\sim 15\%$. In general results just reflect the noise floor anyway, although it would be wrong to say that an upper limit was for a particular pulsar, rather than for just a particular area of the noise floor, if it was known that the phase used in the search was definitely wrong. Here we will give the best fit parameter values the benefit of the doubt and accept them all as correct, with the above caveat. In the future when we obtain pulsar timing we will be supplied with the covariance matrix of the parameters, thus allowing us to calculate phase errors in a far more rigorous and non-conservative way.

3.3.2 Timing noise

Timing noise was described in Chapter 2 with particular focus on the Crab pulsar. For the Crab pulsar the timing noise can be taken account of via a second heterodyne procedure as its phase evolution is regularly followed. For other pulsars some way to estimate the effect of timing noise on its phase is needed that does not rely on continuous observation. One such estimate is the Δ_8 parameter given by equations 2.28 and 2.29, which provides a cumulative phase error by assuming the measured $\ddot{\nu}$ is dominated by timing noise. Therefore, this can only really be estimated empirically for pulsars for which a value of the second frequency derivative has been measured. For other pulsars an estimate can be made using the linear relation fit between the period derivative $\dot{P}$ and Δ_8 in Arzoumanian *et al.* (1994) [68] as given in equation 2.29. The values of Δ_8 and its corresponding cumulative rotational phase error are given in table 3.5 and shown in figure 3.5. Figure 3.5 also shows a linear fit to values for which

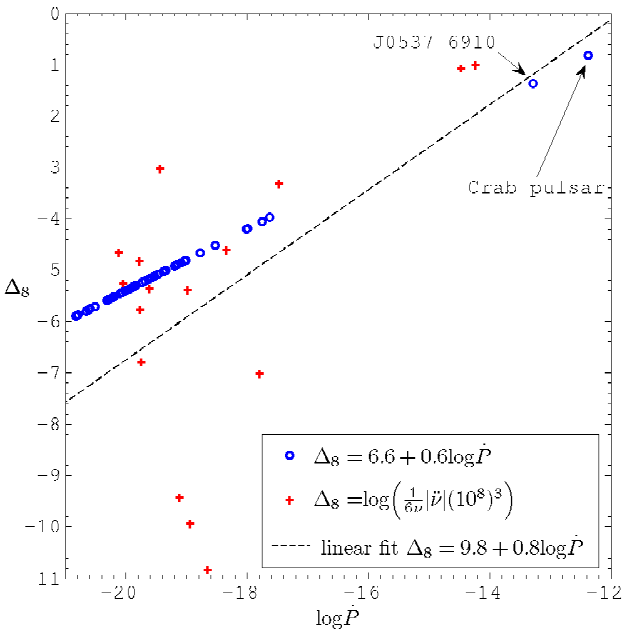

Figure 3.5: The values of Δ_8 for our selection of pulsars.

$\ddot{\nu}$ has been used to calculate Δ_8 given by $\Delta_8 = 8.9 + 0.8\log\dot{P}$. If this fit was to be used instead of equation 2.29 (which was fitted by eye) it would make little difference for the majority of pulsars as their Δ_8 values are already small. For the linear fit a value of the intrinsic spin-down (discussed in more detail in §3.4) has been used when available and if positive. For pulsars which were re-timed over the period of S3 timing noise should not be a problem at all (for the S3 analysis at least) as any timing noise, which usually has variations on time scales of several month to years, will have been folded into the other parameters.

Table 3.5: Values of Δ_8 and associated phase error.

PULSAR	ν	$\log\dot{P}$	Δ_8	phase error (degs)
J0024-7204E	282.8	-19.02	-4.81	3.2
J0024-7204F	381.2	-19.20	-4.92	3.3
J0024-7204Q	247.9	-19.47	-5.08	1.5
J0024-7204T	131.8	-18.53	-4.52	2.9
J0024-7204U	230.3	-19.03	-4.82	2.5
J0030+0451	205.5	-20.00	-5.40	0.6
J0034-0534	532.7	-20.30	-5.58	1.0
J0218+4232	430.5	-19.11	-9.43	0.0
J0407+1607	38.9	-19.10	-4.86	0.4
J0437-4715	173.7	-19.73	-5.24	0.7
J0534+2200	29.8	-12.37	-0.82	3216.4
J0537-6910	62.0	-13.29	-1.37	1898.8
J0613-0200	326.6	-20.06	-5.44	0.9
J0621+1002	34.7	-19.34	-5.00	0.2
J0711-6830	182.1	-20.08	-5.45	0.5

J0737-3039	44.1	-17.75	-4.05	2.8
J0751+1807	287.5	-20.11	-4.67	4.4
J1012+5307	190.3	-19.77	-5.77	0.2
J1022+1001	60.8	-19.36	-5.02	0.4
J1024-0719	193.7	-19.73	-5.24	0.8
J1045-4509	133.8	-19.85	-5.31	0.5
J1300+1240	160.8	-18.94	-9.95	0.0
J1420-5625	29.3	-19.17	-4.90	0.3
J1435-6100	107.0	-19.62	-5.17	0.5
J1455-3330	125.2	-19.61	-5.38	0.4
J1518+0205A	180.1	-19.38	-5.03	1.2
J1537+1155	26.4	-17.63	-3.98	2.0
J1603-7202	67.4	-19.95	-5.37	0.2
J1629-6902	166.6	-20.00	-5.40	0.5
J1640+2224	316.1	-20.79	-5.87	0.3
J1643-1224	216.4	-19.84	-5.30	0.8
J1709+2313	215.9	-20.83	-5.90	0.2
J1713+0747	218.8	-20.10	-5.46	0.5
J1721-2457	286.0	-20.23	-5.54	0.6
J1730-2304	123.1	-19.47	-5.08	0.7
J1732-5049	188.2	-19.86	-5.32	0.7
J1740-5340	273.9	-18.77	-4.66	4.3
J1744-1134	245.4	-20.05	-5.26	1.0
J1745-0952	51.6	-19.02	-4.81	0.6
J1748-2446A	86.5	-19.44	-3.04	56.9
J1756-2251	35.1	-17.99	-4.20	1.6
J1757-5322	112.7	-19.58	-5.15	0.6
J1801-1417	275.9	-20.28	-5.57	0.5
J1802-2124	79.1	-19.14	-4.89	0.7
J1804-0735	43.3	-18.35	-4.62	0.7
J1804-2717	107.0	-19.39	-5.03	0.7
J1810-2005	30.5	-18.65	-10.84	0.0
J1823-3021A	183.8	-17.47	-3.32	62.8
J1824-2452	327.4	-17.79	-7.03	0.0
J1843-1113	541.8	-20.02	-5.41	1.5
J1857+0943	186.5	-19.75	-6.80	0.0
J1905+0400	264.2	-20.31	-5.59	0.5
J1909-3744	339.3	-20.22	-5.53	0.7
J1910-5959A	306.2	-20.51	-5.71	0.4
J1910-5959C	189.5	-20.66	-5.79	0.2
J1910-5959D	110.7	-18.02	-4.21	4.9
J1911-1114	275.8	-20.20	-5.52	0.6
J1913+1011	27.8	-14.47	-1.07	1689.2
J1918-0642	130.8	-19.62	-5.17	0.6
J1939+2134	641.9	-18.98	-5.40	1.8
J1952+3252	25.3	-14.23	-1.02	1754.4
J1955+2908	163.0	-19.54	-5.13	0.9
J1959+2048	622.1	-19.77	-4.83	6.6
J2019+2425	254.2	-20.59	-5.76	0.3
J2051-0827	221.8	-19.90	-5.34	0.7
J2124-3358	202.8	-19.69	-5.21	0.9
J2129-5721	268.4	-19.68	-5.21	1.2
J2145-0750	62.3	-19.53	-5.12	0.3
J2229+2643	335.8	-20.82	-5.89	0.3
J2317+1439	290.3	-20.62	-5.77	0.4
J2322+2057	208.0	-20.02	-5.41	0.6

Almost all the timing noise phase errors are small enough to be negligible for our analysis. Using the same 30° phase error criterion as with the parameter errors we see that the estimated timing noise is not negligible for six pulsars: PSRs J0534+2200 (Crab pulsar), J0537-6910, J1748-2446A, J1823-3021A, J1913+1011, and J1952+3252. The Δ_8 values for the Crab pulsar and PSR J0537-6910 have been obtained from the linear relation even though they have very accurately measured values of $\ddot{\nu}$. This is because for these pulsars timing noise will not be the dominant component of $\ddot{\nu}$. The value for the Crab pulsar is not important as the timing noise is taken into account

with an extra heterodyne. For the other five pulsars it could be important, so these results will be flagged as possible problem pulsars. As for the pulsars with possible parameter errors all the results presented here will give the benefit of the doubt that timing noise has not had an adverse effect, therefore the results should be treated with caution.

There are pulsars in globular clusters for which there is no $\ddot{\nu}$ and $\dot{P}$ is negative ($\dot{\nu}$ is positive), so no value of Δ_8 can be assigned. For these pulsars the value of $\dot{\nu}$ (and therefore $\ddot{\nu}$) must be rather small to have been affected by globular cluster motions (discussed more in §3.4), so timing noise should be negligible.

3.3.3 The data

The results presented below make use of heterodyned data as described in Chapter 2. For each science run there were various cuts made in what data was used. The first and most obvious cut was to use only data taken when the detectors were in lock in so called science mode. This is data which has been deemed to be of good quality. The science mode segments were obtained using the LIGOtools [92] code `segwizard`. The length of times of these science mode segments represent the full data set for the runs.

The first cut after this was from dividing the data into the 60 seconds chunks that comprise each B_k value. This meant that up to 60 seconds could be lost from each locked stretch of data. The start of each locked stretch would also have, by definition, been preceded by a discontinuity in the data. Such a discontinuity would cause the filters in our analysis to ring and produce an apparent glitch in the B_ks. This being so the first B_k after the beginning of a lock stretch was removed in post-processing.

The heterodyning was performed on large computer clusters where the data was split up between the available computers. This splitting of data meant that it artificially introduced discontinuities in the data for each chunk. This would again ring the filters, so the first B_k was always removed. For the analysis on the LSC computer cluster at Caltech[4], with 580 processors, this meant that almost 10 hours of data was artificially

[4] `http://ldas-gridmon.ligo.caltech.edu/ganglia`

contaminated and removed. The Bayesian analysis we use makes the assumption of stationarity of the data over a certain length of time. In the previous analysis of S2 [34] this length of time was fixed at the fairly arbitrary value of 30 minutes, so the value of m_j in equation 2.23 was always 30. This meant that only contiguous 30 minutes segments could be used, again discarding more data. In our current analysis this 30 minute limit becomes the maximum length of a data segment, with segments smaller than this now being allowed. A lower limit on segment lengths of 5 minutes was set, as it was felt that very little more information could be added from segments shorter than this. This allowed the majority of the B_ks to contribute to the analysis.

In Dupuis (2004) [66] a Kolmogorov-Smirnoff test was used to check the validity of the assumption of stationarity over each 30 minute segment for S3. This generally showed about 20% of all segments did not conform to this assumption. Despite this all segments have been included, because as stated in §2.2 the Gaussian distribution is the least informative distribution and any deviations from it will be incorporated as extra noise.

3.4 Results

Here we will present 95% degree-of-belief upper limits on the amplitude of gravitational waves (h_0) emitted from the 93 pulsars as discussed above. The value of h_0 is independent of any assumptions about the neutron star other than it being triaxial and therefore emitting gravitational waves at twice its rotation frequency. The results will also be presented in terms of the pulsars' equatorial ellipticity $\varepsilon = (I_{xx} - I_{yy})/I_{zz}$, which under this assumption of triaxiality can be related to h_0 via

$$\varepsilon = 0.237 \left(\frac{h_0}{10^{-24}}\right) \left(\frac{r}{1\,\mathrm{kpc}}\right) \left(\frac{1\,\mathrm{Hz}^2}{\nu^2}\right) \left(\frac{10^{38}\,\mathrm{kg\,m}^2}{I_{zz}}\right), \tag{3.4}$$

where I_{zz} is the principle moment of inertia, r is the distance to the star and ν is the pulsar frequency[5] [34]. To obtain an upper limit on ε from that found for h_0 the

[5] *not* the gravitational wave signal frequency.

fiducial moment of inertia value of $I_{zz} = 10^{38}\,\mathrm{kg\,m^2}$ is generally used. The validity of this is discussed later.

The results are also presented in comparative terms as a ratio with the upper limit deduced from spin-down arguments via equation 2.3. This makes the assumption that all rotational energy is lost via gravitational wave emission, which for some cases is known to not be true (see §3.4.6). Despite this the spin-down limit is seen as a natural crossing point after which we can begin to speculate on the nature of the neutron star. The spin-down upper limit will obviously depend on the rate of spin-down, this value however, can be masked by radial and transverse motions of the object (see Lyne and Graham-Smith, 1998 [75]). The Shklovskii effect [93], in which the pulsar has a large transverse velocity v, will cause an apparent rate of change in the pulsars period of

$$\dot{P}_{\mathrm{S}} = \frac{v^2}{rc}P, \tag{3.5}$$

where r is the pulsar's distance. With its $1/r$ scaling this is obviously more prominent for close by pulsars. In the ATNF catalogue [47] values of the intrinsic period derivative $\dot{P}_{\mathrm{int}} = \dot{P} - \dot{P}_{\mathrm{S}}$ can be obtained with this effect corrected for. This provides an intrinsic spin-down rather than that measured[6], and for cases where it is available this is the value that is used for the spin-down ratio.

Another cause of changes to the observed pulsar $\dot{P}$ is if it is being accelerated in a gravitational field, like that of a globular cluster. If there is a radial component of the velocity v_r, then the observed value of $\dot{P} = (1 + v_r/c)\dot{P}_{\mathrm{int}}$ (Phinney, 1993 [94]). These effects can cause pulsars to have apparent spin-ups (seen in quite a large number of globular cluster pulsars) although are only strong enough to greatly effect pulsars with intrinsically small period derivatives. There are still many globular clusters for which the radial accelerations have not been measured, therefore no spin-down upper limit can be set, making the direct gravitational wave results a unique limit.

[6]Note that the heterodyne procedure still needs to make use of the measured spin-down rather than the intrinsic spin-down as these Doppler effects will have the same effect on the gravitational waves.

3.4.1 Marginalising over errors

Calibration errors

When calculating the pdfs for h_0 above there was no account taken of the errors/uncertainties in calibration. In previous work [33, 34] these have just been quoted as a percentage uncertainty in the final result. It is possible to fold the errors into the results, where it is in fact seen that they make no difference (under the assumption that the error is additional random noise). Following work done by Romano (2005) [95] we can model the calibration error as a extra parameter λ in our likelihood function, so

$$B_k \rightarrow \lambda B_k, \text{and } \sigma_j \rightarrow \lambda\sigma_j. \tag{3.6}$$

Applying this to equation 2.19 we get

$$p(\{B_k\}_j|\mathbf{a},\lambda) \propto \int_0^\infty \frac{1}{(\lambda\sigma_j)^{2m_j+1}} \exp\left(-\frac{1}{2(\lambda\sigma_j)^2}\sum_{k=1}^{m_j}|\lambda B_k - y_k|^2\right) \mathrm{d}(\lambda\sigma_\mathrm{j}), \tag{3.7}$$

which after integrating leaves

$$p(\{B_k\}_j|\mathbf{a},\lambda) \propto \frac{1}{\lambda^{2m_j}}\left(\sum|B_k - y_k/\lambda|^2\right)^{-m_j}. \tag{3.8}$$

If we use a uniform prior distribution for λ, and give some range for the calibration uncertainty between $\lambda_{\min}$ and $\lambda_{\max}$, we can marginalise over it,

$$p(\{B_k\}_j|\mathbf{a}) \propto \int_{\lambda_{\min}}^{\lambda_{\max}} \frac{1}{\lambda^{2m_j}}\left(\sum|B_k - y_k/\lambda|^2\right)^{-m_j} \mathrm{d}\lambda. \tag{3.9}$$

If we perform this integration numerically between $\lambda_{\min} = 1 - x$ and $\lambda_{\max} = 1 + x$, where x is our calibration uncertainty (e.g. 10%), it can be seen that the pdf remains identical to that without the uncertainty parameter added (figure 3.6). The use of a Jeffreys prior for λ would make little difference, with it just making the factor in equation 3.9 $1/\lambda^{2m_j-1}$. This result is not too surprising as if the value is just random noise with equal probability over an equal range either side of the obtained value then

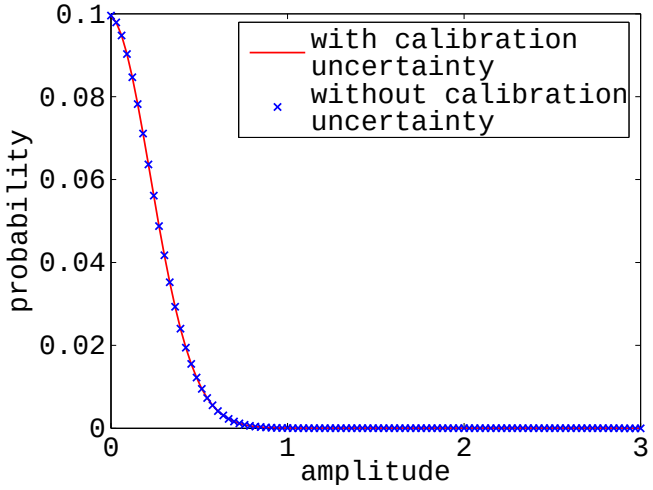

Figure 3.6: Comparison of pdfs calculated with a calibration uncertainty as in equation 3.9 compared to that from equation 2.23 without the calibration uncertainty.

that value will stay the most probable.

Distance errors

Another area of uncertainty is the distance to the pulsar. This is required when calculating the pulsars ellipticity. There are a variety of ways to measure pulsar distances, with the two main distance indicators being parallax, for nearby objects, and interstellar dispersion, for more distant sources. Measurements made using the dispersion measure make use of a model of the distribution of electron density within the galaxy, with the current best model being that of Taylor and Cordes (1993) [96]. Despite this there are still errors of about 10% on most measurements (see review of pulsar distance measurements in Frail and Weisberg, 1990 [97]). The majority of pulsar distance measurements provided in [47] make use of the Taylor and Cordes model, but it otherwise gives the best estimate. Plots of the pulsar distances from the Earth are shown in figure 3.7.

As with the calibration uncertainty we can take a similar view of the distance uncertainty, although this also requires a change of variable. We will assume that the distance error is a random number within a given distribution symmetric about the

Figure 3.7: Best estimate distances in kpc from the Earth for our 92 pulsars [47] (PSR J0537-6910 is left out as it is very distant in the LMC), where $x = r\cos\delta\cos\alpha$, $y = r\cos\delta\sin\alpha$ and $z = r\sin\delta$ are the normal conversions between spherical polar and Cartesian coordinates. The magenta circles represent pulsars in globular clusters.

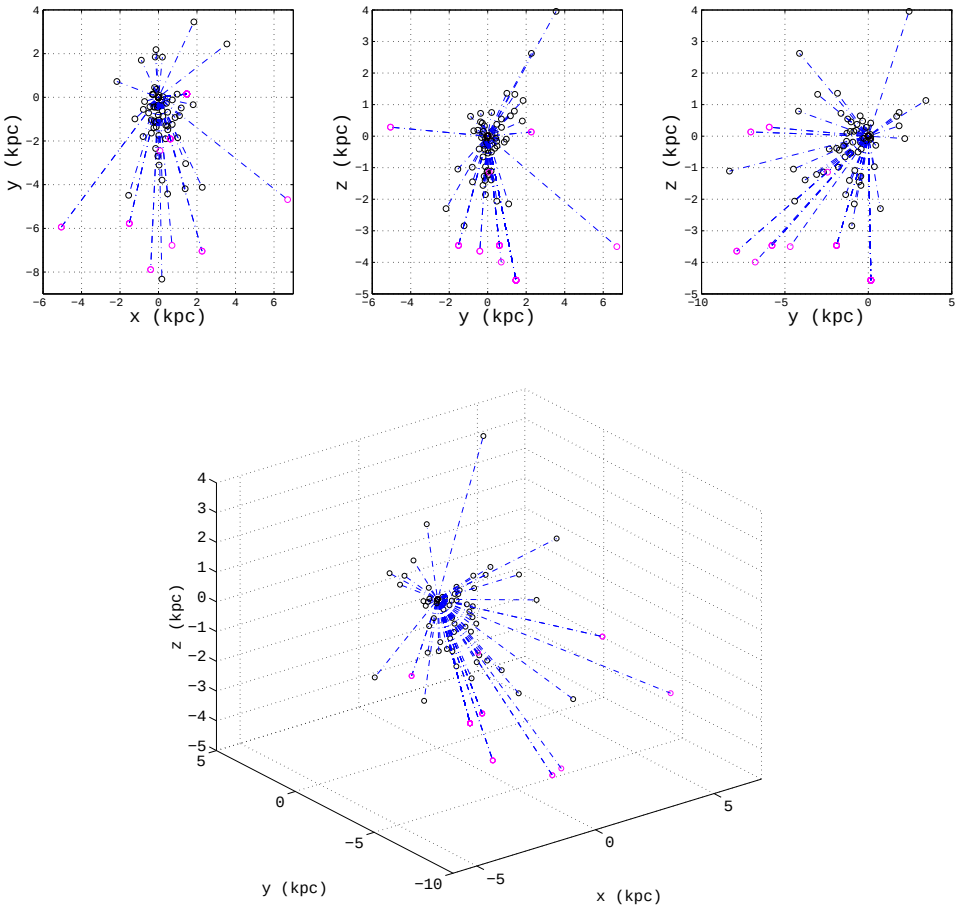

best estimate. To change variables from h_0 to ε the pdf is

$$p(\varepsilon|r) = p(h_0|r)\frac{\mathrm{d}h_0}{\mathrm{d}\varepsilon}, \tag{3.10}$$

which from differentiating equation 3.4 gives

$$p(\varepsilon|r) \propto \frac{p(h_0|r)}{r}. \tag{3.11}$$

From this we get

$$\begin{aligned} p(\varepsilon, r) &= p(\varepsilon|r)p(r), \\ &\propto \frac{p(h_0|r)}{r}p(r), \\ p(\varepsilon) &\propto \int \frac{p(h_0|r)}{r}p(r)\mathrm{d}r, \end{aligned} \tag{3.12}$$

which given a uniform distribution for $p(r)$ over a range $r_{\min}$ to $r_{\max}$, where $r_{\min} = r - 0.1r$ and $r_{\max} = r + 0.1r$ (assuming 10% errors from the best fit distance r), just gives $p(\varepsilon) \propto p(h_0)$. This is intuitively the case as if there is an equal probability that the pulsar is slightly closer or slightly further away, then the most probabilistically likely value would be the best fit value. This would be the same if the prior $p(r)$ were a Gaussian distribution about the best fit value. If there were not equal probability either side of the best fit this would not be the case, but for all our distance errors we shall assume it is.

3.4.2 S3

The S3 run was partaken with the three LIGO interferometers and GEO 600. These detectors had different duty cycles and sensitivities over the run. The collocated H1 and H2 interferometers maintained a relatively high duty cycle of $\sim$ 69.3% and $\sim$ 63.4% respectively[7]. The L1 interferometer was badly affected by anthropogenic noise sources during the day and thus had a relatively poor duty cycle of $\sim$ 21.8%. The

[7] `http://www.phys.lsu.edu/faculty/gonzalez/S3LockStats/`

GEO 600 interferometer did not operate for the full time of S3, but had two main data taking periods between which improvements were made to its sensitivity. These were from 5th to 12th November 2003, called S3 I, and 30th December 2003 to 13th January 2004, called S3 II. Typical sensitivities for these can be seen in figure 3.8. It can be seen

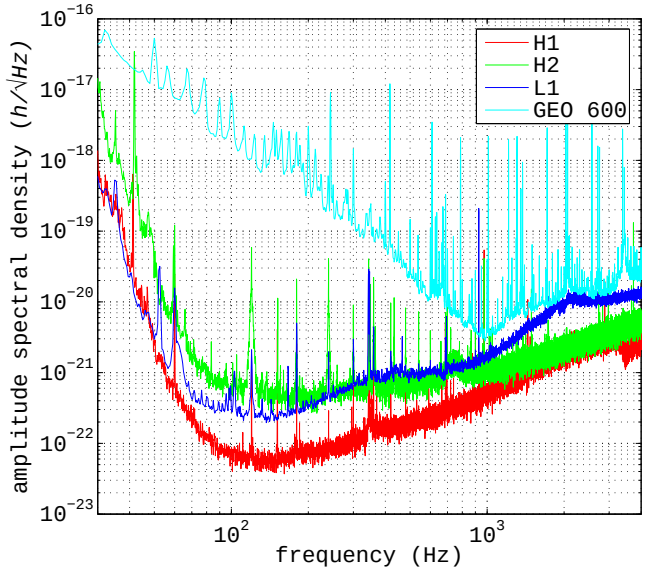

Figure 3.8: Typical sensitivity curves for the LIGO and GEO 600 interferometers over the period of S3. These curves have been reproduced using the official LIGO and GEO 600 sensitivities from [98, 99].

that GEO 600 only competes with the LIGO detectors for frequencies $\gtrsim 1\,\mathrm{kHz}$, where the signal recycling was tuned to. The LIGO detectors have their best sensitivities between ~ 100 and $200\,\mathrm{Hz}$.

The S3 injections suggest that there is phase consistency between the LIGO detectors, which allows a joint analysis combining the data from all interferometers. For all but one pulsar (PSR J1939+2134, the, until recently, fastest millisecond pulsar with $\nu_{\mathrm{gw}} \sim 1283.9\,\mathrm{Hz}$) it was not worth including GEO 600 data in the joint analysis. The phase coherence of GEO 600 with the LIGO interferometers was checked in [66]. The results of $h_0^{95\%}$ for each LIGO interferometer and the joint results, including ellipticity (assuming $I_{zz} = 10^{38}\,\mathrm{kg\,m^2}$ and the best estimate distances from [47]) are given in table 3.6. The results for PSR J1939+2134 including GEO 600 in the joint analysis are given in table 3.7.

Table 3.6: Results of the S3 analysis for the three LIGO interferometers. * denotes pulsars for which only a spin-up is measured and † denotes pulsars for which the spin-down is corrected for the Shklovskii effect. Pulsars for which timing noise might represent a problem are denoted by ‡ and those where the parameter errors might represent a problem are denoted by ⋄.

PULSAR	$h_0^{95\%}$ H1	$h_0^{95\%}$ H2	$h_0^{95\%}$ L1	$h_0^{95\%}$ Joint	ε	UL ratio
J0024-7204C	6.4×10^{-24}	3.8×10^{-24}	1.1×10^{-23}	3.1×10^{-24}	1.2×10^{-4}	*
J0024-7204D	2.0×10^{-24}	2.5×10^{-24}	5.8×10^{-24}	1.5×10^{-24}	4.8×10^{-5}	*
J0024-7204E	1.5×10^{-24}	3.5×10^{-24}	7.9×10^{-24}	1.4×10^{-24}	2.0×10^{-5}	1631†
J0024-7204F	2.4×10^{-24}	4.3×10^{-24}	1.2×10^{-23}	2.1×10^{-24}	1.7×10^{-5}	2576†
J0024-7204G	1.2×10^{-24}	2.9×10^{-24}	7.7×10^{-24}	1.1×10^{-24}	1.9×10^{-5}	*
J0024-7204H⋄	2.2×10^{-24}	4.8×10^{-24}	9.1×10^{-24}	2.4×10^{-24}	2.8×10^{-5}	*
J0024-7204I	1.9×10^{-24}	4.4×10^{-24}	8.4×10^{-24}	1.7×10^{-24}	2.3×10^{-5}	*
J0024-7204J	2.7×10^{-24}	7.9×10^{-24}	1.6×10^{-23}	2.7×10^{-24}	1.4×10^{-5}	*
J0024-7204L	1.3×10^{-24}	3.2×10^{-24}	6.4×10^{-24}	1.2×10^{-24}	2.5×10^{-5}	*
J0024-7204M	1.4×10^{-24}	3.7×10^{-24}	9.7×10^{-24}	1.4×10^{-24}	2.1×10^{-5}	*
J0024-7204N	1.8×10^{-24}	4.3×10^{-24}	9.5×10^{-24}	1.7×10^{-24}	1.8×10^{-5}	*
J0024-7204Q	1.4×10^{-24}	3.8×10^{-24}	6.5×10^{-24}	1.1×10^{-24}	2.0×10^{-5}	2274
J0024-7204S	2.7×10^{-24}	4.9×10^{-24}	10.0×10^{-24}	2.5×10^{-24}	2.3×10^{-5}	*
J0024-7204T	8.1×10^{-25}	2.4×10^{-24}	4.1×10^{-24}	7.5×10^{-25}	4.9×10^{-5}	718
J0024-7204U	2.0×10^{-24}	3.0×10^{-24}	6.2×10^{-24}	1.6×10^{-24}	3.5×10^{-5}	2079†
J0030+0451⋄	1.6×10^{-24}	3.6×10^{-24}	4.9×10^{-24}	1.4×10^{-24}	1.8×10^{-6}	279
J0034-0534	6.0×10^{-24}	7.6×10^{-24}	2.1×10^{-23}	4.0×10^{-24}	3.3×10^{-6}	3017
J0218+4232	3.0×10^{-24}	5.1×10^{-24}	1.3×10^{-23}	2.5×10^{-24}	1.9×10^{-5}	3117
J0407+1607⋄	1.8×10^{-24}	1.1×10^{-23}	9.1×10^{-24}	1.7×10^{-24}	1.1×10^{-3}	4958
J0437-4715⋄	8.1×10^{-24}	5.2×10^{-24}	1.2×10^{-23}	4.7×10^{-24}	5.1×10^{-6}	452†
J0534+2200	8.1×10^{-24}	9.1×10^{-23}	4.3×10^{-23}	7.6×10^{-24}	4.0×10^{-3}	5.3†
J0537-6910‡⋄	6.7×10^{-25}	6.6×10^{-24}	4.8×10^{-24}	6.6×10^{-25}	2.0×10^{-3}	23
J0613-0200	2.2×10^{-24}	5.5×10^{-24}	9.6×10^{-24}	2.0×10^{-24}	9.7×10^{-6}	3205†
J0621+1002	3.2×10^{-24}	2.8×10^{-23}	1.2×10^{-23}	2.9×10^{-24}	1.1×10^{-3}	5354†
J0711-6830	1.3×10^{-24}	6.1×10^{-24}	6.5×10^{-24}	1.1×10^{-24}	8.5×10^{-6}	1203†
J0737-3039A	1.1×10^{-24}	7.4×10^{-24}	7.4×10^{-24}	1.1×10^{-24}	7.8×10^{-5}	91
J0751+1807	1.7×10^{-24}	4.0×10^{-24}	7.2×10^{-24}	1.5×10^{-24}	8.7×10^{-6}	2521
J1012+5307	1.1×10^{-24}	2.4×10^{-24}	5.8×10^{-24}	1.1×10^{-24}	3.6×10^{-6}	442†
J1022+1001	8.6×10^{-25}	1.3×10^{-23}	8.8×10^{-24}	8.6×10^{-25}	1.6×10^{-5}	197
J1024-0719	1.7×10^{-24}	4.0×10^{-24}	4.5×10^{-24}	1.3×10^{-24}	2.9×10^{-6}	302
J1045-4509	1.2×10^{-24}	3.0×10^{-24}	4.1×10^{-24}	1.1×10^{-24}	4.8×10^{-5}	3311†
J1300+1240	1.3×10^{-24}	3.4×10^{-24}	4.3×10^{-24}	1.2×10^{-24}	8.3×10^{-6}	863†
J1420-5625⋄	5.6×10^{-24}	6.7×10^{-23}	3.0×10^{-23}	5.4×10^{-24}	2.6×10^{-3}	8232
J1435-6100	6.7×10^{-25}	2.6×10^{-24}	3.5×10^{-24}	6.3×10^{-25}	4.2×10^{-5}	1574
J1455-3330	9.0×10^{-25}	4.3×10^{-24}	5.4×10^{-24}	8.6×10^{-25}	9.6×10^{-6}	562†
J1518+0205A	2.3×10^{-24}	2.6×10^{-23}	1.6×10^{-23}	2.1×10^{-24}	1.2×10^{-4}	7627
J1518+0205B⋄	9.5×10^{-25}	4.8×10^{-24}	4.7×10^{-24}	9.9×10^{-25}	1.2×10^{-4}	*
J1537+1155	1.6×10^{-23}	10.0×10^{-23}	6.5×10^{-23}	1.6×10^{-23}	4.9×10^{-3}	2285†
J1603-7202	5.9×10^{-25}	3.2×10^{-24}	3.9×10^{-24}	5.7×10^{-25}	4.8×10^{-5}	1318†
J1623-2631	1.1×10^{-24}	4.5×10^{-24}	3.7×10^{-24}	1.1×10^{-24}	6.7×10^{-5}	383†
J1629-6902	9.3×10^{-25}	2.5×10^{-24}	5.1×10^{-24}	8.0×10^{-25}	9.2×10^{-6}	1041
J1640+2224	2.6×10^{-24}	4.2×10^{-24}	1.1×10^{-23}	2.6×10^{-24}	7.3×10^{-6}	5329†
J1643-1224	2.0×10^{-24}	5.5×10^{-24}	6.6×10^{-24}	1.7×10^{-24}	4.2×10^{-5}	5776†
J1701-3006A	1.1×10^{-24}	4.2×10^{-24}	4.7×10^{-24}	1.2×10^{-24}	5.2×10^{-5}	*
J1701-3006B	1.5×10^{-24}	3.9×10^{-24}	8.5×10^{-24}	1.4×10^{-24}	3.0×10^{-5}	*
J1701-3006C	1.5×10^{-24}	4.1×10^{-24}	7.3×10^{-24}	1.6×10^{-24}	3.8×10^{-5}	*
J1709+2313⋄	1.4×10^{-24}	4.6×10^{-24}	6.4×10^{-24}	1.4×10^{-24}	1.3×10^{-5}	5633†
J1713+0747	2.4×10^{-24}	6.5×10^{-24}	7.2×10^{-24}	2.5×10^{-24}	1.4×10^{-5}	2663†
J1721-2457⋄	2.3×10^{-24}	5.8×10^{-24}	8.6×10^{-24}	1.5×10^{-24}	6.8×10^{-6}	2260
J1730-2304⋄	1.1×10^{-24}	2.9×10^{-24}	4.6×10^{-24}	9.4×10^{-25}	7.5×10^{-6}	378
J1732-5049	1.0×10^{-24}	3.2×10^{-24}	5.3×10^{-24}	8.9×10^{-25}	1.1×10^{-5}	1233
J1740-5340⋄	1.4×10^{-24}	4.3×10^{-24}	7.5×10^{-24}	1.4×10^{-24}	1.0×10^{-5}	592
J1744-1134	1.6×10^{-24}	4.1×10^{-24}	5.5×10^{-24}	1.5×10^{-24}	2.1×10^{-6}	483†
J1745-0952	1.1×10^{-24}	5.1×10^{-24}	5.3×10^{-24}	1.1×10^{-24}	2.3×10^{-4}	1482
J1748-2446A‡	7.9×10^{-25}	2.7×10^{-24}	3.1×10^{-24}	7.7×10^{-25}	2.1×10^{-4}	*
J1748-2446C	8.3×10^{-25}	7.9×10^{-24}	3.5×10^{-24}	8.2×10^{-25}	1.2×10^{-4}	*
J1756-2251	2.3×10^{-24}	1.7×10^{-23}	1.2×10^{-23}	2.3×10^{-24}	1.3×10^{-3}	1422
J1757-5322	8.0×10^{-25}	3.7×10^{-24}	3.9×10^{-24}	7.3×10^{-25}	1.8×10^{-5}	715
J1801-1417	2.2×10^{-24}	4.8×10^{-24}	7.7×10^{-24}	1.7×10^{-24}	9.8×10^{-6}	3224
J1802-2124	9.6×10^{-25}	3.9×10^{-24}	3.6×10^{-24}	9.8×10^{-25}	1.2×10^{-4}	1704
J1804-0735	1.5×10^{-24}	7.4×10^{-24}	8.4×10^{-24}	1.5×10^{-24}	1.6×10^{-3}	3532
J1804-2717	9.3×10^{-25}	3.5×10^{-24}	3.5×10^{-24}	9.9×10^{-25}	2.4×10^{-5}	686
J1807-2459A	1.8×10^{-24}	5.0×10^{-24}	9.6×10^{-24}	1.6×10^{-24}	9.8×10^{-06}	*
J1810-2005	6.8×10^{-24}	7.1×10^{-23}	2.5×10^{-23}	6.5×10^{-24}	6.7×10^{-3}	15134
J1823-3021A‡	1.8×10^{-24}	3.8×10^{-24}	4.9×10^{-24}	1.7×10^{-24}	9.1×10^{-5}	649
J1824-2452	1.6×10^{-24}	4.5×10^{-24}	9.8×10^{-24}	1.6×10^{-24}	1.7×10^{-5}	416†
J1843-1113	5.5×10^{-24}	8.1×10^{-24}	2.0×10^{-23}	4.8×10^{-24}	7.7×10^{-6}	5167
J1857+0943	1.8×10^{-24}	3.8×10^{-24}	4.8×10^{-24}	1.8×10^{-24}	1.1×10^{-5}	1117†

J1905+0400	1.7×10^{-24}	5.9×10^{-24}	6.7×10^{-24}	1.7×10^{-24}	7.9×10^{-6}	2556
J1909-3744	1.8×10^{-24}	4.5×10^{-24}	1.1×10^{-23}	1.5×10^{-24}	2.6×10^{-6}	1095†
J1910-5959A	1.5×10^{-24}	4.9×10^{-24}	9.1×10^{-24}	1.3×10^{-24}	1.3×10^{-5}	6488
J1910-5959B$^{\diamond}$	7.1×10^{-25}	9.3×10^{-24}	5.5×10^{-24}	7.0×10^{-25}	4.6×10^{-5}	*
J1910-5959C	1.1×10^{-24}	2.9×10^{-24}	4.9×10^{-24}	1.1×10^{-24}	2.8×10^{-5}	8176
J1910-5959D	7.4×10^{-25}	4.3×10^{-24}	5.2×10^{-24}	8.2×10^{-25}	6.3×10^{-5}	394
J1910-5959E	1.2×10^{-24}	2.6×10^{-24}	5.8×10^{-24}	1.1×10^{-24}	2.1×10^{-5}	*
J1911+0101A	2.7×10^{-24}	4.9×10^{-24}	8.5×10^{-24}	1.9×10^{-24}	4.4×10^{-5}	*
J1911+0101B	2.2×10^{-24}	4.3×10^{-24}	5.3×10^{-24}	1.8×10^{-24}	9.3×10^{-5}	*
J1911-1114	1.8×10^{-24}	4.3×10^{-24}	9.4×10^{-24}	1.7×10^{-24}	8.6×10^{-6}	2617†
J1913+1011‡	1.3×10^{-23}	7.5×10^{-23}	4.0×10^{-23}	1.1×10^{-23}	1.5×10^{-2}	202
J1918-0642$^{\diamond}$	1.1×10^{-24}	3.3×10^{-24}	4.1×10^{-24}	9.4×10^{-25}	1.8×10^{-5}	926
J1939+2134	7.2×10^{-24}	7.7×10^{-24}	3.3×10^{-23}	5.0×10^{-24}	1.0×10^{-5}	2733†
J1952+3252‡	2.9×10^{-23}	2.5×10^{-22}	7.8×10^{-23}	3.1×10^{-23}	2.8×10^{-2}	247†
J1955+2908	1.7×10^{-24}	3.1×10^{-24}	4.8×10^{-24}	1.5×10^{-24}	7.0×10^{-5}	4497†
J1959+2048	6.2×10^{-24}	9.9×10^{-24}	2.8×10^{-23}	5.3×10^{-24}	4.9×10^{-6}	3769†
J2019+2425	1.9×10^{-24}	4.0×10^{-24}	6.9×10^{-24}	1.5×10^{-24}	4.9×10^{-6}	2075†
J2051-0827	1.4×10^{-24}	4.0×10^{-24}	6.9×10^{-24}	1.2×10^{-24}	7.6×10^{-6}	1187†
J2124-3358	1.1×10^{-24}	3.2×10^{-24}	5.4×10^{-24}	1.1×10^{-24}	1.6×10^{-6}	206†
J2129-5721	1.6×10^{-24}	3.9×10^{-24}	7.0×10^{-24}	1.4×10^{-24}	1.2×10^{-5}	2014†
J2140-2310A	7.7×10^{-25}	4.2×10^{-24}	3.6×10^{-24}	7.7×10^{-25}	2.0×10^{-4}	*
J2145-0750	8.7×10^{-25}	8.3×10^{-24}	3.9×10^{-24}	8.2×10^{-25}	2.5×10^{-5}	400†
J2229+2643	2.7×10^{-24}	5.5×10^{-24}	9.6×10^{-24}	2.4×10^{-24}	7.3×10^{-6}	6185
J2317+1439	3.5×10^{-24}	4.6×10^{-24}	7.9×10^{-24}	2.7×10^{-24}	1.4×10^{-5}	9406†
J2322+2057	1.6×10^{-24}	3.9×10^{-24}	6.6×10^{-24}	1.2×10^{-24}	5.0×10^{-6}	1229†

Table 3.7: The S3 results for PSR J1939+2134 including GEO 600 .

PULSAR	$h_0^{95\%}$ GEO 600	$h_0^{95\%}$ Joint	ε	spin-down UL ratio
J1939+2134	8.5×10^{-23}	5.0×10^{-24}	1.0×10^{-5}	2732†

It can be seen in table 3.7 that including GEO 600 in the analysis does not add significantly to the results.

3.4.3 S4

Between S3 and S4 the L1 interferometer was upgraded with better seismic isolation. This greatly reduced the amount of time the interferometer was thrown out-of-lock by anthropogenic noise, and allowed it to operate successfully during the day, with a duty cycle of $\sim$ 74.5% and a longest lock stretch of 18.7 hours. The H1 and H2 interferometers also both improved their duty cycles to $\sim$ 80.5% and $\sim$ 81.4%, with longest lock stretches of almost a day. The best sensitivities for all the detectors during S4 can be seen in figure 3.9.

The results of the S4 analysis for the LIGO interferometers is given in table 3.8. For S4 the GEO 600 interferometer provided two pulsars on a comparable scale to LIGO: PSR J1939+2134 and PSR J1843-1113. At present there has been no test of the phase consistency of the LIGO and GEO 600 interferometers during S4, although there is no

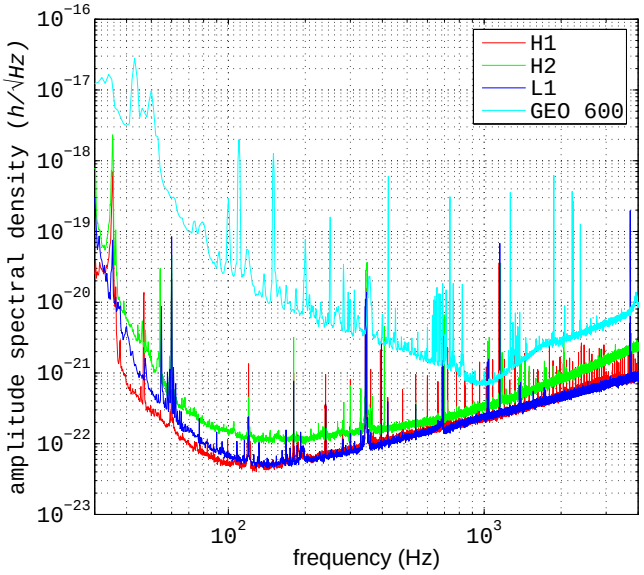

Figure 3.9: Best sensitivities of the LIGO and GEO 600 detectors during S4. These curves have been reproduced using the official LIGO and GEO 600 sensitivities from [98, 99].

reason to believe they are not coherent - no hardware injection was made in GEO 600 for S4.

Table 3.8: Results of the S4 analysis for the three LIGO interferometers. Superscripts are the same as in table 3.6

PULSAR	$h_0^{95\%}$ H1	$h_0^{95\%}$ H2	$h_0^{95\%}$ L1	$h_0^{95\%}$ Joint	ε	UL ratio
J0024-7204C	1.1×10^{-23}	3.3×10^{-24}	6.2×10^{-24}	3.1×10^{-24}	1.2×10^{-4}	*
J0024-7204D	1.2×10^{-24}	1.3×10^{-24}	1.3×10^{-24}	7.5×10^{-25}	2.5×10^{-5}	*
J0024-7204E	1.2×10^{-24}	1.4×10^{-24}	1.8×10^{-24}	8.4×10^{-25}	1.2×10^{-5}	961†
J0024-7204F	1.5×10^{-24}	2.4×10^{-24}	3.2×10^{-24}	1.2×10^{-24}	9.2×10^{-6}	1420†
J0024-7204G	9.9×10^{-25}	1.3×10^{-24}	1.7×10^{-24}	6.7×10^{-25}	1.2×10^{-5}	*
J0024-7204H$^{\diamond}$	1.6×10^{-24}	1.6×10^{-24}	1.8×10^{-24}	1.0×10^{-24}	1.2×10^{-5}	*
J0024-7204I	1.1×10^{-24}	1.4×10^{-24}	2.9×10^{-24}	9.7×10^{-25}	1.3×10^{-5}	*
J0024-7204J	1.8×10^{-24}	2.2×10^{-24}	4.8×10^{-24}	1.2×10^{-24}	6.0×10^{-6}	*
J0024-7204L	1.2×10^{-24}	1.3×10^{-24}	1.8×10^{-24}	1.0×10^{-24}	2.2×10^{-5}	*
J0024-7204M	1.1×10^{-24}	1.3×10^{-24}	1.7×10^{-24}	7.8×10^{-25}	1.2×10^{-5}	*
J0024-7204N	1.6×10^{-24}	1.9×10^{-24}	2.3×10^{-24}	9.2×10^{-25}	9.7×10^{-6}	*
J0024-7204Q	1.0×10^{-24}	1.2×10^{-24}	2.3×10^{-24}	8.7×10^{-25}	1.6×10^{-5}	1777
J0024-7204S	1.4×10^{-24}	1.6×10^{-24}	2.7×10^{-24}	9.1×10^{-25}	8.2×10^{-6}	*
J0024-7204T	6.4×10^{-25}	8.3×10^{-25}	9.1×10^{-25}	4.4×10^{-25}	2.9×10^{-5}	418
J0024-7204U	1.1×10^{-24}	1.2×10^{-24}	2.1×10^{-24}	6.6×10^{-25}	1.4×10^{-5}	849†
J0030+0451$^{\diamond}$	1.2×10^{-24}	2.0×10^{-24}	1.5×10^{-24}	7.6×10^{-25}	9.8×10^{-7}	153
J0034-0534	4.1×10^{-24}	4.4×10^{-24}	3.9×10^{-24}	1.9×10^{-24}	1.5×10^{-6}	1416
J0218+4232	1.9×10^{-24}	3.3×10^{-24}	3.2×10^{-24}	1.6×10^{-24}	1.2×10^{-5}	2024
J0407+1607$^{\diamond}$	1.5×10^{-24}	2.8×10^{-24}	1.5×10^{-24}	1.0×10^{-24}	6.5×10^{-4}	2936
J0437-4715$^{\diamond}$	1.4×10^{-23}	3.1×10^{-24}	6.8×10^{-24}	2.7×10^{-24}	3.0×10^{-6}	264†
J0534+2200	5.1×10^{-24}	8.2×10^{-24}	1.5×10^{-23}	4.4×10^{-24}	2.3×10^{-3}	3.1†
J0537-6910$^{\ddagger\diamond}$	4.7×10^{-25}	1.1×10^{-24}	1.2×10^{-24}	5.5×10^{-25}	1.7×10^{-3}	19
J0613-0200	2.2×10^{-24}	2.0×10^{-24}	2.1×10^{-24}	1.2×10^{-24}	5.7×10^{-6}	1887†
J0621+1002	1.6×10^{-24}	4.3×10^{-24}	1.6×10^{-24}	9.2×10^{-25}	3.4×10^{-4}	1700†
J0711-6830	1.1×10^{-24}	1.2×10^{-24}	1.5×10^{-24}	7.9×10^{-25}	5.9×10^{-6}	837†
J0737-3039A	8.4×10^{-25}	1.8×10^{-24}	1.0×10^{-24}	6.1×10^{-25}	4.2×10^{-5}	49
J0751+1807	1.8×10^{-24}	1.8×10^{-24}	2.2×10^{-24}	1.2×10^{-24}	7.1×10^{-6}	2057
J1012+5307	7.8×10^{-25}	1.1×10^{-24}	1.4×10^{-24}	5.1×10^{-25}	1.7×10^{-6}	212†
J1022+1001	1.1×10^{-24}	1.7×10^{-24}	7.4×10^{-25}	5.7×10^{-25}	1.1×10^{-5}	131
J1024-0719	1.3×10^{-24}	1.4×10^{-24}	1.3×10^{-24}	7.6×10^{-25}	1.7×10^{-6}	174
J1045-4509	8.3×10^{-25}	1.2×10^{-24}	1.2×10^{-24}	6.2×10^{-25}	2.7×10^{-5}	1816†
J1300+1240	1.5×10^{-24}	1.6×10^{-24}	9.8×10^{-25}	8.8×10^{-25}	6.2×10^{-6}	643†

J1420-5625$^{\diamond}$	3.8×10^{-24}	6.2×10^{-24}	5.1×10^{-24}	2.9×10^{-24}	1.4×10^{-3}	4472
J1435-6100	6.9×10^{-25}	1.0×10^{-24}	8.4×10^{-25}	4.1×10^{-25}	2.8×10^{-5}	1024
J1455-3330	6.8×10^{-25}	9.7×10^{-25}	1.3×10^{-24}	5.2×10^{-25}	5.8×10^{-6}	338†
J1518+0205A	3.4×10^{-24}	2.1×10^{-24}	1.7×10^{-24}	1.4×10^{-24}	8.0×10^{-5}	5007
J1518+0205B$^{\diamond}$	9.3×10^{-25}	1.8×10^{-24}	1.3×10^{-24}	5.4×10^{-25}	6.3×10^{-5}	*
J1537+1155	4.5×10^{-24}	1.2×10^{-23}	5.0×10^{-24}	2.7×10^{-24}	8.3×10^{-4}	383†
J1603-7202	5.0×10^{-25}	1.3×10^{-24}	8.9×10^{-25}	4.2×10^{-25}	3.6×10^{-5}	978†
J1623-2631	9.3×10^{-25}	1.9×10^{-24}	8.9×10^{-25}	7.5×10^{-25}	4.8×10^{-5}	273†
J1629-6902	8.6×10^{-25}	9.9×10^{-25}	1.1×10^{-24}	5.4×10^{-25}	6.3×10^{-6}	711
J1640+2224	1.8×10^{-24}	1.8×10^{-24}	2.2×10^{-24}	1.1×10^{-24}	3.1×10^{-6}	2277†
J1643-1224	1.3×10^{-24}	1.8×10^{-24}	1.5×10^{-24}	1.1×10^{-24}	2.8×10^{-5}	3821†
J1701-3006A	9.7×10^{-25}	1.5×10^{-24}	1.3×10^{-24}	6.8×10^{-25}	3.1×10^{-5}	*
J1701-3006B	1.2×10^{-24}	1.6×10^{-24}	2.8×10^{-24}	1.0×10^{-24}	2.1×10^{-5}	*
J1701-3006C	1.4×10^{-24}	1.5×10^{-24}	1.9×10^{-24}	9.2×10^{-25}	2.2×10^{-5}	*
J1709+2313$^{\diamond}$	1.1×10^{-24}	1.8×10^{-24}	1.7×10^{-24}	7.6×10^{-25}	7.1×10^{-6}	3059†
J1713+0747	1.3×10^{-24}	1.3×10^{-24}	1.6×10^{-24}	8.9×10^{-25}	4.9×10^{-6}	938†
J1721-2457$^{\diamond}$	1.4×10^{-24}	2.4×10^{-24}	1.7×10^{-24}	8.7×10^{-25}	3.9×10^{-6}	1303
J1730-2304$^{\diamond}$	7.6×10^{-25}	1.9×10^{-24}	8.8×10^{-25}	6.0×10^{-25}	4.7×10^{-6}	240
J1732-5049	1.3×10^{-24}	1.3×10^{-24}	1.8×10^{-24}	7.5×10^{-25}	9.1×10^{-6}	1046
J1740-5340$^{\diamond}$	1.2×10^{-24}	1.7×10^{-24}	1.7×10^{-24}	9.5×10^{-25}	6.9×10^{-6}	401
J1744-1134	1.9×10^{-24}	1.6×10^{-24}	1.4×10^{-24}	1.1×10^{-24}	1.5×10^{-6}	353†
J1745-0952	6.4×10^{-25}	1.7×10^{-24}	8.2×10^{-25}	5.0×10^{-25}	1.0×10^{-4}	662
J1748-2446A‡	5.5×10^{-25}	10.0×10^{-25}	1.0×10^{-24}	3.8×10^{-25}	1.1×10^{-4}	*
J1748-2446C	7.0×10^{-25}	1.3×10^{-24}	7.7×10^{-25}	4.3×10^{-25}	6.3×10^{-5}	*
J1756-2251	1.6×10^{-24}	5.2×10^{-24}	2.5×10^{-24}	1.6×10^{-24}	9.2×10^{-4}	997
J1757-5322	7.6×10^{-25}	9.1×10^{-25}	8.5×10^{-25}	4.5×10^{-25}	1.1×10^{-5}	437
J1801-1417	1.5×10^{-24}	1.8×10^{-24}	1.6×10^{-24}	9.1×10^{-25}	5.1×10^{-6}	1686
J1802-2124	7.6×10^{-25}	10.0×10^{-25}	8.0×10^{-25}	4.8×10^{-25}	6.1×10^{-5}	836
J1804-0735	9.2×10^{-25}	2.2×10^{-24}	1.0×10^{-24}	6.4×10^{-25}	6.8×10^{-4}	1490
J1804-2717	7.5×10^{-25}	9.4×10^{-25}	7.4×10^{-25}	4.9×10^{-25}	1.2×10^{-5}	340
J1807-2459A	1.4×10^{-24}	2.0×10^{-24}	1.8×10^{-24}	9.8×10^{-25}	5.9×10^{-6}	*
J1810-2005	4.3×10^{-24}	7.1×10^{-24}	4.6×10^{-24}	2.4×10^{-24}	2.5×10^{-3}	5612
J1823-3021A‡	1.3×10^{-24}	1.3×10^{-24}	1.2×10^{-24}	7.8×10^{-25}	4.3×10^{-5}	307
J1824-2452	1.7×10^{-24}	2.0×10^{-24}	2.3×10^{-24}	1.0×10^{-24}	1.1×10^{-5}	269†
J1843-1113	3.1×10^{-24}	3.3×10^{-24}	4.0×10^{-24}	1.8×10^{-24}	2.8×10^{-6}	1887
J1857+0943	1.3×10^{-24}	1.7×10^{-24}	1.1×10^{-24}	6.6×10^{-25}	4.1×10^{-6}	412†
J1905+0400	1.6×10^{-24}	2.1×10^{-24}	1.8×10^{-24}	1.3×10^{-24}	5.8×10^{-6}	1877
J1909-3744	1.7×10^{-24}	1.7×10^{-24}	2.4×10^{-24}	1.1×10^{-24}	1.9×10^{-6}	805†
J1910-5959A	1.7×10^{-24}	2.5×10^{-24}	2.1×10^{-24}	9.7×10^{-25}	9.8×10^{-6}	4974
J1910-5959B	2.4×10^{-24}	1.2×10^{-24}	1.0×10^{-24}	7.4×10^{-25}	4.9×10^{-5}	*
J1910-5959C	8.2×10^{-25}	1.1×10^{-24}	1.3×10^{-24}	6.7×10^{-25}	1.8×10^{-5}	5115
J1910-5959D	5.2×10^{-25}	9.9×10^{-25}	8.6×10^{-25}	4.1×10^{-25}	3.2×10^{-5}	198
J1910-5959E	9.7×10^{-25}	1.3×10^{-24}	1.3×10^{-24}	6.0×10^{-25}	1.2×10^{-5}	*
J1911+0101A	1.6×10^{-24}	1.9×10^{-24}	1.8×10^{-24}	9.3×10^{-25}	2.1×10^{-5}	*
J1911+0101B	1.2×10^{-24}	1.3×10^{-24}	1.1×10^{-24}	7.2×10^{-25}	3.7×10^{-5}	*
J1911-1114	1.4×10^{-24}	1.9×10^{-24}	2.1×10^{-24}	1.0×10^{-24}	4.9×10^{-6}	1504†
J1913+1011‡	3.2×10^{-24}	8.5×10^{-24}	5.2×10^{-24}	2.8×10^{-24}	3.8×10^{-3}	51
J1918-0642$^{\diamond}$	7.7×10^{-25}	1.2×10^{-24}	9.0×10^{-25}	4.8×10^{-25}	9.3×10^{-6}	470
J1939+2134	4.0×10^{-24}	4.2×10^{-24}	5.2×10^{-24}	2.4×10^{-24}	4.9×10^{-6}	1280†
J1952+3252‡	4.9×10^{-24}	10.0×10^{-24}	6.1×10^{-24}	4.0×10^{-24}	3.7×10^{-3}	33†
J1955+2908	8.0×10^{-25}	1.4×10^{-24}	1.2×10^{-24}	5.9×10^{-25}	2.8×10^{-5}	1837†
J1959+2048$^{\diamond}$	3.0×10^{-24}	4.7×10^{-24}	3.9×10^{-24}	2.1×10^{-24}	1.9×10^{-6}	1481†
J2019+2425	1.4×10^{-24}	1.6×10^{-24}	1.8×10^{-24}	8.5×10^{-25}	2.8×10^{-6}	1189†
J2051-0827	1.5×10^{-24}	1.8×10^{-24}	1.9×10^{-24}	1.0×10^{-24}	6.3×10^{-6}	983†
J2124-3358	1.2×10^{-24}	1.4×10^{-24}	1.3×10^{-24}	8.0×10^{-25}	1.1×10^{-6}	151†
J2129-5721	1.1×10^{-24}	1.4×10^{-24}	1.6×10^{-24}	7.8×10^{-25}	6.5×10^{-6}	1087†
J2140-2310A	6.2×10^{-25}	1.2×10^{-24}	9.7×10^{-25}	4.5×10^{-25}	1.1×10^{-4}	*
J2145-0750	6.7×10^{-25}	1.6×10^{-24}	6.8×10^{-25}	4.2×10^{-25}	1.3×10^{-5}	208†
J2229+2643	1.9×10^{-24}	3.2×10^{-24}	2.3×10^{-24}	1.4×10^{-24}	4.1×10^{-6}	3497
J2317+1439	1.6×10^{-24}	1.7×10^{-24}	1.9×10^{-24}	9.1×10^{-25}	4.9×10^{-6}	3238†
J2322+2057	1.2×10^{-24}	1.5×10^{-24}	1.6×10^{-24}	7.8×10^{-25}	3.3×10^{-6}	812†

The results with the two pulsars for which GEO 600 has been included are given in table 3.9. It can be seen that GEO 600 adds only fractionally to the overall sensitivity

Table 3.9: The S4 results including GEO 600 .

PULSAR	$h_0^{95\%}$ GEO 600	$h_0^{95\%}$ Joint	ε	spin-down UL ratio
J1843-1113	3.8×10^{-23}	1.8×10^{-24}	2.8×10^{-6}	1875
J1939+2134	2.6×10^{-23}	2.4×10^{-24}	4.9×10^{-6}	1300†

for PSR J1843-1113.

3.4.4 S3 and S4

Our analysis technique allows us to combine the data from different runs in a way similar to the ability to combine data from all the interferometers to create a joint results. This becomes useful when runs are of a similar sensitivity, which is the case for areas of the frequency spectrum for S3 and S4. The data can be combined by simply concatenating the separate calibrated B_k files together. This is valid provided that the calibration phase is consistent between runs.

The results for the LIGO interferometers are given in table 3.10.

Table 3.10: Results of the combined S3 and S4 analysis for the three LIGO interferometers. Superscripts are the same as in table 3.6

PULSAR	$h_0^{95\%}$ H1	$h_0^{95\%}$ H2	$h_0^{95\%}$ L1	$h_0^{95\%}$ Joint	ε	UL ratio
J0024-7204C	5.3×10^{-24}	2.4×10^{-24}	5.7×10^{-24}	2.1×10^{-24}	7.9×10^{-5}	*
J0024-7204D	8.0×10^{-25}	1.2×10^{-24}	1.4×10^{-24}	5.3×10^{-25}	1.7×10^{-5}	*
J0024-7204E	10.0×10^{-25}	1.2×10^{-24}	1.8×10^{-24}	7.8×10^{-25}	1.1×10^{-5}	890†
J0024-7204F	1.1×10^{-24}	2.3×10^{-24}	3.2×10^{-24}	8.8×10^{-25}	6.9×10^{-6}	1069†
J0024-7204G	8.2×10^{-25}	1.1×10^{-24}	1.6×10^{-24}	5.7×10^{-25}	1.1×10^{-5}	*
J0024-7204H$^{\diamond}$	1.4×10^{-24}	1.5×10^{-24}	1.8×10^{-24}	9.1×10^{-25}	1.1×10^{-5}	*
J0024-7204I	1.1×10^{-24}	1.3×10^{-24}	2.7×10^{-24}	9.9×10^{-25}	1.4×10^{-5}	*
J0024-7204J	1.6×10^{-24}	2.1×10^{-24}	4.8×10^{-24}	1.0×10^{-24}	5.2×10^{-6}	*
J0024-7204L	8.6×10^{-25}	1.2×10^{-24}	1.8×10^{-24}	8.4×10^{-25}	1.8×10^{-5}	*
J0024-7204M	9.6×10^{-25}	1.1×10^{-24}	1.8×10^{-24}	7.0×10^{-25}	1.1×10^{-5}	*
J0024-7204N	1.1×10^{-24}	1.5×10^{-24}	2.3×10^{-24}	7.2×10^{-25}	7.6×10^{-6}	*
J0024-7204Q	8.5×10^{-25}	1.1×10^{-24}	2.3×10^{-24}	6.7×10^{-25}	1.2×10^{-5}	1382
J0024-7204S	1.2×10^{-24}	1.4×10^{-24}	2.7×10^{-24}	9.1×10^{-25}	8.3×10^{-6}	*
J0024-7204T	5.8×10^{-25}	7.9×10^{-25}	8.7×10^{-25}	3.9×10^{-25}	2.6×10^{-5}	377
J0024-7204U	1.2×10^{-24}	1.0×10^{-24}	2.0×10^{-24}	7.3×10^{-25}	1.6×10^{-5}	943†
J0030+0451$^{\diamond}$	1.0×10^{-24}	1.9×10^{-24}	1.4×10^{-24}	7.4×10^{-25}	9.5×10^{-7}	148
J0034-0534	3.3×10^{-24}	3.9×10^{-24}	4.0×10^{-24}	1.6×10^{-24}	1.3×10^{-6}	1224
J0218+4232	1.5×10^{-24}	2.7×10^{-24}	3.0×10^{-24}	1.3×10^{-24}	9.8×10^{-6}	1643
J0407+1607$^{\diamond}$	1.1×10^{-24}	2.7×10^{-24}	1.5×10^{-24}	8.8×10^{-25}	5.6×10^{-4}	2535
J0437-4715$^{\diamond}$	7.3×10^{-24}	2.4×10^{-24}	6.5×10^{-24}	2.3×10^{-24}	2.5×10^{-6}	218†
J0534+2200	4.3×10^{-24}	8.3×10^{-24}	1.4×10^{-23}	3.8×10^{-24}	2.0×10^{-3}	2.7†
J0537-6910$^{\ddagger\diamond}$	3.9×10^{-25}	1.2×10^{-24}	1.2×10^{-24}	4.3×10^{-25}	1.3×10^{-3}	15
J0613-0200	1.4×10^{-24}	1.8×10^{-24}	2.1×10^{-24}	1.0×10^{-24}	4.9×10^{-6}	1619†
J0621+1002	1.5×10^{-24}	4.3×10^{-24}	1.5×10^{-24}	9.1×10^{-25}	3.4×10^{-4}	1680†
J0711-6830	7.4×10^{-25}	1.1×10^{-24}	1.5×10^{-24}	5.9×10^{-25}	4.4×10^{-6}	626†
J0737-3039A	6.4×10^{-25}	1.7×10^{-24}	1.0×10^{-24}	5.3×10^{-25}	3.7×10^{-5}	43
J0751+1807	1.4×10^{-24}	1.6×10^{-24}	2.3×10^{-24}	1.0×10^{-24}	6.0×10^{-6}	1747
J1012+5307	6.3×10^{-25}	9.8×10^{-25}	1.3×10^{-24}	4.5×10^{-25}	1.5×10^{-6}	185†
J1022+1001	7.4×10^{-25}	1.7×10^{-24}	7.2×10^{-25}	4.9×10^{-25}	9.4×10^{-6}	113
J1024-0719	1.0×10^{-24}	1.3×10^{-24}	1.3×10^{-24}	6.0×10^{-25}	1.3×10^{-6}	139
J1045-4509	6.6×10^{-25}	1.2×10^{-24}	1.1×10^{-24}	6.3×10^{-25}	2.7×10^{-5}	1833†
J1300+1240	1.2×10^{-24}	1.6×10^{-24}	9.9×10^{-25}	8.3×10^{-25}	5.9×10^{-6}	606†
J1420-5625$^{\diamond}$	3.2×10^{-24}	6.3×10^{-24}	5.1×10^{-24}	2.6×10^{-24}	1.2×10^{-3}	3987
J1435-6100	4.7×10^{-25}	8.2×10^{-25}	7.8×10^{-25}	3.4×10^{-25}	2.3×10^{-5}	850
J1455-3330	5.3×10^{-25}	1.0×10^{-24}	1.3×10^{-24}	4.6×10^{-25}	5.1×10^{-6}	299†
J1518+0205A	1.7×10^{-24}	2.1×10^{-24}	1.7×10^{-24}	1.1×10^{-24}	6.5×10^{-5}	4030
J1518+0205B$^{\diamond}$	6.7×10^{-25}	1.8×10^{-24}	1.2×10^{-24}	4.4×10^{-25}	5.1×10^{-5}	*
J1537+1155	4.4×10^{-24}	1.2×10^{-23}	4.9×10^{-24}	2.6×10^{-24}	8.0×10^{-4}	369†
J1603-7202	3.8×10^{-25}	1.2×10^{-24}	8.9×10^{-25}	3.2×10^{-25}	2.7×10^{-5}	743†
J1623-2631	6.9×10^{-25}	1.8×10^{-24}	8.9×10^{-25}	4.4×10^{-25}	2.8×10^{-5}	161†
J1629-6902	5.7×10^{-25}	8.9×10^{-25}	1.1×10^{-24}	4.3×10^{-25}	5.0×10^{-6}	567
J1640+2224	1.5×10^{-24}	1.7×10^{-24}	2.1×10^{-24}	1.0×10^{-24}	2.8×10^{-6}	2079†
J1643-1224	1.2×10^{-24}	1.8×10^{-24}	1.3×10^{-24}	1.1×10^{-24}	2.6×10^{-5}	3616†

J1701-3006A	7.1×10^{-25}	1.5×10^{-24}	1.2×10^{-24}	5.2×10^{-25}	2.3×10^{-5}	*
J1701-3006B	9.4×10^{-25}	1.5×10^{-24}	2.7×10^{-24}	8.1×10^{-25}	1.7×10^{-5}	*
J1701-3006C	9.4×10^{-25}	1.5×10^{-24}	1.9×10^{-24}	7.7×10^{-25}	1.8×10^{-5}	*
J1709+2313$^{\diamond}$	8.9×10^{-25}	1.8×10^{-24}	1.6×10^{-24}	6.6×10^{-25}	6.1×10^{-6}	2655†
J1713+0747	1.1×10^{-24}	1.4×10^{-24}	1.7×10^{-24}	8.0×10^{-25}	4.4×10^{-6}	838†
J1721-2457$^{\diamond}$	1.1×10^{-24}	1.9×10^{-24}	1.8×10^{-24}	7.2×10^{-25}	3.3×10^{-6}	1080
J1730-2304$^{\diamond}$	6.4×10^{-25}	1.6×10^{-24}	9.1×10^{-25}	4.4×10^{-25}	3.5×10^{-6}	176
J1732-5049	7.5×10^{-25}	1.0×10^{-24}	1.8×10^{-24}	5.6×10^{-25}	6.7×10^{-6}	772
J1740-5340$^{\diamond}$	8.9×10^{-25}	1.8×10^{-24}	1.7×10^{-24}	8.7×10^{-25}	6.3×10^{-6}	367
J1744-1134	1.4×10^{-24}	1.6×10^{-24}	1.4×10^{-24}	9.1×10^{-25}	1.3×10^{-6}	301†
J1745-0952	6.1×10^{-25}	1.7×10^{-24}	8.0×10^{-25}	4.7×10^{-25}	9.9×10^{-5}	623
J1748-2446A‡	4.4×10^{-25}	9.0×10^{-25}	1.0×10^{-24}	3.6×10^{-25}	9.8×10^{-5}	*
J1748-2446C	5.2×10^{-25}	1.3×10^{-24}	7.5×10^{-25}	3.9×10^{-25}	5.7×10^{-5}	*
J1756-2251	1.5×10^{-24}	5.0×10^{-24}	2.5×10^{-24}	1.6×10^{-24}	9.0×10^{-4}	976
J1757-5322	6.1×10^{-25}	9.0×10^{-25}	8.7×10^{-25}	4.2×10^{-25}	1.1×10^{-5}	409
J1801-1417	1.2×10^{-24}	1.7×10^{-24}	1.7×10^{-24}	7.9×10^{-25}	4.4×10^{-6}	1456
J1802-2124	6.7×10^{-25}	1.0×10^{-24}	7.7×10^{-25}	5.7×10^{-25}	7.1×10^{-5}	980
J1804-0735	7.0×10^{-25}	2.1×10^{-24}	1.0×10^{-24}	5.8×10^{-25}	6.1×10^{-4}	1336
J1804-2717	5.7×10^{-25}	9.0×10^{-25}	7.4×10^{-25}	4.7×10^{-25}	1.1×10^{-5}	329
J1807-2459A	1.1×10^{-24}	1.8×10^{-24}	1.8×10^{-24}	8.3×10^{-25}	4.9×10^{-6}	*
J1810-2005	3.2×10^{-24}	7.2×10^{-24}	4.5×10^{-24}	2.3×10^{-24}	2.4×10^{-3}	5342
J1823-3021A‡	1.1×10^{-24}	1.2×10^{-24}	1.1×10^{-24}	6.8×10^{-25}	3.8×10^{-5}	269
J1824-2452	1.2×10^{-24}	1.7×10^{-24}	2.2×10^{-24}	8.4×10^{-25}	9.0×10^{-6}	221†
J1843-1113	2.7×10^{-24}	3.0×10^{-24}	4.0×10^{-24}	1.6×10^{-24}	2.5×10^{-6}	1690
J1857+0943	1.1×10^{-24}	1.7×10^{-24}	1.1×10^{-24}	6.2×10^{-25}	3.8×10^{-6}	388†
J1905+0400	1.1×10^{-24}	1.7×10^{-24}	1.7×10^{-24}	9.8×10^{-25}	4.5×10^{-6}	1440
J1909-3744	1.4×10^{-24}	1.5×10^{-24}	2.2×10^{-24}	8.8×10^{-25}	1.5×10^{-6}	628†
J1910-5959A	1.1×10^{-24}	1.7×10^{-24}	2.0×10^{-24}	7.6×10^{-25}	7.6×10^{-6}	3863
J1910-5959B	6.8×10^{-25}	1.2×10^{-24}	10.0×10^{-25}	5.1×10^{-25}	3.4×10^{-5}	*
J1910-5959C	6.3×10^{-25}	9.8×10^{-25}	1.2×10^{-24}	5.0×10^{-25}	1.3×10^{-5}	3852
J1910-5959D	4.6×10^{-25}	9.5×10^{-25}	9.0×10^{-25}	4.1×10^{-25}	3.2×10^{-5}	198
J1910-5959E	8.1×10^{-25}	1.1×10^{-24}	1.3×10^{-24}	5.6×10^{-25}	1.1×10^{-5}	*
J1911+0101A	1.1×10^{-24}	1.8×10^{-24}	1.8×10^{-24}	7.8×10^{-25}	1.8×10^{-5}	*
J1911+0101B	1.2×10^{-24}	1.2×10^{-24}	1.2×10^{-24}	8.0×10^{-25}	4.0×10^{-5}	*
J1911-1114	1.1×10^{-24}	1.7×10^{-24}	2.2×10^{-24}	8.7×10^{-25}	4.3×10^{-6}	1308†
J1913+1011‡	3.1×10^{-24}	8.6×10^{-24}	5.0×10^{-24}	2.6×10^{-24}	3.5×10^{-3}	47
J1918-0642$^{\diamond}$	6.1×10^{-25}	1.1×10^{-24}	8.2×10^{-25}	4.6×10^{-25}	8.8×10^{-6}	449
J1939+2134	3.5×10^{-24}	3.8×10^{-24}	5.3×10^{-24}	2.0×10^{-24}	4.0×10^{-6}	1063†
J1952+3252‡	4.5×10^{-24}	10.0×10^{-24}	6.0×10^{-24}	3.6×10^{-24}	3.3×10^{-3}	30†
J1955+2908	6.9×10^{-25}	1.3×10^{-24}	1.2×10^{-24}	5.0×10^{-25}	2.4×10^{-5}	1558†
J1959+2048$^{\diamond}$	2.8×10^{-24}	4.6×10^{-24}	3.8×10^{-24}	1.9×10^{-24}	1.8×10^{-6}	1363†
J2019+2425	1.3×10^{-24}	1.5×10^{-24}	1.9×10^{-24}	8.0×10^{-25}	2.7×10^{-6}	1114†
J2051-0827	1.1×10^{-24}	1.7×10^{-24}	1.9×10^{-24}	8.5×10^{-25}	5.2×10^{-6}	814†
J2124-3358	7.7×10^{-25}	1.2×10^{-24}	1.3×10^{-24}	5.9×10^{-25}	8.5×10^{-7}	112†
J2129-5721	1.0×10^{-24}	1.4×10^{-24}	1.6×10^{-24}	7.5×10^{-25}	6.2×10^{-6}	1038†
J2140-2310A	4.7×10^{-25}	1.2×10^{-24}	9.1×10^{-25}	3.7×10^{-25}	9.5×10^{-5}	*
J2145-0750	5.6×10^{-25}	1.5×10^{-24}	6.6×10^{-25}	4.0×10^{-25}	1.2×10^{-5}	195†
J2229+2643	1.4×10^{-24}	2.7×10^{-24}	2.3×10^{-24}	9.3×10^{-25}	2.8×10^{-6}	2357
J2317+1439	1.5×10^{-24}	1.6×10^{-24}	1.9×10^{-24}	8.7×10^{-25}	4.6×10^{-6}	3091†
J2322+2057	1.0×10^{-24}	1.3×10^{-24}	1.3×10^{-24}	6.7×10^{-25}	2.9×10^{-6}	702†

GEO 600 was included in the joint analysis for the same two pulsars as the S4 results (see table 3.11). For the vast majority of pulsars combining the two runs improves the

Table 3.11: The combined S3 and S4 results including GEO 600 .

PULSAR	$h_0^{95\%}$ GEO 600	$h_0^{95\%}$ Joint	ε	spin-down UL ratio
J1843-1113	3.7×10^{-23}	1.6×10^{-24}	2.5×10^{-6}	1671
J1939+2134	2.5×10^{-23}	2.0×10^{-24}	4.1×10^{-6}	1071†

results, although for a few the S3 data has a detrimental effect (of a few percent) with the S4 data providing the lowest upper limit.

The upper limits on h_0 and ε from the S3, S4 and the combined data set are plotted in figures 3.10 and 3.11. Figure 3.10 also shows an estimate of the upper limit across

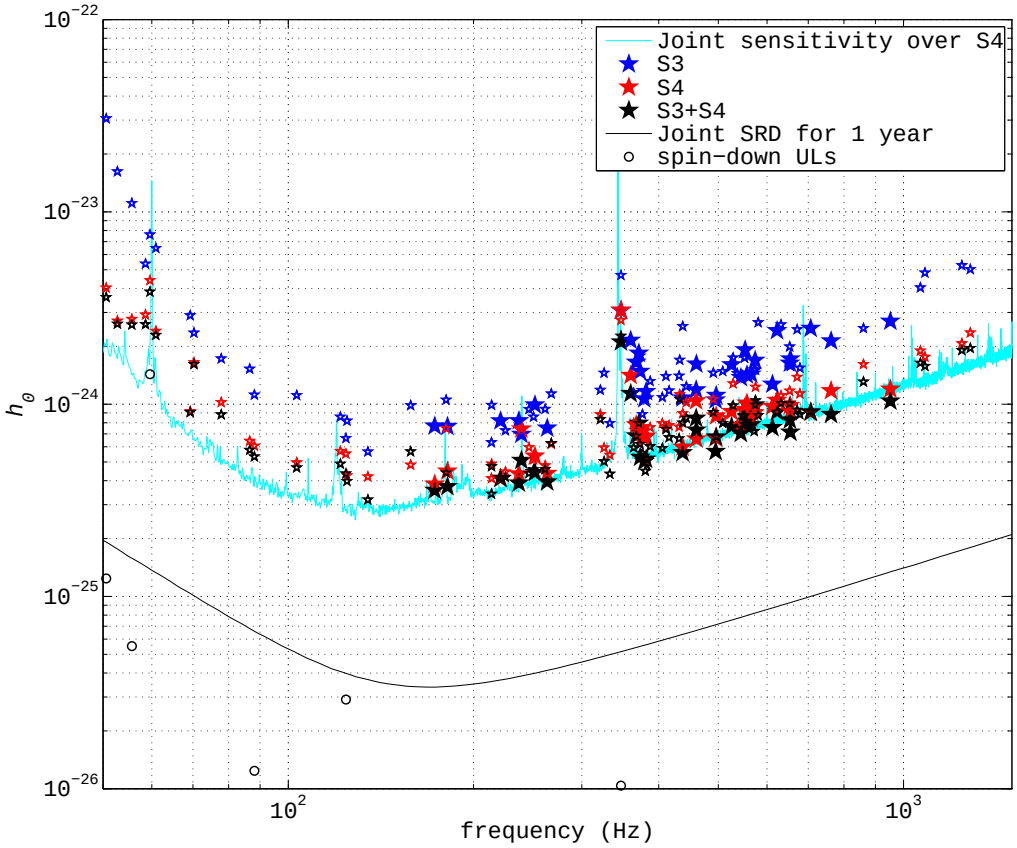

Figure 3.10: 95% upper limits on h_0 for 93 pulsars using the S3, S4 and combined data sets. Bold stars represent pulsars within globular clusters. Also shown is the joint LIGO upper limit estimated from their best noise spectral densities during S4. A joint upper limit estimate for LIGO using their design (SRD) sensitivities integrated over one year is shown. Several pulsar spin-down upper limits are also shown for those within the range of the figure.

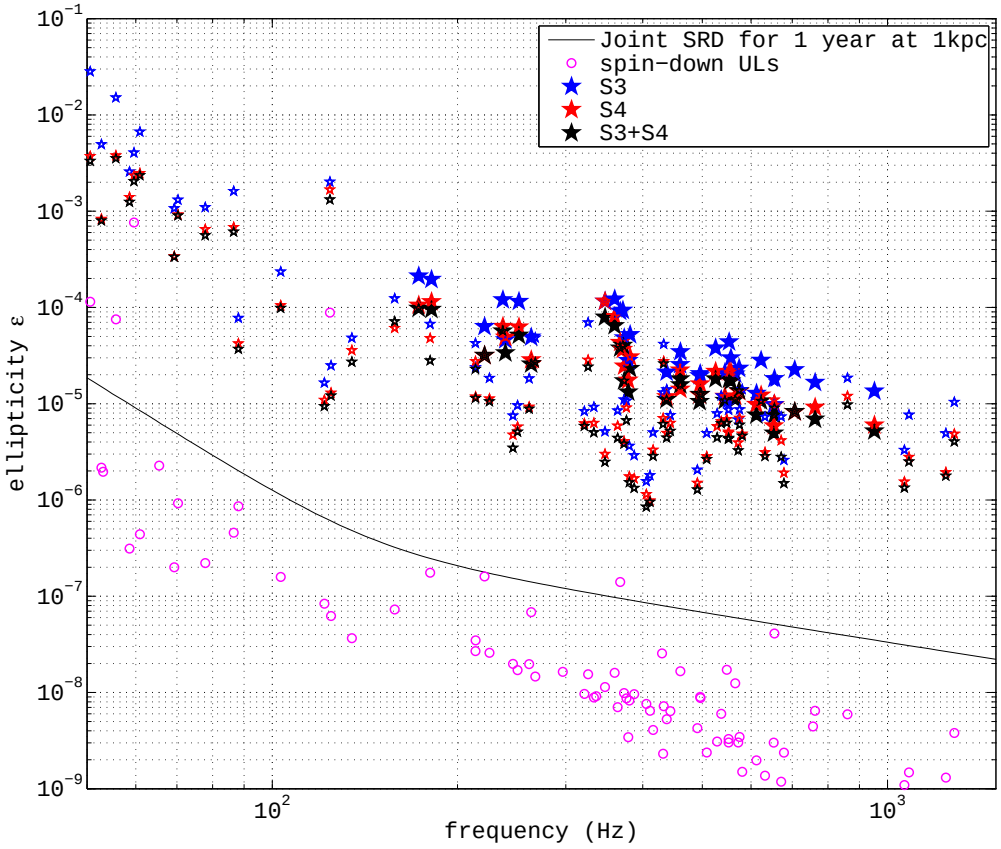

Figure 3.11: Upper limits on pulsar ellipticity for the S3, S4 and combined data sets. Bold stars represent pulsars within globular clusters. Also shown is the ellipticity limit that could be produced using the joint design sensitivity upper limit integrated over one year for a source at a distance of 1 kpc. The spin-down upper limits are also plotted.

the frequency range by combining the LIGO noise spectral density sensitivity curves, taken as the best sensitivity during S4. The estimate is made using the relation $h_0^{95\%} = 10.8\sqrt{S_h(f)/T_{\rm obs}}$, where $S_h(f)$ is the one-sided power spectral density (PSD) and $T_{\rm obs}$ is each detector's live time (using the associated duty cycle of each interferometer during the run). The factor 10.8, given in Dupuis and Woan (2005) [1], has been modified from the value of 15.3 calculated in [66] from simulations using white noise averaged over sky position, due to an error in the definition of the noise spectral density. The joint upper limit curve is produced by combining the detector PSDs via

$$\begin{aligned} S(f) &= \left(\frac{T_{\rm obs\ H1}}{S_h(f)_{\rm H1}} + \frac{T_{\rm obs\ H2}}{S_h(f)_{\rm H2}} + \frac{T_{\rm obs\ L1}}{S_h(f)_{\rm L1}}\right)^{-1} \\ h_0^{95\%} &= 10.8\sqrt{S(f)}. \end{aligned} \tag{3.13}$$

In [34] a similar plot to figure 3.10 is shown for the S2 data using a factor of 11.4 in the relation between the upper limit and PSD. This definition comes from using the $\mathcal{F}$-statistic search method and setting a 1% false alarm rate and 10% false dismissal rate for signals given the underlying detector PSD. It can be seen that the majority of the combined S3 and S4 upper limits are dominated by the S4 data, with a few for which the S4 data alone produces the more stringent upper limit. Combining the data set has pushed two of the ellipticity limits below the level of 10^{-6}. The implications of these results will be discussed in §3.5.

3.4.5 Moment of inertia - ellipticity plane

The moment of inertia of a neutron star will depend on the equation-of-state (EOS) used to model it. For all the above results on pulsar ellipticity a moment of inertia of $10^{38}\,\mathrm{kg\,m^2}$ has been assumed (see Chapter 2), which relies upon a particular equation-of-state being correct. It also assumes a neutron star mass of $1.4\,M_\odot$. For many known radio pulsars in binary systems, where the mass can be measured, this mass estimate appears to be remarkably well kept (see Thorsett and Chakrabarty, 1999 [100]). Recent measurements have reported two of the most massive pulsars known with Nice *et al.*

(2005) [101] giving the highest recorded pulsar mass at $2.1\,M_{\odot}$, although with wide error bars, and Ransom *et al.* (2005) [91] giving a mass of $1.68\,M_{\odot}$ at 95% confidence. There are many equations-of-state, some considered more realistic (using nucleons and leptons) and others considered less likely (involving more exotic particles or quark states), giving moments of inertia varying over factors of about two, with Thorne (1987) [12] giving a range for different EOS of $3\times10^{37}\,\mathrm{kg\,m^2} \lesssim I_{zz} \lesssim 3\times10^{38}\,\mathrm{kg\,m^2}$. The high mass neutron stars given above could possible have ellipticities towards the high end of this range. Attempts have been made by Bejger and Haensel (2002 and 2003) [102, 103] to set limits on the moment of inertia of the Crab pulsar by equating its spin-down energy loss to the expansion of the Crab nebula and its electromagnetic emission, which have been used to confine its mass and radius. More recently Bejger *et al.* (2005) [104] have set constraints on the moment of inertia of the neutron stars in the double pulsar binary system PSRs J0737-3039A and B giving values close to the canonical value.

As suggested in Pitkin *et al* (2005) [105] instead of using equation 3.4 to set a limit on ε directly it can be used to set a limit on the neutron star quadrupole moment $I\varepsilon$, which does not contain the mass and moment of inertia assumptions. The quadrupole moment can then be used to provide constraints on an $I-\varepsilon$ plane with exclusion regions. With this plane, an upper limit on ε can then be read off using your favoured equation-of-state. The spin-down upper limit can also be used to provide exclusion regions via the relation

$$I_{zz} = \frac{5|\dot{\Omega}|c^5}{32G\Omega^5}\frac{1}{\varepsilon^2}. \tag{3.14}$$

For most pulsars, forming an $I-\varepsilon$ plane will generally provide very little more information than the straight limit set with the canonical moment of inertia when compared to the spin-down limit. For the Crab pulsar and PSR J0537-6910, which are nearing their spin-down limits, it starts to become more interesting with the experimental values nearing the point where they beat the spin-down limit for moments of inertia from exotic equations-of-state[8]. In the following sections the results for these

[8]This is not to say that they are compatible with ellipticities obtainable with exotic EOSs which

two pulsars are discussed.

There are a couple of other constraints which can be placed on the $I - \varepsilon$ plane (see figure 3.12). The first constraint is that from the EOS. These provide limits on the possible mass and radius of neutron stars and can provide upper and lower limits on the range of moments of inertia. They will also constrain the maximum ellipticity that the neutron star could sustain, estimates of which for various neutron star equations of state are given by Owen (2005) [106]. For the Crab pulsar a lower limit can be placed on the moment of inertia by equating its loss in rotational energy with the energetics of the Crab nebula surrounding it (discussed below) [103].

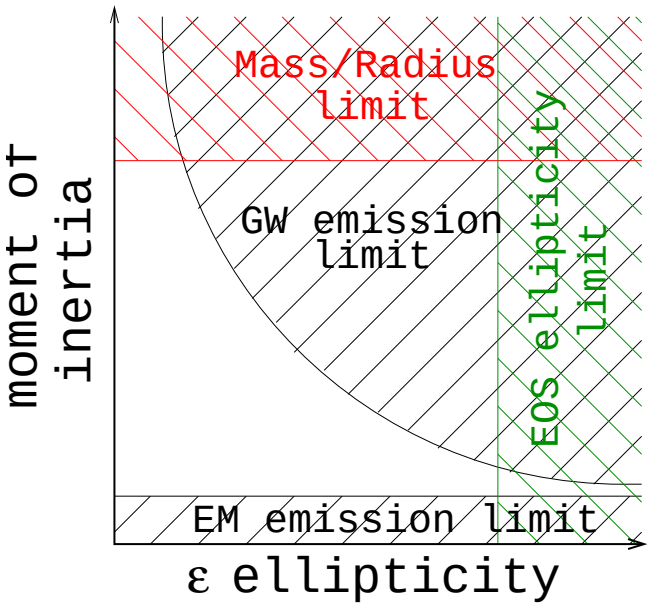

Figure 3.12: The regions in the moment of inertia I_{zz}-ε plane for a pulsar that can be excluded via various methods. The electromagnetic emission of a pulsar can set a lower limit on the moment of inertia by equating the EM emission with the rotational energy loss of the pulsar. The various equations-of-state for neutron stars can constrain the mass/radius relation and therefore moment of inertia [107]. Equations of state will also put limits on the maximum allowable ellipticity of the neutron star. A limit can be set from upper limits on gravitational wave emission.

3.4.6 The Crab pulsar

Of the known radio pulsars, the Crab pulsar has often been considered one of the most promising sources of gravitational waves. This is in part due to its youth and therefore large spin-down rate, leading to a relatively large spin-down upper limits orders of

are generally a few orders of magnitude smaller.

magnitude higher than for most other pulsars. The high rate of glitching in the pulsar also provides possible evidence of asymmetry. One glitch model, favoured for the Crab pulsar, is that there is a change in the pulsar ellipticity, and breaking of the crust, as the star settles to its new equilibrium state as it spins-down [75]. Back in the 1970s estimates of gravitational wave strains were spurred on by the experimenters producing novel technologies which could start the possibility of probing these low strains, with Zimmermann (1978) [108] producing estimates of gravitational wave strains from the Crab pulsar ranging from $2\times10^{-25} \lesssim h_0 \lesssim 2\times10^{-29}$.

The first searches for gravitational waves from the Crab pulsar were by the Japanese using specially designed resonant bar detectors, with frequencies of around 60 Hz [57]. The most recent result using such a bar was from 1993 and gave a 1σ upper limit of $h_0 \leq 2\times10^{-22}$ [58]. This upper limit has now been overtaken with the advent of the interferometric gravitational wave detectors, with results of the S2 run, giving $h_0^{95\%} = 4.1\times10^{-23}$ [34]. Using equation 2.3, and taking $I_{zz} = 10^{38}\,\mathrm{kg\,m^2}$ and $r = 2\,\mathrm{kpc}$, gives a spin-down upper limit for the Crab pulsar of $h_0 < 1.4\times10^{-24}$. This meant that for S2 the Crab pulsar results was still a factor of ~ 30 above the spin-down limit. This was still the closest result to the spin-down upper limit so far obtained and closest of any of the known pulsars searched for.

The Crab pulsar does require special attention. As described in Chapter 2 the effect of timing noise has to be taken into account. Also its gravitational wave frequency sits very close to 60 Hz, which is the mains AC frequency in the US, so checks need to be made that this line, as appearing in the detector spectra, does not interfere with the analysis. Figure 3.13 shows the spectra around the 60 Hz for the LIGO interferometers during a section of S3 and S4. It can be seen that the 60 Hz power line does not seem to interfere with the data at the Crab pulsar frequency of ~ 59.6 Hz.

The general results for the Crab pulsar can be seen with the others in tables 3.6, 3.8 and 3.10. It can be seen that the results improve by about an order of magnitude over those from the previous S2 run. The majority of this improvement was between the S2 and S3 runs, with there not being as big an improvement in the low frequencies

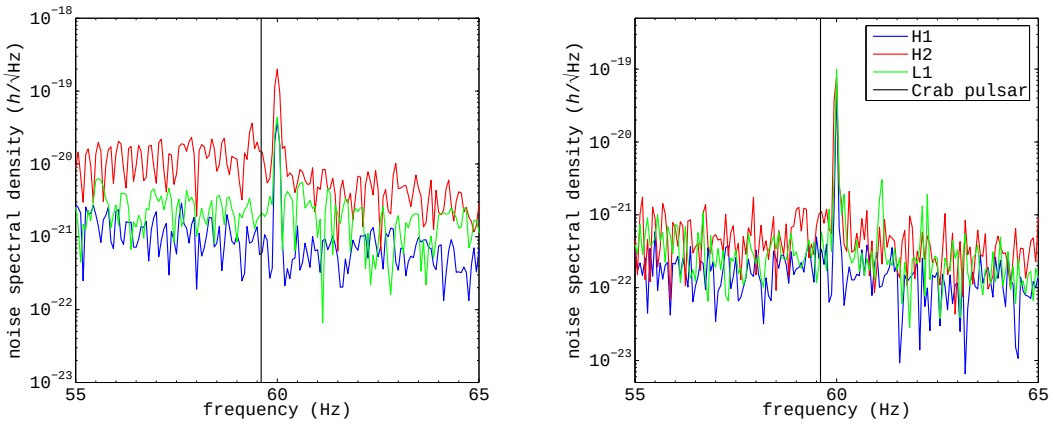

Figure 3.13: The LIGO noise spectral densities between 55 and 65 Hz for S3 (left) and S4 (right) showing the 60 Hz power line and Crab pulsar frequency.

between S3 and S4. The results for the Crab pulsar over the S2, S3 and S4 runs are plotted on the $I - \varepsilon$ plane in figure 3.14. It can be seen that over the range of

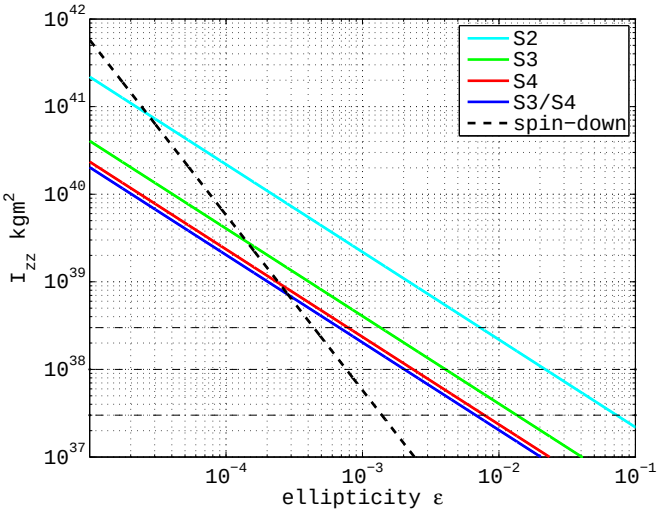

Figure 3.14: The moment of inertia-ellipticity plane for the Crab pulsar over the S2, S3 and S4 runs.

$3\times10^{37} < I_{zz} < 3\times10^{38}\,\mathrm{kg\,m^2}$, which covers moments of inertia from even some of the most exotic EOS, that the ratio of the spin-down upper limit to our results ranges from ~ 5 at the lower end to ~ 1.5 at the upper end. For the Crab pulsar the spin-down limit argument is rather spurious as it is known that at least some of the spin-down energy goes into the energetics of the Crab nebula. The fact that the braking index of the pulsar is not 3, but 2.51, shows that it is not spinning down purely through magnetic dipole radiation. In Palomba (2000) [49] several reasons for having $n \neq 3$

are mentioned, including particle acceleration in pulsar winds or non-dipole magnetic fields, but in particular there is discussion of the effects of gravitational radiation. If the spin-down were purely through emission of gravitational waves one would expect $n = 5$, so Palomba (2000) [49] tries combining all possible mechanisms of producing $n = 2.51$ to provide limits on the gravitational wave emission. This gives an upper limit of $\varepsilon \leq 3{\times}10^{-4}$, which is 2.5 times lower than the previous spin down limit (assuming all emission via gravitational waves) and therefore makes our result over six times greater than this new upper limit.

For these results we have assumed that the α parameter of Jones (2004) [70] has a value of 1, i.e. the gravitational wave and electromagnetic timing noise of the Crab pulsar are the same. As previously stated this seems to be a good assumption, although when our results start to beat the spin-down limit it could be worth including this as an extra parameter in the search.

3.4.7 PSR J0537-6910

Another interesting pulsar worth closer study is PSR J0537-6910. This pulsar, associated with the SNR N157B in the Large Magellanic Cloud (LMC), is currently only seen as an X-ray pulsar and is the fastest rotating young pulsar, with a rotation frequency of $\sim 62\,\mathrm{Hz}$ [50]. It is also one of the most prolific glitchers of the known pulsars, with a rate of 2.3 per year seen over the period of study in Marshall *et al.* (2004) [50] (with a number of observations using the *Rossi X-ray Timing Explorer* between 19$^{\mathrm{th}}$ January 1999 and 23$^{\mathrm{rd}}$ August 2001). Despite this high glitch rate Marshall *et al.* (2004) [50] were able to carry out phase-connected timing solutions between glitches and get measurements of $\ddot{\nu}$ and therefore the braking index n. The observed value of $n \geq 6.9$ is well away from the pure dipole radiation value of 3, although as stated in [50] there could be some contamination due to timing noise and uncertainties in the pulsars position and the $\ddot{\nu}$ value. We have not been able to obtain timing data for this pulsar over the periods of S3 and S4, so the high glitch rate and unknown timing noise mean these results should be accepted as possibly invalid. It also has potential problems with the

frequency parameter errors pushing its maximum phase error over our 30° limit. Its parameters taken from [50], and as used for the heterodyne procedure (at twice the frequency), are given in table 3.12.

Table 3.12: The parameter values for PSR J0537-6910.

PSR J0537-6910	
α	$05^{\mathrm{h}}37^{\mathrm{m}}47^{\mathrm{s}}.36$
δ	$-69°10'20''.4$
ν (Hz)	62.0261895958(13)
$\dot{\nu}$ (Hz s^{-1})	$-1.992720(4)\times10^{-10}$
$\ddot{\nu}$ (Hz s^{-2})	$6.1(3)\times10^{-21}$
Epoch (MJD)	52061.334068867

What makes this pulsar interesting are its similarities with the Crab pulsar. As it is young it has a relatively high spin-down rate (just under half that of the Crab). It also happens to be in the most sensitive part of the LIGO spectrum, which accounts for why its joint upper limit for S4 is so good. One disappointment is that, being an LMC object, it is relatively far away with $r \simeq 49.4\,\mathrm{kpc}$. These factors mean that this pulsar is the second closest, after the Crab pulsar, to its spin-down upper limit at only ~ 6 times the Crab pulsar value for the combined results. The results in terms of the $I - \varepsilon$ plane are shown in figure 3.15.

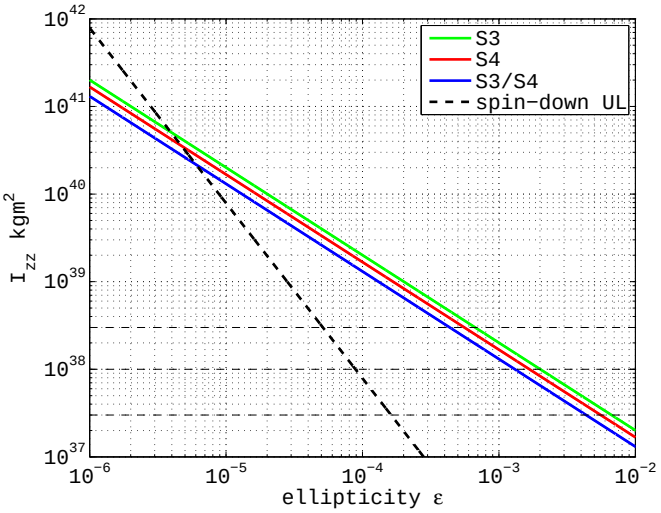

Figure 3.15: The moment of inertia-ellipticity plane for PSR J0537-6910 over the S2, S3 and S4 runs.

3.5 Astrophysical interpretation

It can be seen from tables 3.6, 3.8 and 3.10 that for the majority of pulsars the upper limits we have produced are at least a couple of orders of magnitude above those from the spin-down argument. If we were to take a pulsar for which our S4 upper limit was still 100 times above the spin-down limit, we would require an S4 sensitivity run of ~ 1000 years until we could match the spin-down limit. This being so is there anything that we can take from the results in terms of useful astrophysics?

The first thing we can say is that for many of the globular cluster pulsars for which there is a Doppler induced apparent spin-up we are providing the only limits independent of the pulsars' motion within the cluster. The maximum apparent spin-up induced by acceleration in a globular cluster is $4.7\times10^{-13}\,\mathrm{Hz\,s^{-1}}$ for PSR J2129+1210D in the cluster M15 [90]. This large apparent spin-up is due to the pulsar being close to the centre of the cluster and thus being subject to the largest accelerations. Given this value we can speculate that this is the sort of magnitude of frequency derivative that could be masked by acceleration effects and therefore use $-4.7\times10^{-13}\,\mathrm{Hz\,s^{-1}}$ as a maximum *spin-down* for all our globular cluster pulsars. This has not been used here, but may be useful in providing a spin-down upper limit in the future.

It is also interesting to note, despite our limits on the known pulsars being high in relation to the spin-down ones, that our ellipticity limits are well into the range permitted by at some models of strange quark stars or hybrid stars ($\varepsilon \sim$ a few times $10^{-4} - 10^{-5}$) and are reaching into the range permitted by more conventional neutron star EOSs ($\varepsilon \sim$ a few times 10^{-7}) [106].

Currently the fifth LSC science run (S5) is underway with this providing the possibility of beating the Crab pulsar spin-down limit within a few months. In reality we will need to be a few times better than the straight spin-down limit before we can say we are into an interesting regime. This is because we know that some energy is being lost through magnetic breaking and powering the nebula, and if we take Palomba's argument stated above we need to be at least 2.5 times better than spin-down. Again this is assuming our canonical moment of inertia, and some of this may be clawed back

if the Crab pulsar is in the higher mass range.

Facts are meaningless. You could use facts to prove anything that's even remotely true!

Homer Simpson - The Simpsons

Chapter 4

Neutron star quasi-normal mode searches

In this chapter we will describe the possible emission of gravitational wave ring-down signals from neutron stars during glitches. We then describe two search techniques; one using matched-filtering and the other using Bayesian evidence (sometimes called the marginal likelihood). These techniques are them applied to search for a ring-down signal from the magnetar SGR 1806-20 during a GRB on 27^{th} December 2004.

4.1 Neutron stars as burst sources

As well as being potential sources of continuous gravitational waves, under certain conditions neutron stars may also provide a good source of burst-like transient events. Such bursts could come from the birth of the neutron star in a supernova, where the violence of the event excites various vibrational modes of the hot young proto-neutron star (PNS) [109]. At present there have been no searches to specifically target vibrational mode signals from PNSs, although such signals could possibly come under the remit of more generic burst source searches. Neutron stars in binary systems will emit a transient chirp signal during the final stages of the binary inspiral as they coalesce. These are some of the most promising gravitational wave sources as the

extreme energetics of the event can produce very large amplitude waves that can be seen over great distances. Searches for such signals have been carried out using data from the LIGO detectors (see Abbott *et al.*, 2004b [40]). For the current LIGO sensitivity such binary inspiral signals (for two $1.4\,M_{\odot}$ neutron stars) will be observable out to a distance of $\lesssim 15\,\mathrm{Mpc}$.

There is another possible mechanism which could induce a burst of gravitational waves from a neutron star. Quasi-normal mode oscillations could be set up during a neutron star glitch leading to a gravitational wave ring-down signal (see Kokkotas *et al.*, 2001 and Kokkotas and Schmidt, 1999 [110, 111]). The most promising of these vibrational modes for detection using current gravitational wave detectors are the fundamental fluid modes (f-modes) due to their frequencies being between $\sim 1.5 - 4\,\mathrm{kHz}$ [27] and therefore within the frequency range of detectors. The nature of this signal is closely related to the structure of the star and could provide a direct probe of the equation-of-state, making such signals an exciting prospect for detection and opening up neutron star asteroseismology.

4.1.1 Neutron star glitches

A pulsar glitch is seen as an irregularity in its timing whereby there is a step increase in its frequency followed by an exponential recovery back to the pre-glitch level (see Lyne and Graham-Smith, 1998 [75] for more details). These were first seen in the Vela pulsar. The step changes in frequency cover a range of magnitudes from $\Delta\nu/\nu \sim 10^{-9}$ to $\sim 10^{-6}$. Glitches have so far been observed in 45 pulsars (as given in the ATNF pulsar catalogue [47] at the time of writing). The majority of these have only been observed to glitch once, although sparseness of observations leads to some uncertainty in the actual number of glitches. A few are quite prolific glitchers, with PSR J0835-4510 (the Vela pulsar) and PSR J1740-3015 both having been seen to glitch the maximum observed number of 14 times. Two other prolific glitchers are the young pulsars discussed in Chapter 3: the Crab pulsar and PSR J0537-6910.

The cause of pulsar glitches is still unknown, but two main theories have been

postulated. The first involves an adjustment in the pulsar ellipticity/moment of inertia. This occurs when the crust of the pulsar reaches breaking strain as it spins-down and the centrifugal force reduces and therefore has to adjust to a new equilibrium [75] i.e. starquakes. This possibility seems to be the most likely cause of the glitches seen in the Crab pulsar. The second possibility involves a transfer of angular momentum between the stars crust and superfluid interior when the two dramatically uncouple [75].

4.1.2 The ring-down signal

A ring-down signal will have the form

$$y(t) = \begin{cases} A\sin\left[2\pi f(t-T_0)+\phi_0\right]e^{-(t-T_0)/\tau} & \text{for } t \geq T_0, \\ 0 & \text{for } t < T_0 \end{cases} \tag{4.1}$$

where A is the initial amplitude, ϕ_0 is the initial phase, τ is the decay constant and T_0 is the signal arrival time. The frequency of such signals can be calculated from the characteristic timescale of the dynamical process involved, which is related to the mean density of mass involved giving $f \sim \sqrt{\bar{\rho}}$. The ring-down timescale can be estimated using the ratio of the oscillation energy to the power emitted in gravitational waves, giving $\tau \sim R(R/M)^3$. In Andersson and Kokkotas (1998) [27] these are used to calculate the ring-down frequency f and damping time τ for the f-modes using various neutron star EOSs, the empirical fits to which are are given in [27] by

$$f(\text{kHz}) \approx 0.78 + 1.635\left[\frac{(M/1.4\,\text{M}_\odot)}{(R/10\,\text{km})^3}\right]^{1/2}, \tag{4.2}$$

and

$$\frac{1}{\tau(\text{s})} \approx \frac{(M/1.4\,\text{M}_\odot)^3}{(R/10\,\text{km})^4}\left\{22.85 - 14.65\left[\frac{(M/1.4\,\text{M}_\odot)}{(R/10\,\text{km})}\right]\right\}. \tag{4.3}$$

These relations show how important information on the neutron star mass/radius relation (and therefore EOS) could be extracted from the detection of a ring-down signal, with such observations possibly providing a unique measurement.

The amount of energy released in a glitch can be inferred by the fractional change in

frequency. From Andersson and Kokkotas (1998) [27] the effective achievable amplitude of gravitational wave searches, assuming a matched filtering search strategy, for the f-mode is given by

$$h_{\rm eff} \sim 2.2\times10^{-21}\left(\frac{E}{10^{-6}{\rm M}_\odot c^2}\right)^{1/2}\left(\frac{2\,{\rm kHz}}{f}\right)^{1/2}\left(\frac{50\,{\rm kpc}}{r}\right), \tag{4.4}$$

where $h_{\rm eff} = h\sqrt{f\tau}$, from the effective amplitude scaling as the square root of the observed number of cycles [111], and E is the available pulsation energy liberated via whichever mechanism excited the star. For a newly formed neutron star in a supernova explosion the amount of energy released in gravitational waves has been estimated (via simulations) to be within the range $10^{-4} - 10^{-7}\,{\rm M}_\odot c^2$ giving a range of $h_{\rm eff} \sim 10^{-19} - 10^{-22}$ [111] (assuming all energy goes into f-modes and using the fiducial frequency and distance). For the two different glitch models the amount of energy released can be estimated in different ways as shown in van Riper *et al.* (1991) [112]. For the angular momentum exchange model (thought to be the most probable explanation for the Vela pulsar glitches) the amount of energy released depends on the angular momentum exchanged between the superfluid interior and crust $\Delta J \sim I\Delta\Omega$, where $\Delta\Omega$ is the angular frequency change from the glitch. The energy change is then $\Delta E = \Delta J\Omega_{\rm lag}$, where $\Omega_{\rm lag}$ is the lag frequency between the superfluid and crust, with a range of values of 1-100 rad s^{-1} (or possibly $\lesssim 0.1\,{\rm rad\,s^{-1}}$) [112]. For the largest Vela pulsar glitch, with a fractional frequency change of $\Delta\Omega/\Omega = 3.1\times10^{-6}$ [113], this gives a $\Delta J \sim 2\times10^{34}$ J giving an energy release of $\Delta E \sim 2\times10^{34} - 2\times10^{36}$ J $\approx 10^{-13} - 10^{-11}\,{\rm M}_\odot c^2$. Using these value in equation 4.4, with $r = 0.29$ kpc gives a value of $h_{\rm eff} \sim 10^{-22} - 10^{-21}$, assuming all energy loss goes into gravitational waves. In [112] the energy is assumed to go into heating the star rather than gravitational wave emission, but even if a few percent goes into f-modes this could still be a considerable gravitational wave amplitude.

For starquake driven glitches the energy released is given in van Riper *et al.* [112] as $\Delta E \approx \mu V_{\rm crust}\epsilon_{\rm max}\epsilon_{\rm quake}$, where $\epsilon_{\rm quake} = \Delta\Omega/\Omega$ is equivalent to the relative change in moment of inertia, μ is the mean shear modulus of the star, $V_{\rm crust}$ is the volume of the

crust (where $\mu V_{\rm crust} \sim 10^{41}$ J), and $\epsilon_{\rm max}$ is the maximum deformation from equilibrium the crust can withstand without breaking (given in [112] as $\epsilon_{\rm max} \lesssim 10^{-2}$ although this could vary somewhat). Assuming this $\epsilon_{\rm max}$ and taking the largest Crab pulsar glitch, where $\Delta\Omega/\Omega \sim 8\times10^{-8}$ [71], we get an energy release of $\Delta E \sim 8\times10^{31}$ J, which is a couple of orders of magnitude less than for the Vela pulsar glitches, and will therefore probably not be as good a gravitational wave source. If the starquake mechanism can provide similar fractional frequency changes to a neutron star to those seen in the Vela pulsar during glitches, then this mechanism could still be a valuable potential source.

4.2 Search methods

4.2.1 Matched filtering

Matched filtering methods can be used in searches where the shape of the signal is well defined by theory. This is not the case for generic burst searches where the signal shape is unknown, but is the case for the binary inspiral search (up to the point at which theoretical models and simulations break down), and for ring-down signals as in equation 4.1. Matched filtering is a method of correlating the detector output with a filter (or template) produced for a set of parameter values. Given a detector output $d(t) = As(t) + n(t)$, where A is the signal amplitude, $s(t)$ the signal shape normalised such that $\langle s|s\rangle = 1$ and $n(t)$ is the noise, and a filter $h(t)$, then the matched filter will be their inner product

$$\begin{aligned} \langle d|h\rangle &= 2\int_0^\infty \frac{\tilde{d}^*(f)\tilde{h}(f) + \tilde{d}(f)\tilde{h}^*(f)}{S_n(f)}\mathrm{d}f, \\ &= 4\Re\left[\int_0^\infty \frac{\tilde{d}^*(f)\tilde{h}(f)}{S_n(f)}\mathrm{d}f\right], \end{aligned} \tag{4.5}$$

where $\tilde{d}(f)$ is the Fourier transform $\tilde{d}(f) = \int_{-\infty}^{\infty} d(t)e^{i2\pi ft}\mathrm{d}t$ and $S_n(f)$ is the detector one sided noise power spectral density (see Owen, 1996 [114] for a more complete description). The matched filter time series output, for a given filter, will be the inverse Fourier transform of this (see Abbott *et al.*, 2004b [40] for an application of

this to inspiral searches), giving a real time series

$$x(t) = 4\Re\left[\int_0^\infty \frac{\tilde{d}^*(f)\tilde{h}(f)}{S_n(f)} e^{2\pi i f t} \mathrm{d}f\right]. \tag{4.6}$$

The signal-to-noise ratio S/N of this output is then given by $\rho(t) = |x(t)|/\sigma$, where

$$\sigma^2 = 4\int_0^\infty \frac{|\tilde{h}(f)|^2}{S_n(f)} \mathrm{d}f \tag{4.7}$$

is the filter variance. For a template exactly matching a signal present in the data the filtering will be optimal in the sense that the expectation value of $\langle d|h\rangle$ $(=S/N)$ will provide the signal amplitude A exactly. If the template does not match the filter it will be non-optimal and the expectation value will be mis-matched from A by a factor of $\langle s|h\rangle$.

Template bank generation

In a search for a signal in noise we clearly want to use the optimal filter i.e. the one which most closely matches the signal shape. A continuous template bank will be computationally impossible, but we still need enough templates to ensure that the mis-match between adjacent templates will not seriously decrease the effectiveness of the search. Following [114], we see that given a vector of intrinsic signal parameters $\boldsymbol{\lambda}$, the match between two templates with parameters $\boldsymbol{\lambda}$ and $\boldsymbol{\lambda} + \Delta\boldsymbol{\lambda}$ is defined as

$$M(\boldsymbol{\lambda}, \Delta\boldsymbol{\lambda}) = \langle h(\boldsymbol{\lambda})|h(\boldsymbol{\lambda} + \Delta\boldsymbol{\lambda})\rangle. \tag{4.8}$$

Expanding this as a power series to second order in $\Delta\boldsymbol{\lambda}$ about $\Delta\boldsymbol{\lambda} = 0$ leads to the metric interpretation of the mis-match between templates

$$1 - M = g_{ij}\Delta\lambda^i\Delta\lambda^j, \tag{4.9}$$

where the metric g_{ij} is defined as

$$g_{ij}(\boldsymbol{\lambda}) = -\frac{1}{2}\left(\frac{\partial^2 M}{\partial\Delta\lambda^i\partial\Delta\lambda^j}\right)_{\Delta\lambda^k=0}. \tag{4.10}$$

This is the square of the proper distance between two templates $\mathrm{d}s^2$. Substituting the decay constant τ with the ring-down quality factor $Q = \tau\pi f$ we have $\boldsymbol{\lambda} = \{f, Q\}$ giving mis-match (from the LALapps ring-down code documentation [115]) of

$$\mathrm{d}s^2 = \frac{1}{8}\left[\frac{3+16Q^4}{Q^2(1+4Q^2)^2}\mathrm{d}Q^2 - 2\frac{3+4Q^2}{fQ(1+4Q^2)}\mathrm{d}Q\mathrm{d}f + \frac{3+8Q^2}{f^2}\mathrm{d}f^2\right] \tag{4.11}$$

Equation 4.11 can be used to place templates in our parameter space for a given value of the mismatch. From [114], assuming closely spaced templates in an N-dimensional hypercube we get

$$\mathrm{d}s^2 = g_{ij}\Delta\lambda^i\Delta\lambda^j = N(\mathrm{d}\ell/2)^2, \tag{4.12}$$

where the proper length $\mathrm{d}\ell$ forms the sides of the hypercube. If we work in terms of $\log f$, the metric g_{ij} only depends on Q, making the number of dimensions in parameter space $N = 1$. For a range of Qs starting at Q_{min} templates can be placed at intervals of $\mathrm{d}\log f = \mathrm{d}\phi = \mathrm{d}\ell/\sqrt{g_{\phi\phi}}$ across the range of ϕ. The value of Q can then be incremented by $\mathrm{d}Q = \mathrm{d}\ell/\sqrt{g_{QQ}}$ and the placement of templates in ϕ repeated. This can be seen in figure 4.1 where each point represents a template. It can been seen that the coverage of the Q range can be quite coarse while that for f is quite fine meaning that there will still be a quite fine coverage of τ.

There is obviously a trade-off between the number of templates used (which will increase for smaller mis-matches and larger parameter ranges) and the speed of the search, so the value of the mis-match needs to be chosen with this in mind.

Code to perform a ring-down search using matched filtering with a template bank as described above has been developed in LALapps [83] in the main by Jolien Creighton. This search was initially intended to look for black hole ring-downs after mergers as in

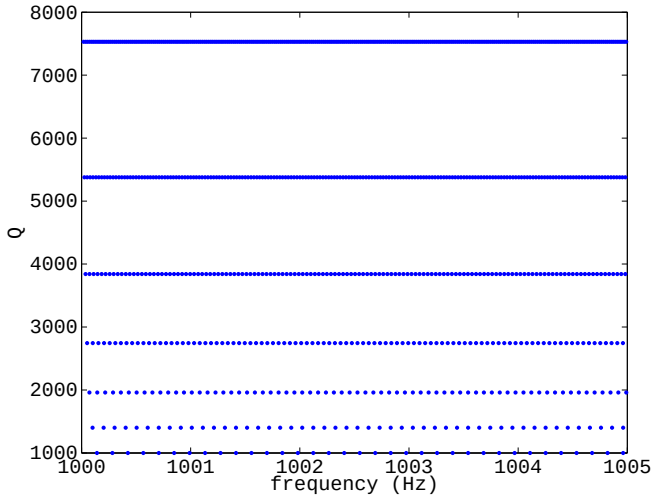

Figure 4.1: Template bank for our ring-down parameters over the range $f(\mathrm{Hz}) = [1000, 1005]$ and $Q = [1000, 10000]$ with a mismatch of 1%.

Creighton (1999) [25], where the values of Q and f can be used to imply parameters of the black hole. The simple ring-down template also applies to our case of neutron star ring-downs, so we are able to make use of the code for these purposes.

4.2.2 Bayesian evidence based search

Bretthorst (1988) [3] looks into the problem of parameter estimation for ring-down signals in noise, with the frequency and decay time being the parameters of interest. He derives a joint posterior probability distribution for the ring-down frequency and decay time of

$$p(f,\tau|D,I) \propto \left[1 - \frac{R(f,\tau)^2 + I(f,\tau)^2}{Nc\bar{d}^2}\right]^{\frac{2-N}{N}}, \tag{4.13}$$

where

$$R(f,\tau) = \sum_{i=1}^{N} d_i \cos(2\pi f t_i) e^{-t_i/\tau}, \tag{4.14}$$

$$I(f,\tau) = \sum_{i=1}^{N} d_i \sin(2\pi f t_i) e^{-t_i/\tau}, \tag{4.15}$$

$$c \approx \frac{1}{2}\sum_{i=1}^{N} e^{-2t_i/\tau}, \tag{4.16}$$

and

$$\bar{d^2} = \frac{\sum_{i=1}^{N} d_i^2}{N}, \tag{4.17}$$

where d_i are the data points. The ring-down amplitude and phase (see equation 4.1) have been analytically marginalised over using uniform priors, as has the unknown noise standard deviation (using a Jeffreys prior) in a similar way to that described in Chapter 2 for the pulsar parameter estimation, leaving a Student's-t-like distribution. This posterior only holds under the assumptions of no low frequency components in the data, i.e. $t \gg 1/f$ (as approximations are made in averaging sinusoids to zero) and that there is a large data set, $N \gg 1$. The use of this as a parameter estimation tool can be seen in figure 4.2, where a ring-down signal has been injected into noise and the posterior pdf extracted using the above method. A comparison of this method

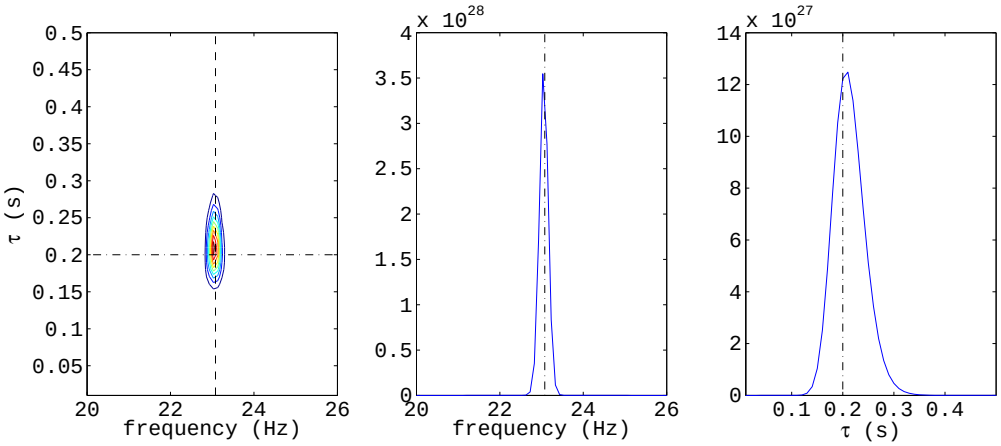

Figure 4.2: The posterior pdfs for the ring-down parameters f and τ. The dotted black lines represents the true signal parameters. The left-hand plot shows the joint pdf with probability contours. The other two plots show marginalised pdfs for each parameter.

for parameter estimation of ring-down frequencies with that of more classical Fourier power spectrum and periodogram analyses is given in [3] and can be seen in figure 4.3. Figure 4.3 shows how the Bayesian estimation technique can be far superior in pinning down the parameter value over more traditional methods.

This parameter estimation can be extended into a potential search for ring-down signals in which the parameter values are not considered important but the evidence of any signal being present is wanted. By marginalising over the range of the frequency

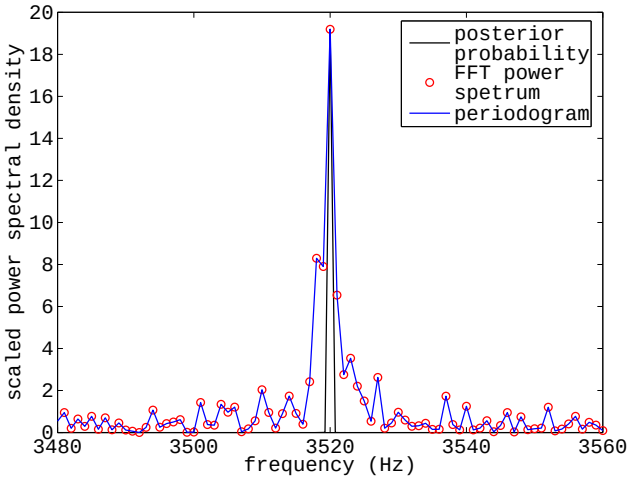

Figure 4.3: A comparison of the posterior pdf from equation 4.13 marginalised over τ, and the periodogram and power spectrum for a ring-down signal (with amplitude = 1, $f = 3519.9\,\mathrm{Hz}$ and $\tau = 0.11\,\mathrm{s}$) injected into Gaussian noise with $\sigma = 1$.

and decay time parameters a single value is obtained called the evidence,

$$\text{evidence} = \int_{f_{\min}}^{f_{\max}} \int_{\tau_{\min}}^{\tau_{\max}} p(f,\tau|I)p(D|f,\tau,I)\mathrm{d}f\mathrm{d}\tau, \tag{4.18}$$

which tells us something about the presence or absence of any ring-down signals in the given range. To evaluate its efficacy some comparison is needed between the value of the evidence when only noise is present to that when a ring-down signal is present.

To get an idea of how this algorithm performs when a signal is not present we have performed extensive simulations on 1000 realisations of Gaussian noise. This used a uniformly placed 4001×21 grid in $f(\mathrm{Hz}) = [1000, 4000]$ and $\tau(s) = [0.05, 0.5]$ to evaluate the posterior and perform the marginalisation, where the grid size was chosen as the best compromise between computational speed and parameter extraction accuracy from many trial grids. A plot of the evidence values obtained can be seen in figure 4.4. This has a mean value of $\log \text{evidence} = 5.97$ and shows $\log$ evidence values extending to ~ 8.5.

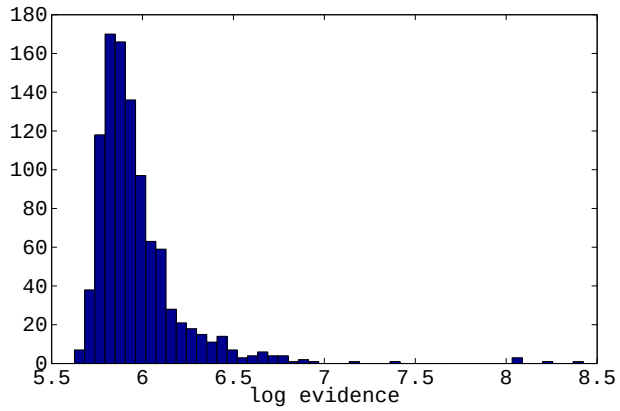

Figure 4.4: Evidence of a ring-down signal in 1000 independently realised one second (sampled at 16384 Hz) sets of Gaussian noise.

4.3 Ring-down search from 27th December 2004 γ-ray burst of SGR 1806-20

4.3.1 Soft γ-ray Repeaters

Soft γ-ray repeaters (SGRs) are seen as sources of short, extremely high luminosity bursts of soft spectrum γ-rays. Their periods of burst activity can be sporadic with extremely active periods followed by lengthy quiet periods. SGRs are also seen as quiescent soft X-ray sources. There are currently four (possibly five) SGRs known, a review of which can be found in Hurley (2000) [116]. The collocation of SGRs with supernova remnants has lead to the hypothesis that they are a class of very highly magnetised neutron stars called magnetars. Such stars have dipole magnetic fields of $B \sim 10^{14}-10^{15}$ G (cf. $\sim 10^{12}$ G for normal pulsars and $\sim 10^{8}$ G for millisecond pulsars), which means they will quickly spin-down via magnetic breaking.

SGRs are occasionally seen to emit giant flares of γ-rays, with thousands of times the luminosity of ordinary bursts and with harder spectra. The identification of these short duration ($\sim$ 0.2 second) γ-ray bursts (GRBs) with SGRs provides a possible source of some classical GRBs without any known counterpart. The cause of such giant bursts is discussed in Hurley *et al.* (2005) [117] and is thought to be a result of some extreme instability in the magnetar involving crustal breaking and magnetic

reconnection, with huge amounts of energy coming from the untwisting of the magnetosphere. Such reconfigurations of the crust and magnetic field could set up oscillations in the star (see Ioka, 2001 [118] and Kokkotas and Schmidt, 1999 [111]) which will be damped by emission of gravitational waves. This makes giant flares from SGRs a potential target for our ring-down search. Various methods of energy release to power the flares and possible gravitational wave emission are discussed in Horvath (2005) [119].

On 27th December 2004 the most luminous SGR flare yet seen was observed from SGR 1806-20 [117]. It was observed by five separate space-based γ-ray detectors and such was its intensity that it briefly saturated them all. The flare lasted ~ 380 seconds with an initial 0.2 second spike. The event information is shown in table 4.1. Although

Table 4.1: The parameters of SGR 1806-20 and the giant flare.

SGR 1806-20	
α	$15^{\mathrm{h}}56^{\mathrm{m}}37^{\mathrm{s}}$
δ	$-20°13'50"$
Distance	~ 15 kpc
Burst time	21:30:27 UTC 27-Dec-2004
Burst duration	200 ms

the time of this burst was outside of any LSC science run period, both the LIGO H1 detector and GEO 600 were taking data at the time. This gives the interesting possibility of performing a targeted search for gravitational waves from this source.

A search for gravitational waves from quasi-normal modes of this source has already been performed using data from the AURIGA bar detector (see Baggio *et al.*, 2005 [4]). It had a limited bandwidth of ~ 100 Hz around their detectors most sensitive frequency of 900 Hz (below the expected f-mode frequency range). This search performed a time convolution of the data with the ring-down signal model for 10 s around the peak of the burst over a range of f values spaced at $\Delta f = 1/(2\tau) = 5$ Hz, where $\tau = 100$ ms, and with time steps $\Delta t = 201.5$ ms. This method did not make use of optimal matched filtering. This gave an upper limit across the frequency range on the total gravitational wave energy of around $10^{-5}\,\mathrm{M}_{\odot}c^2$.

We can obtain an upper limit estimate on the gravitational wave amplitude from

this burst using the equations in §4.1.2. In Woods *et al.* (2005) [120] an upper limit on the change in frequency of SGR 1806-20 during the GRB is given as $\Delta f < 2\times10^{-5}$ Hz. Taking this value and assuming the model of angular momentum exchange between interior and crust we can get an upper limit on the energy release of $\Delta E < 10^{34} - 10^{36}$ J (for the range of $\Omega_{\rm lag}$), which is very similar to that for large glitches of the Vela pulsar. With a distance to SGR 1806-20 of $\sim$ 15 kpc, and again assuming all the energy goes into exciting f-modes and using equation 4.4 we get an upper limit range of $h_{\rm eff} < 10^{-23} - 10^{-24}$. From the discussion in [117] breaking of the crust, and therefore a change in the moment of inertia, seems a more likely mechanism of energy release to set up stellar oscillations. With a period of 7.48 s an upper limit on the relative change in moment of inertia can be calculated giving an energy release of $\Delta E < 10^{35}$ J and a gravitational wave amplitude upper limit on $h_{\rm eff} < 5\times10^{-24}$. These energies are still orders of magnitude less than that given off in γ-rays at the peak of the flare with $E \approx 3.5\times10^{39}$ J [117]. The energy for which can be explained by the release of energy stored in the twisted magnetic field ($E_{\rm twist} \sim 10^{39}$ J) via magnetic reconnection.

4.3.2 A preliminary search

First look

The first thing we did upon receiving information about the 27th December 2004 GRB was to look by eye at the data for any obvious signal. The data from 20 s around the time of the burst, high-pass filtered at 900 Hz, are shown as a time series in figure 4.5 and a spectrogram in figure 4.6. No obvious glitch is seen in this data above the level of the noise floor.

Szabolcs Marka and Peter Kalmus [121] have also been looking at this data for a possible low frequency burst, but for our quasi-normal mode search the low frequencies have been filtered out. In the low frequency region the GEO 600 data does not really help as its sensitivity below $\sim$ 1000 Hz is much worse than H1.

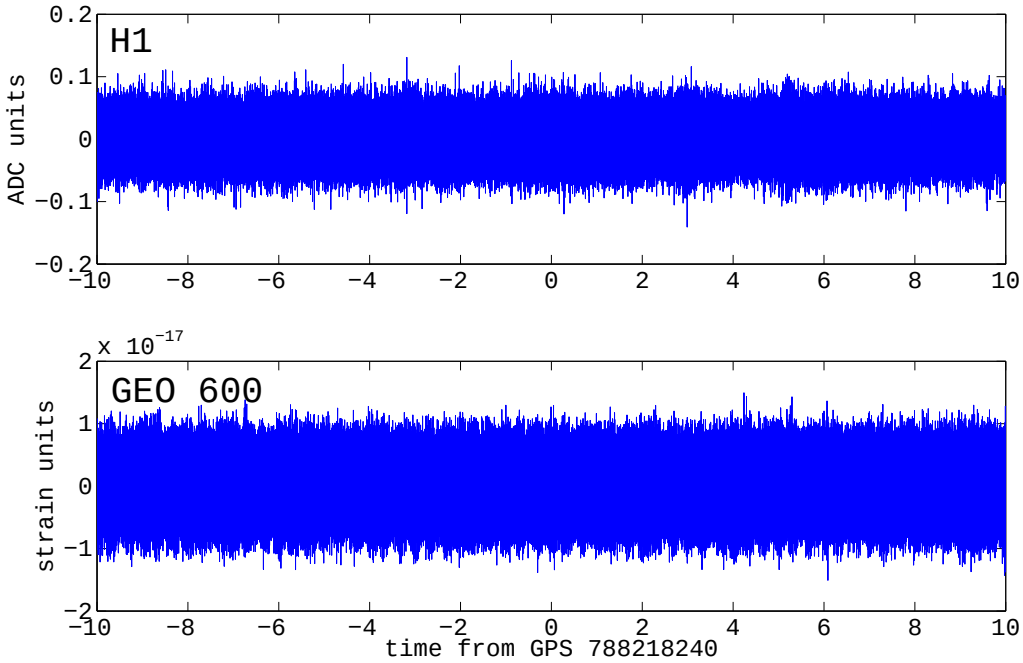

Figure 4.5: The time series of data from H1 and Geo 600 for 20 seconds around the time of the 27th December 2004 GRB. The data has been high-pass filtered at 900 Hz with an 8th order Butterworth filter.

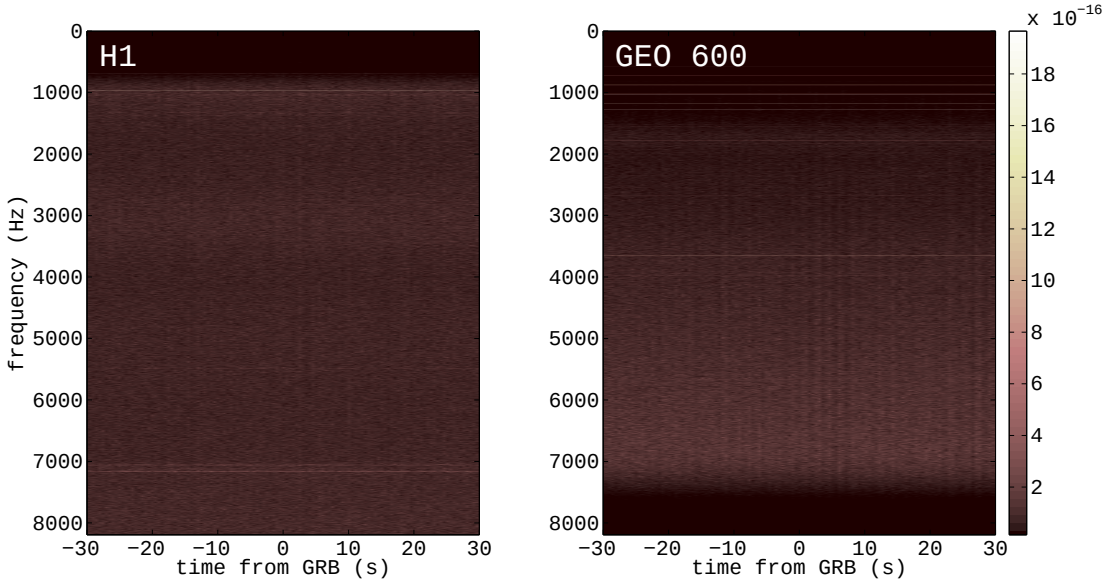

Figure 4.6: The spectrogram of data from H1 and Geo 600 for 60 seconds around the time of the 27th December 2004 GRB. The data has been high-pass filtered at 900 Hz with an 8th order Butterworth filter and the strength of the Geo 600 calibration lines has been suppressed for contrast.

Matched filter search

After the initial examination of the data we have made use of the LALapps ring-down code (as described in §4.2.1) to search for signals in the data at the time of the GRB. This work was performed with the help of an undergraduate summer student Edward Bloomer as part of a *Robert Cormack Bequest Scholarship*. The ring-down code takes in several parameters to perform the search which have been chosen with our particular targets in mind. These were: $f(\mathrm{Hz}) = [1000, 4000]$, $Q = [1000, 10\,000]$, $\phi_0 = 0$, high-pass frequency = 800 Hz, and a maximum template mismatch of 10%. This produces a template bank of 26 023 filters spaced as is shown in figure 4.7. The code will then

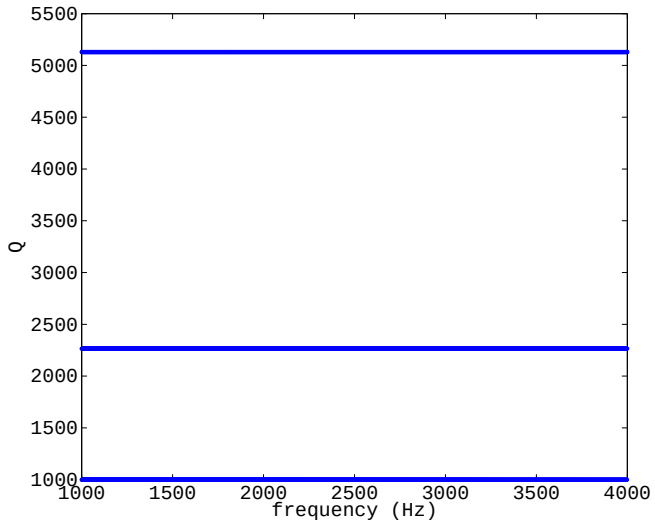

Figure 4.7: The template bank for the ring-down search with $f(\mathrm{Hz}) = [1000, 4000]$, $Q = [1000, 10\,000]$, and a maximum mismatch of 10%.

output triggers if any of the templates match the data above a certain S/N threshold. The level of this threshold needs to be set carefully as even Gaussian noise will give a underlying level of template matching. To determine the threshold to use for our data around the time of the GRB, we ran the code on simulated data and data from periods off-source, giving us a background level. Running the code over 120 seconds of simulated Gaussian noise (using the low S/N threshold of 1), gives us an idea of the background distribution of events picked up by the matched filtering (see figure 4.8). It can be seen from figure 4.8 that there is a clustering of events around an S/N of 3,

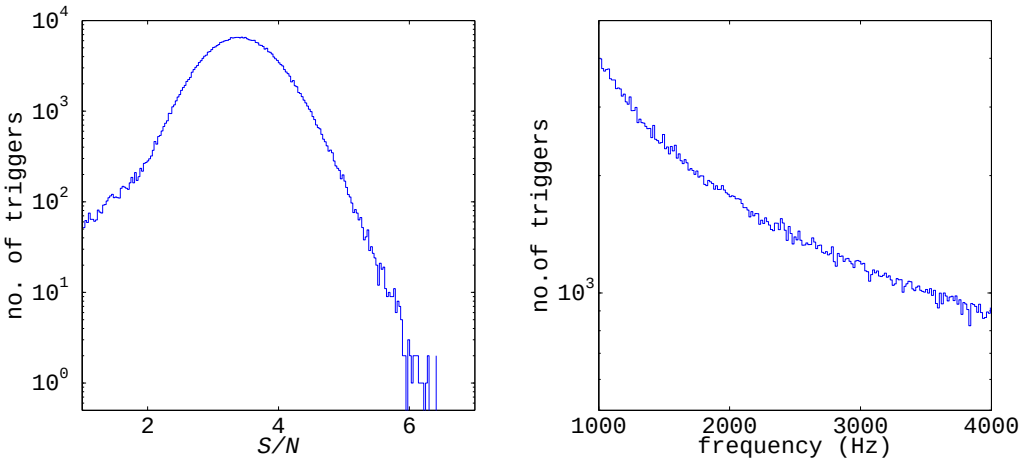

Figure 4.8: The number of triggers at given S/N and frequency for the LALapps ring-down code using 120 seconds of Gaussian noise.

with a tail extending out to ~ 7. This shows that even in completely Gaussian noise the code gives a background of events and a threshold of $S/N > 7$ is probably needed unless the events can be vetoed in some other way.

Simulated white noise does not necessarily reflect the true nature of our data which can contain many artifacts, either continuous, like instrumental lines, or transient in nature. The same search was therefore performed (using the parameters given above for the simulated noise) on 120 s of data approximately half an hour after the GRB. Here the threshold has been increased to an S/N of 5 to avoid the large number of events around $S/N \approx 3$. For H1 the data is uncalibrated and whitened, and as the calibration lines lie below 1000 Hz they are out of our band [88], meaning that many spectral features will be suppressed (see figure 4.9). This *background* analysis produced a total of 2814 events with $S/N > 5$ with a maximum S/N of 7.2 (see figure 4.10). This is at a similar level to the analysis on Gaussian noise. The ring-down code is sensitive to lines in the spectrum, with lines at ~ 1040 Hz producing an excess of events as well as the strongest events (see figure 4.11). As certain events are from a known origin, i.e. the line, it is perhaps possible to veto them and therefore bring down our final choice of S/N cut for the results. A histogram comparing the S/N of events with those thought to be caused by the line feature (between 1025-1050 Hz) removed over the histogram of all events is shown in figure 4.12. It can be seen that the strongest

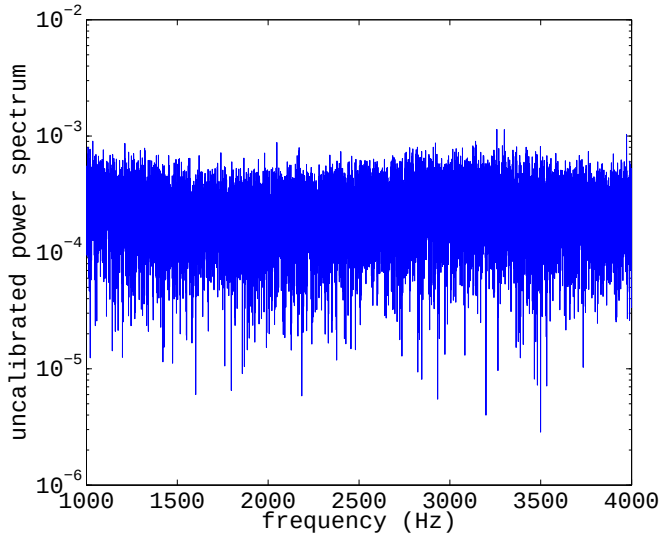

Figure 4.9: The uncalibrated spectrum of H1 (in ADC units) for 60 s from GPS 78822000, high-pass filtered at 800 Hz.

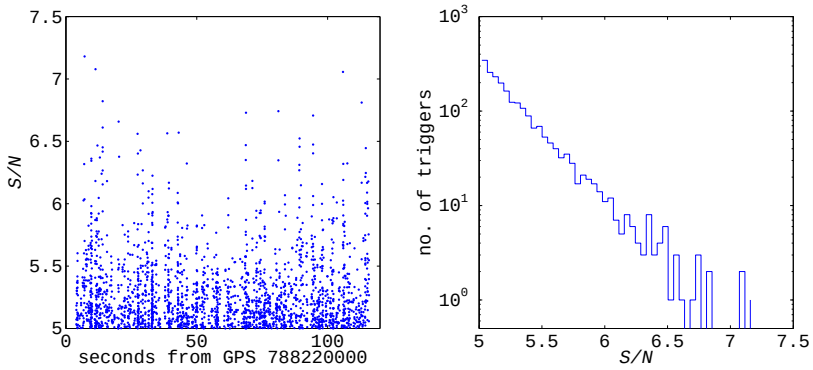

Figure 4.10: The distribution in S/N of events from the matched filtering algorithm for 120 s of H1 data from GPS 788220000.

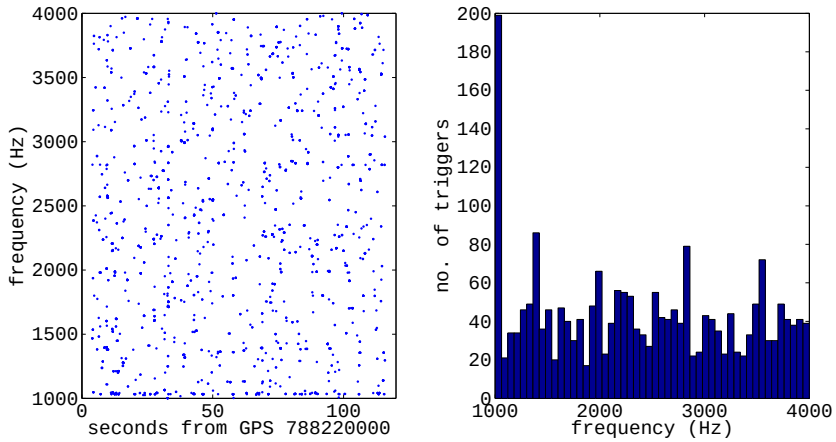

Figure 4.11: The distribution in frequency of events from the matched filtering algorithm for 120 s of H1 data from GPS 788220000.

events ($S/N > 7$) appear to be caused by the line feature, and with these removed the maximum S/N is 6.8. The fact that the line has been removed in post-processing (rather than attempting to filter it out in the data before analysis) means that it is impossible to tell if the events were really triggered by the line or not, so it is safest to use all the triggers for our S/N threshold rather than removing them in a semi-ad-hoc way. Figure 4.12 also shows that, other than the obvious line-like features, the S/N is fairly level across the frequency range, meaning that it is probably best to use a single S/N threshold cut across all frequencies. It can been seen in figure 4.13 that there are

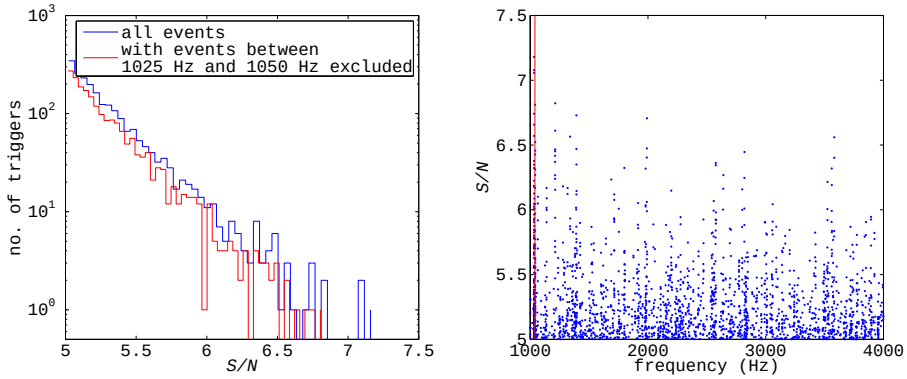

Figure 4.12: On the left is a histogram of S/N for events with and without removing those between the frequencies of 1025-1050 Hz. On the right is the S/N against frequency where the excess events around the $\sim$ 1040 Hz lines can be seen.

three distinct amplitude bands of events, which relate to the three bands of templates over Q seen in figure 4.7. The band of events with the smallest amplitude relate to those with the largest Q values, with successively smaller Qs giving successively larger amplitude events.

The GEO 600 data being used is already calibrated and contains many large spectral features within our search band which dominate the spectrum (see figure 4.14). Again the matched filtering code was run over a 120 s section of data away from the GRB time to gauge a background level of events and their S/Ns. This produced 13 589 events with an $S/N > 5$ (see figure 4.15), compared with the 2814 found in the H1 data, suggesting that the GEO 600 data is far less clean, as can indeed be seen from the spectrum. Figure 4.15 also shows a large cluster of events around GPS 788220100 suggesting some disturbance in the data. The tail in events extends further than that

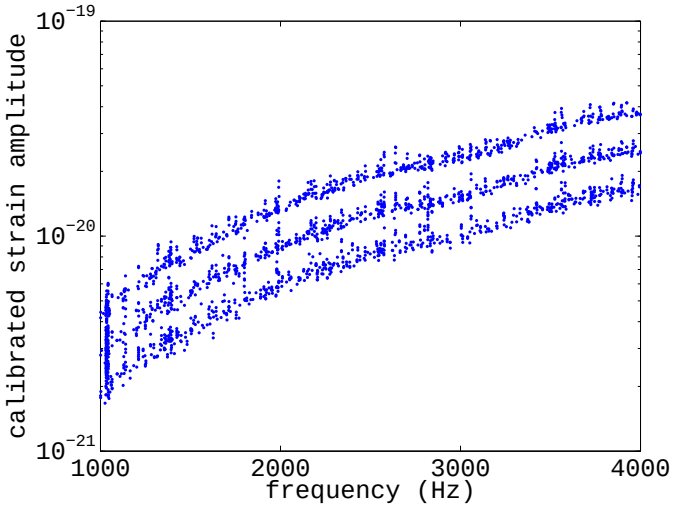

Figure 4.13: The calibrated strain amplitude of events against frequency for 120 s of H1 data from GPS 788220000.

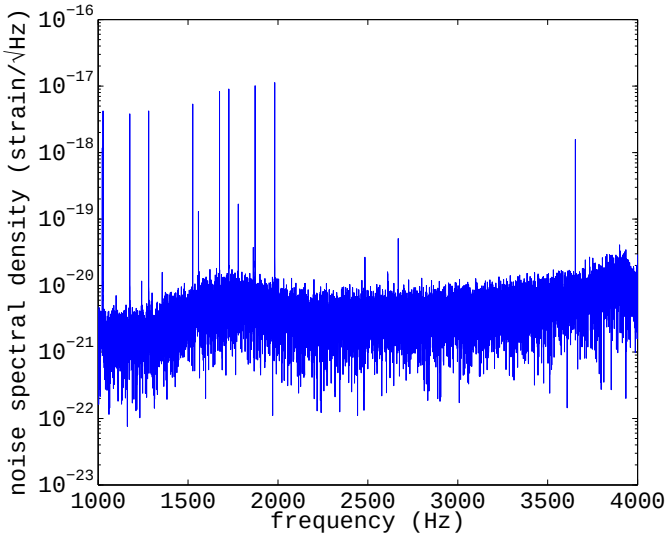

Figure 4.14: The noise spectral density for GEO 600 estimated from ten 4 s Hanning windowed segments with 50% overlap from GPS 788220060.

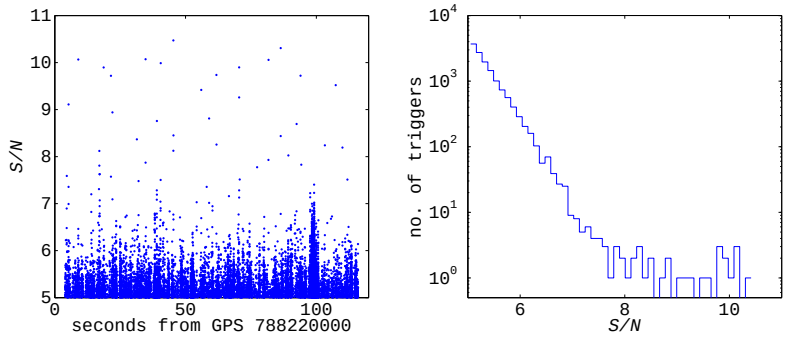

Figure 4.15: The distribution in S/N of events from the matched filtering algorithm for 120 s of GEO 600 data from GPS 788220000.

for H1 with a maximum S/N of 10.5. The large lines in the spectrum below 2000 Hz are picked up strongly by the matched filters (see figure 4.16) with the disturbance at around GPS 788220100 contributing a significant amount of events in the upper half of the frequency range. The larger number of lines in the spectrum makes it harder to veto out with confidence triggers that they were caused by the lines, although it is obvious from figures 4.16 and 4.17 that the largest S/N triggers are caused by a line at $\sim$ 1176 Hz. From these background studies we can set thresholds on the S/N at

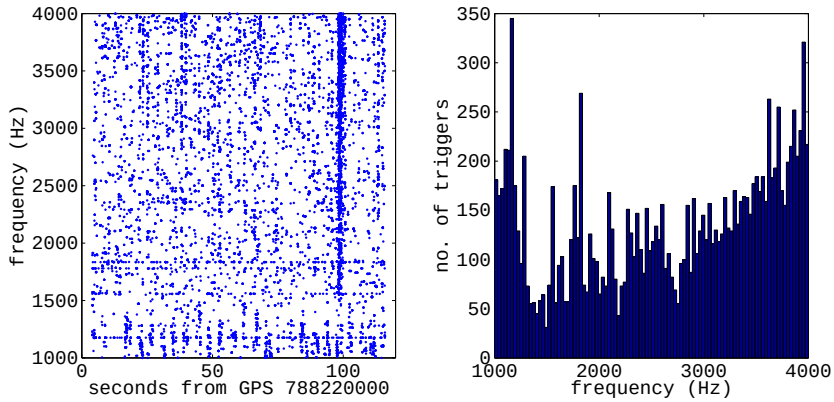

Figure 4.16: The distribution in frequency of events from the matched filtering algorithm for 120 s of GEO 600 data from GPS 788220000.

the time of the glitch, which we will take as > 8 for H1 and > 11 for GEO 600.

After calculating a background threshold the matched filtering code was then run over the 120 s surrounding the time of the glitch, using the same parameters as for the background and simulated noise studies. This provided 12 537 events for GEO 600 and 2126 events for H1 with $S/N > 5$. These numbers are similar to those found on the

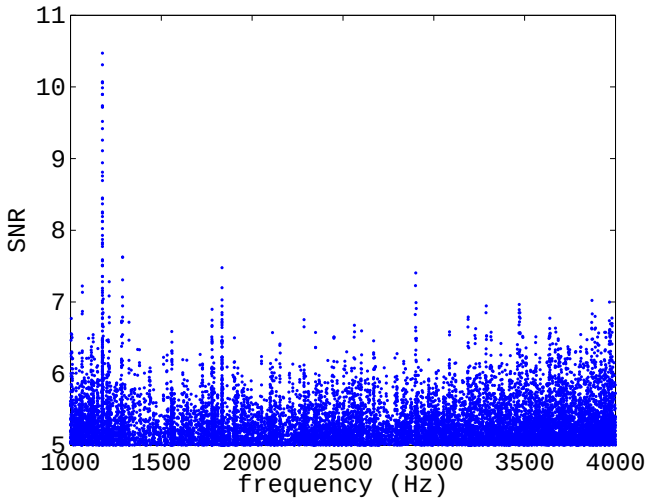

Figure 4.17: The S/N against frequency for events from the matched filtering algorithm for 120 s of GEO 600 data from GPS 788220000.

background segments. No events rise above our thresholds to give us any possible astrophysical triggers. In H1 the strongest events appear approximately 4.3 seconds before the time of the GRB, although these appears to be associated with the ~ 1040 Hz line feature becoming particularly strong around this time (see also the evidence analysis below).

The most obvious veto for non-gravitational wave signals is coincidence between detectors. Any gravitational wave signal strong enough should be visible in data from multiple detectors, with coincidence between arrival times and amplitudes. This is most useful, and allows the the most stringent thresholds to be set, when the detectors are of comparable sensitivity and are coaligned. For the detector pair we have, the GEO 600 data is approximately an order of magnitude less sensitive than H1, meaning that any signal visible to both would be very strong in H1. The fact that the detectors are not coaligned also means that they have different responses to the gravitational wave polarisation, which additionally complicates things. This factor will reduce the effective gravitational wave amplitude for all except a source optimally positioned directly above the plane of the detector. The polarisation of any signal is unknown, so any coincidence threshold will have to be set with this reduction factor in mind for the less sensitive detector. In our search for gravitational waves from SGR 1806-20

we know the source position and can therefore calculate the detectors' responses to different source orientations. For GEO 600 the factor $\sqrt{F_+^2 + F_\times^2} = 0.84$ and for H1 it is 0.50.

In our case where no triggers are seen above the set S/N threshold no coincidence analysis is possible. If we were to reduced our threshold too far however, say to the $S/N > 5$ used in the background analyses, it would become difficult to use such a coincidence veto with the large number of events seen leading to many accidental coincidences.

Many events will be produced by artifacts which do not in fact resemble our expected ring-down waveform, as seen with the events from instrumental lines, so some method of vetoing these is useful. In the matched filter search for inspiralling binaries a χ^2 based discriminator is used to veto such events [122]. The evidence based search below was originally conceived as a possible waveform consistency veto, with the hope of combining the matched filter results and evidence searches.

Evidence search

This method is most efficient if the ring-down signal begins at the start of the data section being studied. It would take too long computationally, and be unnecessary, to implement such a search from the start of each consecutive sample at 16 384 Hz. A time step of $\frac{1}{8}$ s and a data length of 1 s was chosen as a reasonable duration to catch the shortest events and span the longest events. The overlap between consecutive data segments (0.875 s) means that the evidence for each is not truly independent and could be correlated.

As with the matched filtering search we want to gauge some background level for this method. It was seen in figure 4.4 that Gaussian noise will give a certain background level, but again real data needs studying. For this purpose the same section of off-source data as used in the matched filter search was studied. The data for both H1 and GEO 600 was high-pass filtered to remove low frequency noise before applying the evidence finding algorithm. The first evidence value from each data segment analysed

was ignored due to contamination from the filter response, although overlapping of data in the analysis meant that all the time was covered. The evidence for 4776 overlapping segments from H1 (covering 597 s) from GPS 788220000 can be seen in figure 4.18. The

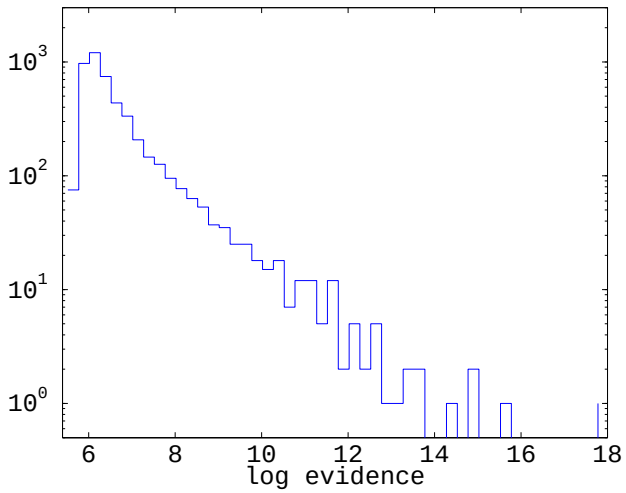

Figure 4.18: The evidence of a ring-down signal in H1 data from GPS 788220000 for 597 s.

H1 data was uncalibrated and whitened so certain spectral features were suppressed. As with the test on Gaussian noise figure 4.18 shows the value of log evidence clustering around 6, with a mean of 6.55. For real data a larger tail to the evidence is present suggesting more spectral contamination within the frequency band. This can be seen when looking at the posterior pdf of frequency at times when the evidence is highest, for example at the time of the maximum value of log evidence = 17.9. From the studies on Gaussian noise such high evidence values would suggest the presence of a signal, but figure 4.19 shows that this value is almost entirely due to the spectral line at $f \sim 1045$ Hz, as seen in the matched filter studies above. This was confirmed as a spectral line feature, and not an actual signal, by studying spectra from periods long before the GRB occurred. This means that without removing this spectral feature a far higher threshold on the evidence than is suggested by Gaussian noise studies is needed. We will set a threshold of log evidence > 20 for the data around the GRB.

The search performed on the 120 s of data around the time of the GRB produces evidence values similar to those in the background (see figure 4.20). There are spikes in the evidence which, as with the background data, are caused by the spectral lines,

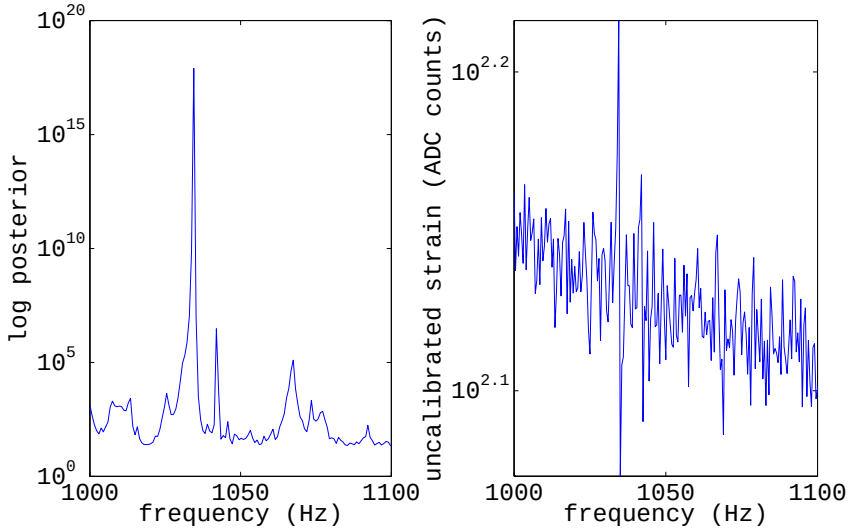

Figure 4.19: Comparison of the posterior pdf of frequency from the Bayesian method for the data giving the highest background evidence value and an FFT of the same data.

like the matched filter events. The highest value of log evidence = 18.3 occurs ~ 4.3 s before the GRB, at the same time as the highest S/N matched filter event, suggesting the same source. The frequency posterior and spectrum have been examined showing the $f \sim 1045$ Hz spectral line to be particularly strong at this time. None of these spikes crosses our log evidence > 20 threshold.

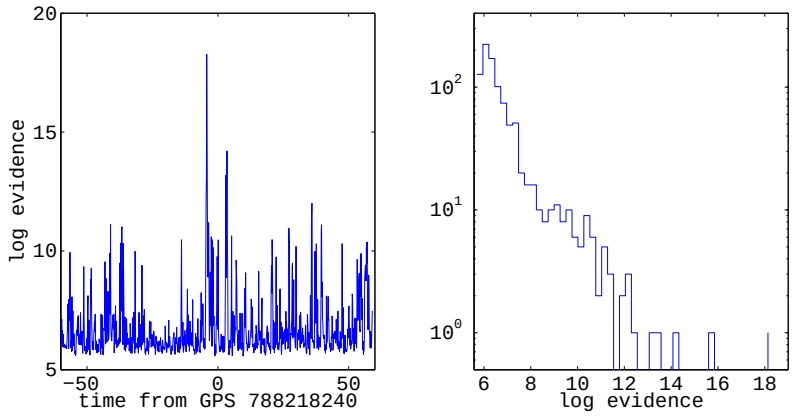

Figure 4.20: The evidence of a ring-down signal in H1 data from for 120 seconds around the GRB time of GPS 788218240 s.

Using studies of the efficiency of this algorithm it still might prove useful in vetoing H1 triggers above the original matched filter S/N threshold of 5. To do this a simulation has been performed in which 4000 ring-down signals of varying amplitude, frequency

and decay time have been injected into Gaussian noise and the S/N and evidence calculated. These signals have a start time that varies randomly between $0 - \frac{1}{8}$ s to reproduce the time step between consecutive segments used in the actual analysis. The evidence as a function of S/N is plotted in figure 4.21. The flat roof on the evidence is an artifact of the evidence code, which sets the posterior value equal to e^{230} ($\approx 10^{100}$) if it is greater than this, due to it otherwise getting outside the dynamic range allowed by double precision. We need to set some evidence limit for which we believe the code

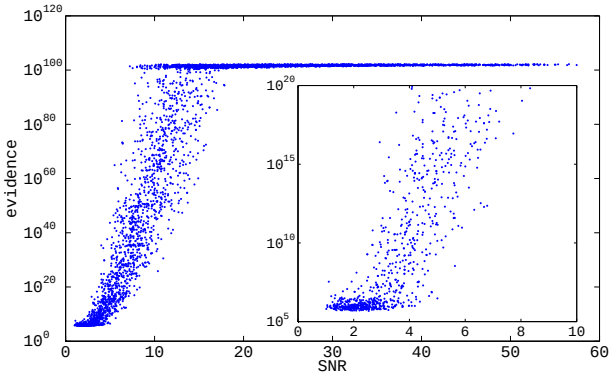

Figure 4.21: The evidence for ring-down signals against the signal S/N for 4000 simulated ring-down signals injected into Gaussian noise.

has truly seen the signal. From our studies on Gaussian noise with no signal injected (see figure 4.4) we can see that evidence values can reach out to nearly $10^{8.5}$ with a mean of $\sim 10^6$, so conservatively we can say that we see a signal if the evidence is $> 10^{10}$. From figure 4.21 this means that we see all the events with $S/N > 5.63$. Using this evidence threshold we can plot the efficiency of the search (see figure 4.22) and see that above an S/N of 6 we see all triggers and below an S/N of 2.5 we see no triggers.

It has been seen that lines in the spectra can produce a large evidence value even though they are not ring-downs. To estimate how this could effect the analysis we have done a simulation by injecting 2000 sinusoids with random frequency and amplitude parameters into Gaussian noise. The evidence against S/N is plotted in figure 4.23 and shows that, using our evidence threshold of above 10^{10} being a signal detection, all sinusoids with $S/N \gtrsim 6.7$ will be picked up. This shows that the evidence as it is

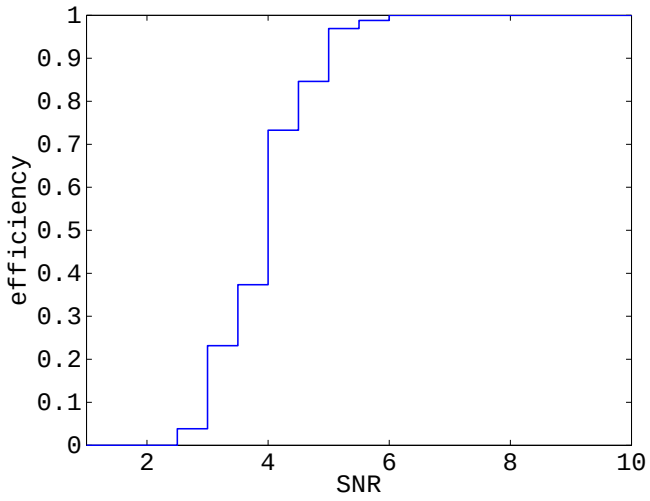

Figure 4.22: The efficiency of the evidence search for different signal S/Ns.

currently implemented, using short 1 second stretches of data, is not promising as a method of distinguishing ring-downs from lines, and possible extensions to this end are discussed below.

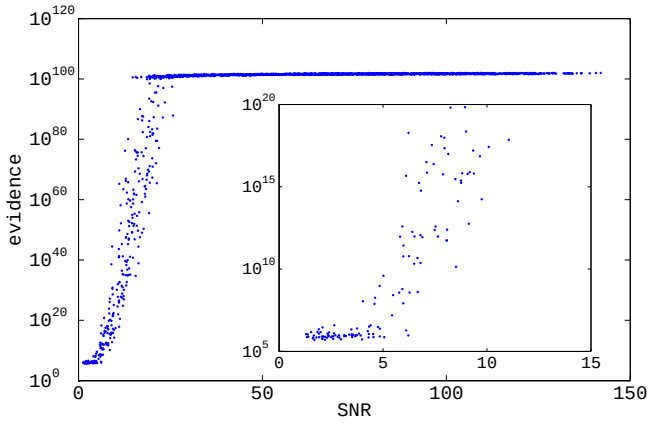

Figure 4.23: The evidence for ring-down signals against S/N for 2000 simulated sinusoids injected into Gaussian noise.

Detector data can also contain many transient δ-function like events, so a simulation has been performed to see whether these trigger our evidence algorithm above the level of Gaussian noise. 2000 δ-functions have been in injected into Gaussian noise with a range of amplitudes (see figure 4.24) and it can be seen that all evidence values are well below our evidence threshold of 10^{10} and cover a very similar range to those from pure noise (see figure 4.4). Such signals do not seem to affect our algorithm in any

way. In the future other types of signal such as ring-ups or chirps will be tested.

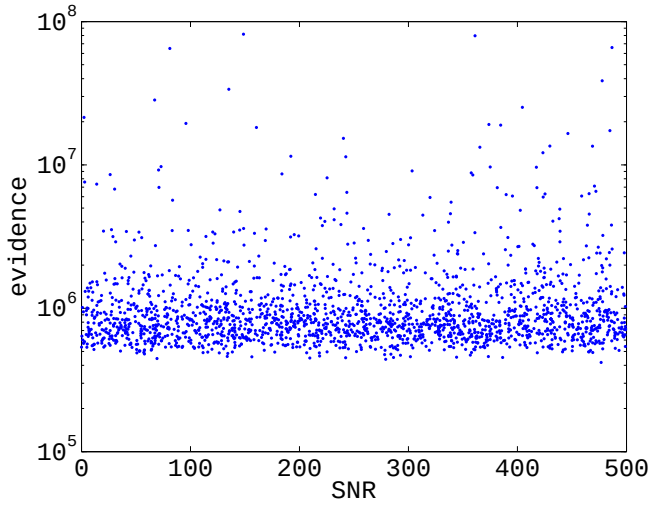

Figure 4.24: The evidence for ring-down signals against S/N for 2000 simulated δ-functions injected into Gaussian noise.

For GEO 600 the data is calibrated and contains very strong calibration lines within our band of study. Without the removal of these lines it makes our evidence studies almost useless as they completely swamp the evidence. This can be seen in the frequency posterior pdf for a section of GEO 600 data (see figure 4.25) in which almost all the probability is at the frequencies of the spectral lines shown in figure 4.14. These

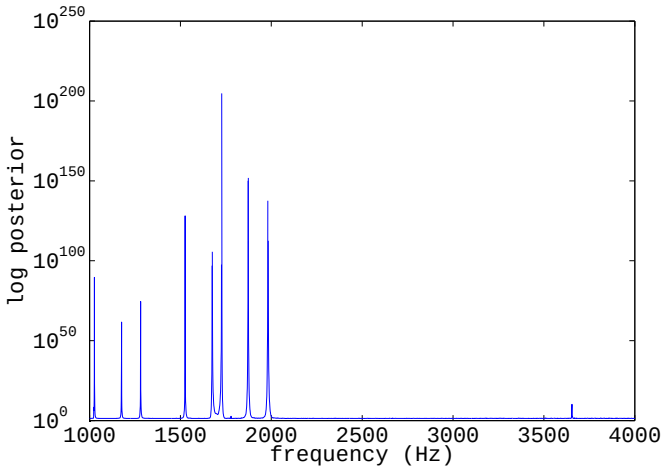

Figure 4.25: The frequency posterior for ring-down signals in a section of GEO 600 data.

excessively large probability values also make it hard to calculate a true value of the evidence as they will be out of the range of the double precision variable in the code.

For all the GEO 600 data analysed this limit on the evidence is reached just from the spectral lines and can therefore tell us nothing about the presence of ring-down signals.

These studies show that the Bayesian evidence method, as currently implemented, does not sufficiently discriminate against non-decaying sinusoids. In the absence of there being any better alternative hypothesis the code will take sinusoids as the nearest thing to a ring-down signal. In our implementation this happens because of the short 1 s time of the data segments being used. It was shown that for δ-functions, which are essentially very short ring-downs, the 1 s time stretch is long enough by far that the probability that they are within our range of τ becomes very small. If the segment times were increased then the probability of long duration sinusoids being within our τ range should also be small, although a very preliminary test shows that this timescale needs to be $\gg 100$ s.

There are several possible options which could be implemented in the future to help make the algorithm more robust against non-ring-down signals. One way, as just stated, would be to increase the length of data segments. This could become computationally expensive, although if the marginalisation can be performed analytically, or at least approximated analytically, then this would become far more practical. Another obvious method is to use notch filters to remove known instrumental lines e.g. calibration lines, suspension violin modes. A more complex method would be to extend the Bayesian analysis to include non-decaying sinusoids in some way that they can be excluded. This would mean that a number of sinusoidal models, N, could be included

$$y(t) = A\sin(2\pi f t + \phi_0)e^{-(t-T_0)/\tau} + \sum_{i=1}^{N} B_i \sin(2\pi f_i t + \phi_i), \tag{4.19}$$

which would provide a better model for any line features to assume, leaving the ring-down model free to estimate the presence of ring-down signals alone. Along similar lines you could instead have N ring-down models and veto any with values of τ outside our range, which would include non-decaying sinusoids with $\tau = \infty$, or transient delta functions with $\tau \to 0$. Or a model with N_1 ring-downs and N_2 sinusoids. The parameter T_0 could also be searched over, eliminating the need for large numbers of overlaps

between successive data segments. This could become computationally expensive for data with many lines and might need to be implemented using an MCMC approach. This would be similar to a method being developed to estimate the large number white dwarf binary system in LISA data [123].

4.3.3 Results

The aim of this search was to find out whether or not any ring-down gravitational wave burst was seen associated with the 27th December 2004 GRB and in that the result is negative. We are however, able to set an upper limit on gravitational wave emission by making use of our S/N thresholds. These results only make use of the matched filter search.

For GEO 600 data no triggers were seen above our S/N threshold of 11 across our entire frequency range, so using the antenna response of 0.84 we can produce an upper limit on the effective strain from our source as given by figure 4.26. For the H1 data no

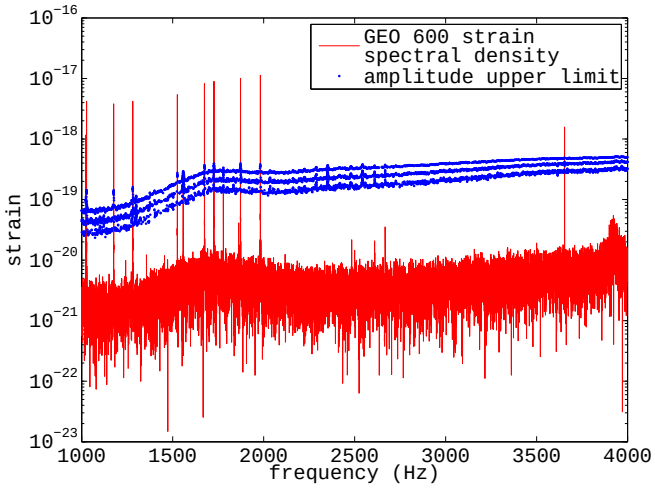

Figure 4.26: The upper limit on effective amplitude of ring-down signals from SGR 1806-20 using GEO 600 data shown along with an estimate of the noise spectral density.

triggers were seen above our S/N threshold of 8 across the entire frequency range, so using the antenna response of 0.50 we can produce an upper limit on the effective strain as given in figure 4.27. The H1 data gives the most stringent upper limits with them ranging from $h_0 \sim 10^{-20}$ at the low frequency end to $h_0 \sim 10^{-19}$ at the high frequency

end. The S/N, and therefore amplitudes, will have an error of about 5% from the 10% filter mis-match used in the matched filtering. These results are plotted in terms of an upper limit on the energy emitted (via equation 4.4 using $r = 15\,\mathrm{kpc}$) in figure 4.28. This gives an upper limit on the energy emitted ranging from $E \sim 2{\times}10^{-6}\,\mathrm{M}_{\odot}c^2$ at the

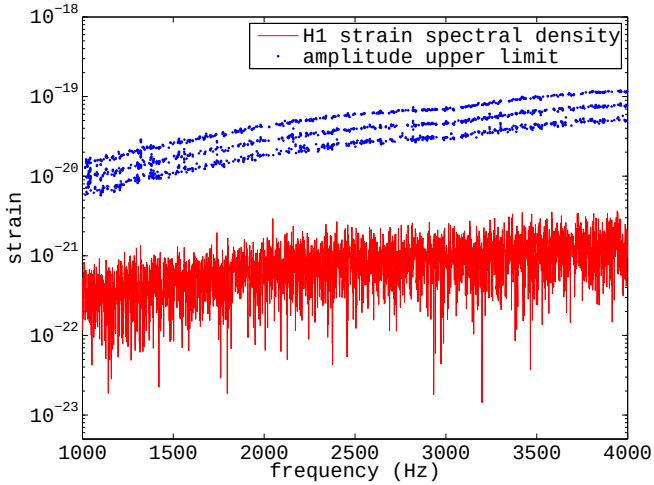

Figure 4.27: The upper limit on the effective amplitude of ring-down signals from SGR 1806-20 using H1 data shown along with an estimate of the noise spectral density.

low frequency end to $E \sim 5{\times}10^{-4}\,\mathrm{M}_{\odot}c^2$ at the high frequency end (see figure 4.28). The results at low frequency beat those given in Baggio *et al.* (2005) [4] although do not quite extend into their frequency range. The results are still about 3 orders of magnitude greater than the upper limit from spin-down argument set above with $h_{\mathrm{eff}} < 10^{-23}$, but are into the range of amplitudes expected from new born neutron stars. Thus we are starting to get into the range of some interesting astrophysics.

Here we have performed and described only a preliminary analysis of this data, with much work still needed. The data can be made more effective for this study with some line removal strategy. A background coincidence analysis can be performed to attempt to reduce the S/N threshold. The matched filter search and evidence search will also be combined to provide increased confidence in the result. Therefore a more detailed analysis of the data could potentially push down the upper limits stated above.

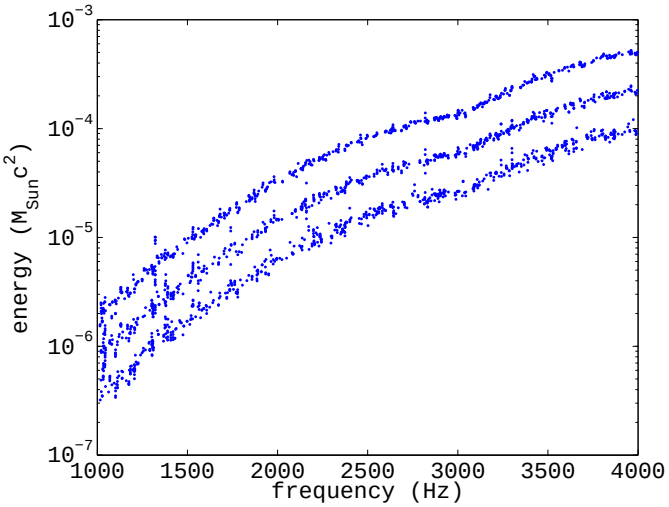

Figure 4.28: The upper limit on energy of ring-down signals from SGR 1806-20 using H1 data.

4.4 Other pulsar ring-down studies

4.4.1 Crab and Vela pulsar glitches

The Crab and Vela pulsars have both glitched during periods when at least one interferometer has been taking data. For the Crab pulsar these glitches have been on 3$^{\text{rd}}$ March, 6$^{\text{th}}$ September and 12$^{\text{th}}$ November 2004 [73]. For the Vela pulsar a glitch with a fractional change in period of 2.1×10^{-6} was observed on 7$^{\text{th}}$ July 2004 [124]. At present this data has yet to be dug out and analysed and although a detection is very unlikely these could provide some interesting upper limits.

You win again, gravity.

Captain Zapp Brannigan - Futurama

Chapter 5

Future work

The present status of the ongoing search for gravitational waves is that no evidence has yet been seen for their direct detection. Despite this pessimistic sounding statement we are still advancing ever closer towards the first direct sighting. In the meantime we are reaching the point where interesting astrophysics can be gained from our null results. Upper limits on various emission mechanisms and event rates can begin to constrain theoretical models of sources and population studies.

This thesis has given the current status of the search for gravitational waves from a selection of known neutron stars via two different mechanisms. This, however, is not the end state of each search, with much more work continuing in the future.

5.1 The known pulsar search

One of the first things to be noted is that here we have searched for 93 known pulsars, this being the number for which adequate timing solutions were available. There are currently 150 pulsars within our band, with more being discovered from radio surveys on a regular basis. This will increase our search sample and hopefully provide some candidates with more promising detection possibilities i.e. young pulsars with high spin-down rates. We are in close contact with radio astronomers to get the most up-to-date timing solutions possible, although obviously timing observations from the time of a science run can only be used in a post-run analysis. As we have seen from their

inferred spin-down upper limits the *known* radio pulsars are not the best candidates for gravitational wave detection. There are, however, several pulsars only seen in X-rays which might provide better candidates, for example PSR J0537-6910 described in §3.4.7. With several space-based high energy telescopes (the *Rossi X-ray Timing Explorer*, *Chandra*, *XMM-Newton* and *INTEGRAL*) currently operating, X-ray pulsars, mainly those in LMXB systems, are becoming a far more studied source. These provide more enticing candidates, with conditions for sustaining gravitational wave emission being more favourable. Other enticing places to search are SNRs, with Veitch *et al.* (2005) [64] developing a search for a possible remnant of SN 1987A. Due to the many X-ray pulsars and other potential sources having far less well defined, or unknown, parameters than many radio pulsars, a search as performed in this thesis would be inadequate. The MCMC search for gravitational waves from a SN 1987A remnant in [64] could, for instance, be extended to search over binary parameters and used in LMXB searches.

The search algorithm, as it is currently used by performing a single fine grained heterodyne at the exact pulsar phase, is computationally fairly slow. The main speed restriction on this is having to compute the Doppler correction to the SSB (and binary system barycentre for some) for every data sample. This will only get slower as more pulsars are included. The speed of the algorithm also becomes a problem if the data has to be re-analysed many times, for example if certain data segments were missed or new calibration data is used. One possible method to reduce the computational burden of the search, and more easily allow repeated analysis, would be to return to a two stage heterodyne process similar to that used in the S1 pulsar search [33]. This performed an initial heterodyne at the pulsar frequency, but did not include spin-down or Doppler corrections, allowing the data to be massively down-sampled and filtered before the finer corrections were applied in a second heterodyne. There are some limitations on this, in that the down-sampling and filtering must be able to accommodate the frequency range drift caused by Doppler motions, with particular care for binary pulsars, although going from 16 384 Hz to 1 Hz would still provide plenty of

range. In practice a less crude initial heterodyne using as many parameters as possible can also be used. This would mean that during the course of a science run the initial heterodyne can still be performed using older timing solutions, and then the second stage heterodyne used to perform additional phase corrections when up-to-date timing information is made available - this is essentially what is done for the Crab pulsar with regards to timing noise corrections.

The heterodyne approach may well be phased out in the longer term. When there are many pulsars across a wide range of frequencies a more sensible approach may be to use Fourier transforms of the data, which essentially provide a fixed frequency heterodyne over all frequencies. Short time baseline Fourier transforms (SFTs) of the data for LIGO and GEO 600 are already produced for the frequency domain pulsar searches and could be used for our purposes. The SFTs need to be short enough that the source's signal is not spread out over many frequency bins due to Doppler/spin-down effects. Under such an approach the exact frequency of the source would be calculated and extrapolated between successive frequency bins. This cuts down the problem computationally, as the SFTs are pre-produced and the frequency only needs to be calculated at the rate of the time baseline of the SFTs.

The marginalisation in equation 2.26 used in the Bayesian parameter estimation currently numerically sums over the nuisance parameters. The grid over which the marginalisation takes place is limited by computer memory restraints, so the integration is only approximate. The possibility of performing these integrals analytically needs to be explored.

5.2 The ring-down search

The ring-down search presented in this thesis is in a very preliminary state and was more about outlining and testing the algorithms than producing a full and thorough search pipeline. Much of what needs to be done is outlined at the end of Chapter 4. The particular case of the search for a signal from the 27^{th} December GRB needs a more thorough study of event background rates and the coincidence analysis. When

the evidence based search becomes more stable against spectral lines it will be provide a good complementary strategy to the matched filtering search. There are other glitches from the Crab and Vela pulsars to be searched for.

With S5 starting and providing an almost continuous data set for a year or so, it provides the opportunity to catch as many glitches as we can. With pulsars such as the Crab, Vela and J0537-6910 being prolific glitchers there should be several events during the run. As with the known pulsar continuous wave search, the timing for these glitches can only be obtained post-event. This will again need close cooperation with those observing the pulsars to obtain accurate information as soon as possible. Glitches seen in accreting X-ray pulsars provide an excellent target, with fractional frequency changes seen up to $\Delta\nu/\nu \sim 3\times10^{-4}$ for one such object (SAX J2103.5+4545) [125] being two orders of magnitude above the maximum seen in Vela glitches. Another good accreting X-ray potential target is KS 1947+300 which had a glitch of fractional frequency change at $\Delta\nu/\nu \sim 4\times10^{-5}$ [126].

5.3 S5 and beyond

The fifth science run (S5) of the LSC interferometers started officially on 4$^{\text{th}}$ November 2005, with H1 and H2 to start with, and L1 and GEO 600 joining later. This run marks the start of full time operation of the interferometers at approximately their design sensitivities. This should give sensitivities to pulsars at around that given in figure 3.10, and allow us to beat the spin-down upper limits for at least the Crab pulsar by approximately an order of magnitude.

Towards the end of the decade LIGO will be decommissioned and upgrades to Advanced LIGO installed. This should give access to many more potential sources and beat the spin-down limits for many pulsars. Possible upgrades to GEO 600 to tune it to the high frequencies could provide a good window to look at oscillation modes of neutron stars, with possibilities extending beyond the fundamental f-mode. This would perhaps be able to spot high frequency oscillations from newborn neutron stars to a large distance.

Hopefully gravitational wave astronomy will soon be able to provide much needed insight into the structure and nature of neutron stars, which is currently open to much speculation. This will be complimentary to electromagnetic studies, but should provide a wealth of unique information.

Bibliography

[1] R. J. Dupuis and G. Woan. Bayesian estimation of pulsar parameters from gravitational wave data. *Phys. Rev. D*, 72:102002–+, 2005.

[2] `http://pulsar.princeton.edu/tempo/`.

[3] G. Larry Bretthorst. *Bayesian Spectrum Analysis and Parameter Estimation.* Lecture Notes in Statistics. Spinger-Verlag, Berlin Heidleberg, 1988.

[4] L. Baggio *et al.* Upper Limits on Gravitational-Wave Emission in Association with the 27 Dec 2004 Giant Flare of SGR1806-20. *Phys. Rev. Lett.*, 95(8):081103–+, August 2005.

[5] B. F. Schutz. Gravitational waves on the back of an envelope. *Am. J. Phys.*, 52:412–419, May 1984.

[6] A. Einstein. On the general theory of relativity. *Sitzungsberichte Preußische Akademie der Wissenschaften (Berlin)*, (778), 1915.

[7] A. Einstein. On gravitational waves. *Sitzungsberichte Preußische Akademie der Wissenschaften (Berlin)*, (157), 1918.

[8] B. F. Schutz. *A first course in general relativity.* Cambridge University Press, Cambridge, 1985.

[9] M. A. Hendry. *Gravitational Radiation.* Lecture Notes in Gravitation and Relativity II. Unversity of Glasgow, 2005.

[10] É. É. Flanagan and S. A. Hughes. The basics of gravitational wave theory. *New Journal of Physics*, 7:204–+, September 2005.

[11] B. F. Schutz. Gravitational wave astronomy. *Class. Quantum Grav.*, 16:A131–A156, December 1999.

[12] K. S. Thorne. Gravitational Radiation. In S. K. Hawking and W. Israel, editors, *300 Years of Gravitation*. Cambridge University Press, Cambridge, 1987.

[13] C. Cutler, G. Ushomirsky, and B. Link. The Crustal Rigidity of a Neutron Star and Implications for PSR B1828-11 and Other Precession Candidates. *Astrophys. J.*, 588:975–991, May 2003.

[14] D. I. Jones and N. Andersson. Gravitational waves from freely precessing neutron stars. *Mon. Not. R. Astron. Soc.*, 331:203–220, March 2002.

[15] N. Andersson. A New Class of Unstable Modes of Rotating Relativistic Stars. *Astrophys. J.*, 502:708–+, August 1998.

[16] R. A. Hulse and J. H. Taylor. Discovery of a pulsar in a binary system. *Astrophys. J. Lett.*, 195:L51–L53, January 1975.

[17] J. H. Taylor and J. M. Weisberg. Further experimental tests of relativistic gravity using the binary pulsar PSR 1913+16. *Astrophys. J.*, 345:434–450, October 1989.

[18] G. Nelemans *et al.* Population synthesis for double white dwarfs . I. Close detached systems. *Astron. Astrophys.*, 365:491–507, January 2001.

[19] R. A. Saffer, M. Livio, and L. R. Yungelson. Close Binary White Dwarf Systems: Numerous New Detections and Their Interpretation. *Astrophys. J.*, 502:394–+, July 1998.

[20] M. Burgay *et al.* An increased estimate of the merger rate of double neutron stars from observations of a highly relativistic system. *Nature*, 426:531–533, December 2003.

[21] V. Kalogera *et al.* The Cosmic Coalescence Rates for Double Neutron Star Binaries. *Astrophys. J. Lett.*, 601:L179–L182, February 2004.

[22] V. Kalogera *et al.* Erratum: "The Cosmic Coalescence Rates for Double Neutron Star Binaries". *Astrophys. J. Lett.*, 614:L137–L138, October 2004.

[23] C.-H. Lee and G. E. Brown. Double Neutron Star Binaries: Implications for LIGO. *ArXiv Astrophysics e-prints* `astro-ph/0510380`, October 2005.

[24] D. B. Fox *et al.* The afterglow of GRB 050709 and the nature of the short-hard γ-ray bursts. *Nature*, 437:845–850, October 2005.

[25] J. D. E. Creighton. Search techniques for gravitational waves from black-hole ringdowns. *Phys. Rev. D*, 60(2):022001–+, July 1999.

[26] A. I. MacFadyen and S. E. Woosley. Collapsars: Gamma-Ray Bursts and Explosions in "Failed Supernovae". *Astrophys. J.*, 524:262–289, October 1999.

[27] N. Andersson and K. D. Kokkotas. Towards gravitational wave asteroseismology. *Mon. Not. R. Astron. Soc.*, 299:1059–1068, October 1998.

[28] B. Abbott *et al.* Upper Limits on a Stochastic Background of Gravitational Waves. *Physical Review Letters*, 95(22):221101–+, November 2005.

[29] J. Weber. Detection and Generation of Gravitational Waves. *Phys. Rev.*, 117:306–313, January 1960.

[30] B. Willke *et al.* The GEO 600 gravitational wave detector . *Class. Quantum Grav.*, 19:1377–1387, April 2002.

[31] A. Abramovici *et al.* LIGO - The Laser Interferometer Gravitational-Wave Observatory. *Science*, 256:325–333, April 1992.

[32] B. Abbott *et al.* Detector description and performance for the first coincidence observations between LIGO and GEO. *Nucl. Instrum. Methods Phys. Res., Sect. A*, 517:154–179, January 2004.

[33] B. Abbott *et al.* Setting upper limits on the strength of periodic gravitational waves from PSR J1939+2134 using the first science data from the GEO 600 and LIGO detectors. *Phys. Rev. D*, 69(8):082004–+, April 2004.

[34] B. Abbott *et al.* Limits on Gravitational-Wave Emission from Selected Pulsars Using LIGO Data. *Phys. Rev. Lett.*, 94(18):181103–+, May 2005.

[35] B. Abbott *et al.* First all-sky upper limits from LIGO on the strength of periodic gravitational waves using the Hough transform. *Phys. Rev. D*, 72:102004–+, 2005.

[36] B. Abbott *et al.* First upper limits from LIGO on gravitational wave bursts. *Phys. Rev. D*, 69(10):102001–+, May 2004.

[37] B. Abbott *et al.* Upper limits on gravitational wave bursts in LIGO's second science run. *Phys. Rev. D*, 72(6):062001–+, September 2005.

[38] B. Abbott *et al.* Upper limits from the LIGO and TAMA detectors on the rate of gravitational-wave bursts. *Phys. Rev. D*, 72(12):122004–+, December 2005.

[39] B. Abbott *et al.* Search for gravitational waves associated with the gamma ray burst GRB030329 using the LIGO detectors. *Phys. Rev. D*, 72(4):042002–+, August 2005.

[40] B. Abbott *et al.* Analysis of LIGO data for gravitational waves from binary neutron stars. *Phys. Rev. D*, 69(12):122001–+, June 2004.

[41] B. Abbott *et al.* Search for gravitational waves from galactic and extra-galactic binary neutron stars. *Phys. Rev. D*, 72(8):082001–+, October 2005.

[42] B. Abbott *et al.* Search for gravitational waves from binary black hole inspirals in LIGO data. *ArXiv General Relativity and Quantum Cosmology e-prints* `gr-qc/0509129`, September 2005.

[43] B. Abbott *et al.* Search for gravitational waves from primordial black hole binary coalescences in the galactic halo. *Phys. Rev. D*, 72(8):082002–+, October 2005.

[44] B. Abbott *et al.* Analysis of first LIGO science data for stochastic gravitational waves. *Phys. Rev. D*, 69(12):122004–+, June 2004.

[45] W. Baade and F. Zwicky. Cosmic Rays from Super-novae. *Proc. Nat. Acad. Sci.*, 20:259–263, 1934.

[46] A. Hewish *et al.* Observation of a Rapidly Pulsating Radio Source. *Nature*, 217:709–+, 1968.

[47] Australia Telescope National Facility Pulsar Catalogue `http://www.atnf.csiro.au/research/pulsar/psrcat/`.

[48] D. R. Lorimer. Binary and Millisecond Pulsars at the New Millenium. *Living Rev. Relativity*, 4(5), 2001. (cited on 25/11/05) `http://www.livingreviews.org/lrr-2001-5`.

[49] C. Palomba. Pulsars ellipticity revised. *Astron. Astrophys.*, 354:163–168, February 2000.

[50] F. E. Marshall *et al.* The Big Glitcher: The Rotation History of PSR J0537-6910. *Astrophys. J.*, 603:682–689, March 2004.

[51] O. Benhar. Neutron Star Matter Equation of State and Gravitational Wave Emission. *Mod. Phys. Lett. A*, 20:2335–2349, 2005.

[52] V. R. Pandharipande, D. Pines, and R. A. Smith. Neutron star structure : theory observation, and speculation. *Astrophys. J.*, 208:550–566, September 1976.

[53] P. Jaranowski, A. Królak, and B. F. Schutz. Data analysis of gravitational-wave signals from spinning neutron stars: The signal and its detection. *Phys. Rev. D*, 58:63001–+, September 1998.

[54] M. Zimmermann and E. Szedenits, Jr. Gravitational waves from rotating and precessing rigid bodies: Simple models and applications to pulsars. *Phys. Rev. D*, 20:351–355, July 1979.

[55] N. Andersson, K. D. Kokkotas, and N. Stergioulas. On the Relevance of the R-Mode Instability for Accreting Neutron Stars and White Dwarfs. *Astrophys. J.*, 516:307–314, May 1999.

[56] A. Melatos and D. J. B. Payne. Gravitational Radiation from an Accreting Millisecond Pulsar with a Magnetically Confined Mountain. *Astrophys. J.*, 623:1044–1050, April 2005.

[57] H. Hirakawa, K. Tsubono, and M.-K. Fujimoto. Search for gravitational radiation from the Crab pulsar. *Phys. Rev. D*, 17:1919–1923, April 1978.

[58] T. Suzuki. Search for Continuous Gravitational Wave from Pulsars with Resonant Detector. In *First Edoardo Amaldi Conference on Gravitational Wave Experiments*, pages 115–+, 1995.

[59] J. Hough *et al.* Direct observational upper limit to gravitational radiation from millisecond pulsar PSR1937+214. *Nature*, 303:216–+, May 1983.

[60] M. Hereld. *A search for gravitational radiation from PSR 1937+2134.* PhD thesis, California Institute of Technology, 1983.

[61] G. Mendell. Incoherent wide parameter-space searches for gravitational waves from neutron stars using LIGO S2 and S3 data. *APS Meeting Abstracts*, pages 10004–+, April 2005.

[62] V. Dergachev. Broadband Search for Continous-Wave Gravitation Radiation with LIGO. *APS Meeting Abstracts*, pages 10002–+, April 2005.

[63] P. R. Brady and T. Creighton. Searching for periodic sources with LIGO. II. Hierarchical searches. *Phys. Rev. D*, 61(8):082001–+, April 2000.

[64] J. Veitch *et al.* A time-domain MCMC search and upper limit technique for gravitational waves of uncertain frequency from a targeted neutron star. *Class. Quantum Grav.*, 22(18):995–1001, September 2005.

[65] J. Middleditch *et al.* Rapid photometry of supernova 1987A: a 2.14 ms pulsar? *New Astronomy*, 5:243–283, August 2000.

[66] R. J. Dupuis. *Bayesian searches for gravitational waves from pulsars.* PhD thesis, University of Glasgow, 2004.

[67] J. M. Cordes and D. J. Helfand. Pulsar timing. III - Timing noise of 50 pulsars. *Astrophys. J.*, 239:640–650, July 1980.

[68] Z. Arzoumanian *et al.* Timing behavior of 96 radio pulsars. *Astrophys. J.*, 422:671–680, February 1994.

[69] J. M. Cordes and G. Greenstein. Pulsar timing. IV - Physical models for timing noise processes. *Astrophys. J.*, 245:1060–1079, May 1981.

[70] D. I. Jones. Is timing noise important in the gravitational wave detection of neutron stars? *Phys. Rev. D*, 70(4):042002–+, August 2004.

[71] A. G. Lyne, R. S. Pritchard, and F. Graham-Smith. Twenty-Three Years of Crab Pulsar Rotational History. *Mon. Not. R. Astron. Soc.*, 265:1003–+, December 1993.

[72] T. Wong, D. C. Backer, and A. G. Lyne. Observations of a Series of Six Recent Glitches in the Crab Pulsar. *Astrophys. J.*, 548:447–459, February 2001.

[73] Jodrell Bank Crab Pulsar Monthly Ephemeris `http://www.jb.man.ac.uk/~pulsar/crab.html`.

[74] A. G. Lyne, R. S. Pritchard, and F. G. Smith. Crab pulsar timing 1982-87. *Mon. Not. R. Astron. Soc.*, 233:667–676, August 1988.

[75] A. G. Lyne and F. Graham-Smith. *Pulsar Astronomy.* Cambridge Astrophysics Series. Cambridge University Press, Cambridge, 2 edition, 1998.

[76] M. Pitkin and G. Woan. Searching for gravitational waves from the Crab pulsar - the problem of timing noise. *Class. Quantum Grav.*, 21:843–+, March 2004.

[77] R. Blandford and S. A. Teukolsky. Arrival-time analysis for a pulsar in a binary system. *Astrophys. J.*, 205:580–591, April 1976.

[78] S. V. Dhurandhar and A. Vecchio. Searching for continuous gravitational wave sources in binary systems. *Phys. Rev. D*, 63(12):122001–+, June 2001.

[79] A. Wolszczan *et al.* Timing Observations of Four Millisecond Pulsars with the Arecibo and Effelsberg Radio Telescopes. *Astrophys. J.*, 528:907–912, January 2000.

[80] M. Kramer. private communication, 2004.

[81] C. Lange *et al.* Precision timing measurements of PSR J1012+5307. *Mon. Not. R. Astron. Soc.*, 326:274–282, September 2001.

[82] T. Damour and N. Deruelle. General relativistic celestial mechanics of binary systems II. The post-Newtonian timing formula. *Ann. Inst. Henri Poincaré A Phys. Théor.*, 44:263–292, 1986.

[83] `http://www.lsc-group.phys.uwm.edu/daswg/projects/lalapps.html`.

[84] `http://www.lsc-group.phys.uwm.edu/daswg/projects/lal.html`.

[85] `http://www.stjarnhimlen.se/comp/time.html`.

[86] `http://ssd.jpl.nasa.gov/horizons.html`.

[87] M. Hewitson *et al.* Calibration of GEO 600 for the S1 science run. *Class. Quantum Grav.*, 20:885–+, September 2003.

[88] R. Adhikari *et al.* Calibration of the LIGO detectors for the First LIGO Scientific Run. Ligo technical document, 2003.

[89] U. Weiland *et al.* Hardware injection of simulated continuous gravitational wave signals for GEO 600. *Class. Quantum Grav.*, 21:861–+, March 2004.

[90] R. N. Manchester *et al.* The Australia Telescope National Facility Pulsar Catalogue. *Astron. J.*, 129:1993–2006, April 2005.

[91] S. M. Ransom *et al.* Twenty-One Millisecond Pulsars in Terzan 5 Using the Green Bank Telescope. *Science*, 307:892–896, February 2005.

[92] `http://www.ldas-sw.ligo.caltech.edu/ligotools/`.

[93] I. S. Shklovskii. Possible Causes of the Secular Increase in Pulsar Periods. *Soviet Astronomy*, 13:562–+, February 1970.

[94] E. S. Phinney. Pulsars as Probes of Globular Cluster Dynamics. In *ASP Conf. Ser. 50: Structure and Dynamics of Globular Clusters*, pages 141+–, 1993.

[95] J. Romano. private communication, 2005.

[96] J. H. Taylor and J. M. Cordes. Pulsar distances and the galactic distribution of free electrons. *Astrophys. J.*, 411:674–684, July 1993.

[97] D. A. Frail and J. M. Weisberg. A critical evaluation of pulsar distance measurements. *Astron. J.*, 100:743–757, September 1990.

[98] `http://www.ligo.caltech.edu/~lazz/distribution/LSC_Data/`.

[99] `http://www.aei.mpg.de/~jrsmith/geocurves.html`.

[100] S. E. Thorsett and D. Chakrabarty. Neutron Star Mass Measurements. I. Radio Pulsars. *Astrophys. J.*, 512:288–299, February 1999.

[101] D. J. Nice *et al.* A 2.1 Solar Mass Pulsar Measured by Relativistic Orbital Decay. *Astrophys. J.*, 634:1242–1249, December 2005.

[102] M. Bejger and P. Haensel. Moments of inertia for neutron and strange stars: Limits derived for the Crab pulsar. *Astron. Astrophys.*, 396:917–921, December 2002.

[103] M. Bejger and P. Haensel. Accelerated expansion of the Crab Nebula and evaluation of its neutron-star parameters. *Astron. Astrophys.*, 405:747–751, July 2003.

[104] M. Bejger, T. Bulik, and P. Haensel. Constraints on the dense matter equation of state from the measurements of PSR J0737-3039A moment of inertia and PSR J0751+1807 mass. *Mon. Not. R. Astron. Soc.*, 364:635–639, December 2005.

[105] M. Pitkin and the LIGO Scientific Collaboration. Searching for gravitational waves from known pulsars. *Class. Quantum Grav.*, 22:1277–+, September 2005.

[106] B. J. Owen. Maximum elastic deformations of compact stars with exotic equations of state. *Phys. Rev. Lett.*, 95:211101, 2005.

[107] J. M. Lattimer and M. Prakash. Neutron Star Structure and the Equation of State. *Astrophys. J.*, 550:426–442, March 2001.

[108] M. Zimmermann. Revised estimate of gravitational radiation from Crab and Vela pulsars. *Nature*, 271:524–+, February 1978.

[109] N. Andersson and K. D. Kokkotas. Gravitational Wave Astronomy: The High Frequency Window. *LNP Vol. 653: The Physics of the Early Universe*, 653:255–+, 2005.

[110] K. D. Kokkotas, T. A. Apostolatos, and N. Andersson. The inverse problem for pulsating neutron stars: a 'fingerprint analysis' for the supranuclear equation of state. *Mon. Not. R. Astron. Soc.*, 320:307–315, January 2001.

[111] K. D. Kokkotas and B. Schmidt. Quasi-Normal Modes of Stars and Black Holes. *Living Rev. Relativity*, 2(2), 1999. (cited on 25/11/05) `http://www.livingreviews.org/lrr-1999-2`.

[112] K. A. van Riper, R. I. Epstein, and G. S. Miller. Soft X-ray pulses from neutron star glitches. *Astrophys. J. Lett.*, 381:L47–L50, November 1991.

[113] R. Dodson, D. R. Lewis, and P. M. McCulloch. High Time Resolution Observations of a Vela Glitch. In *ASP Conf. Ser. 271: Neutron Stars in Supernova Remnants*, pages 357–+, 2002.

[114] B. J. Owen. Search templates for gravitational waves from inspiraling binaries: Choice of template spacing. *Phys. Rev. D*, 53:6749–6761, June 1996.

[115] LAL Software Documentation, Chapter 18: Package `ring`, `http://www.lsc-group.phys.uwm.edu/daswg/projects/lal/docs/lsd-4.0.pdf`.

[116] K. Hurley. The 4.5+/-0.5 Soft Gamma Repeaters in Review. In *AIP Conf. Proc. 526: Gamma-ray Bursts, 5th Huntsville Symposium*, pages 763–+, 2000.

[117] K. Hurley *et al.* An exceptionally bright flare from SGR 1806-20 and the origins of short-duration γ-ray bursts. *Nature*, 434:1098–1103, April 2005.

[118] K. Ioka. Magnetic deformation of magnetars for the giant flares of the soft gamma-ray repeaters. *Mon. Not. R. Astron. Soc.*, 327:639–662, October 2001.

[119] J. E. Horvath. Energetics of the Superflare from SGR1806-20 and a Possible Associated Gravitational Wave Burst. *Mod. Phys. Lett. A*, 20:2799–2804, 2005.

[120] P. M. Woods *et al.* Spin and Pulsed X-ray Flux Properties of SGR 1806-20 after the Giant Flare. *The Astronomer's Telegram*, 407:1–+, February 2005.

[121] S. Marka and P. Kalmus. private communication, 2005.

[122] B. Allen *et al.* FINDCHIRP: an algorithm for detection of gravitational waves from inspiraling compact binaries. *ArXiv General Relativity and Quantum Cosmology e-prints* `gr-qc/0509116`, September 2005.

[123] R. Umstätter *et al.* Bayesian modeling of source confusion in LISA data. *Phys. Rev. D*, 72(2):022001–+, July 2005.

[124] R. Dodson *et al.* PSR 0833-45. *IAU Circ.*, 8370:4–+, July 2004.

[125] M. J. Stark *et al.* Pulsar frequency glitches in the Accreting pulsar SAX J2103.5+4545. *American Astronomical Society Meeting Abstracts*, 205:–+, December 2004.

[126] D. K. Galloway, E. H. Morgan, and A. M. Levine. A Frequency Glitch in an Accreting Pulsar. *Astrophys. J.*, 613:1164–1172, October 2004.